

SIMULATIONS FOR MODELLING OF
POPULATION BALANCE EQUATIONS OF
PARTICULATE PROCESSES USING
DISCRETE PARTICLE MODEL (DPM)

NARNI NAGESWARA RAO



Fakultät für Mathematik

Otto-von-Guericke Universität Magdeburg

Simulations for Modelling of Population Balance Equations of Particulate Processes using the Discrete Particle Model (DPM)

Dissertation
zur Erlangung des akademischen Grades

doctor rerum naturalium
(Dr. rer. nat.)

genehmigt durch die Fakultät für Mathematik
der Otto-von-Guericke-Universität Magdeburg

von **Narni Nageswara Rao**
geb. am 01. July 1979 in Kappaladoddi, India

Gutachter:

Prof. Dr. rer. nat. habil. Gerald Warnecke
Prof. Dr.-Ing. habil. Stefan Heinrich

Eingereicht am: 04. Februar 2009
Verteidigung am: 24. März 2009

Nomenclature

Latin Symbol

| | | |
|----------------------|--|---------------------------------|
| a, b, c | Constants | — |
| A_i | Area of the particle i | m^2 |
| C_d | Drag coefficient | — |
| d_α | Diameter of the particle α | m |
| $\langle d \rangle$ | Average diameter | m |
| e | Coefficient of restitution | — |
| g | Acceleration due to gravity | m/sec^2 |
| G | Growth rate | $1/sec$ |
| h | Height of the bed | m |
| I | Unit tensor | — |
| I_α | Moment of inertia of particle α | Kgm^2 |
| J | Impulse vector | Kgm/sec |
| k | Boltzmann constant | $1.380 \times 10^{-16} erg/K^0$ |
| $K(t, x, y)$ | Aggregation kernel | m^3/sec |
| $K(x, y)$ | Collision frequency function | m^3/sec |
| $K_0(t)$ | Aggregation efficiency function | $1/sec$ |
| $K_{i,j}(t)$ | Aggregation kernel among classes i and j | m^3/sec^2 |
| L_i | Length of the particle i | m |
| M | Average molecular weight of air | Kg/mol |
| m_α | Mass of particle α | Kg |
| n | Normal unit vector | — |
| $n(t, x)$ | Number density at time t of particle property x | $1/m^3$ |
| $n_0(x)$ | Initial number density of the particle with property x | $1/m^3$ |
| n_i | Particle concentration of class i | $1/m^3$ |
| n_j | Particle concentration of class j | $1/m^3$ |
| $N_{i,j}$ | Number of collisions between class i and class j | m^3/sec |
| N_i | Number of particles of class i | — |
| $N_{i,sim}$ | Number of particles of class i from simulation | — |
| $N_{i,expt}$ | Number of particles of class i from experiment | — |
| N_j | Number of particles of class j | — |
| N_{cell} | Number of Eulerian grid cells | — |
| p | Pressure of the gas | $dyne/m^2(Pa)$ |
| r_α | Radius of the particle α | m |
| R | Gas constant | $8.31 \times 10^7 erg/K^0 mol$ |
| Re_α | Particle Reynolds number | — |
| $\langle Re \rangle$ | Average Reynolds number | — |

| | | |
|---------------------|-----------------------------------|---------|
| s | Surface areas of the particle | m^2 |
| S_t | Stokes number | — |
| S_t^* | Critical Stokes number | — |
| t | Time | sec |
| \mathbf{t} | Tangential unit vector | — |
| t_{sim} | Simulation time | sec |
| T | Temperature | K^0 |
| T_α | Torque | Nm |
| \mathbf{u} | Velocity of the gas | m/sec |
| \mathbf{U} | Relative velocity | m/sec |
| \mathbf{v}_α | Velocity of the particle α | m/sec |
| V_α | Volume of the particle α | m^3 |
| V_{bed} | Volume of the bed | m^3 |
| V_{cell} | Volume of Eulerian grid cell | m^3 |
| V_{fluid} | Volume of the fluid | m^3 |
| $V_{particles}$ | Volume of the particles | m^3 |
| W | Effective volume of the particle | m^3 |
| W^* | Critical volume of the particle | m^3 |
| \mathbf{x}_α | Position of the particle α | m |
| x, y | Volume of the particle | m^3 |
| z | Random number | — |
| z_α | Height of the particle α | m |

Greek Symbol

| | | |
|-------------------|--|-----------------------|
| β | Interphase momentum transfer coefficient | Kg/m^3sec |
| β_0 | Coefficient of tangential restitution | — |
| μ | Gas phase shear viscosity | $Kg/msec$ |
| μ_j | The j th moment | $m^{3j} \cdot m^{-3}$ |
| δ | Distance | m |
| δt_{flow} | Time step for gas phase | sec |
| $\delta(x)$ | Dirac-delta distribution | — |
| $\delta_{i,j}$ | Kronecker delta | — |
| ϵ | Void fraction | — |
| λ | Gas phase bulk viscosity | $Kg/msec$ |
| $\lambda(t)$ | Specific aggregation rate function | $1/sec$ |
| Ω | Discretized domain | — |
| ω | Angular velocity | $1/sec$ |
| ρ | Density of the gas | Kg/m^3 |
| η | Bed parameter | (dimensionless) |
| Γ | Laminar shear velocity of gas | m/sec |
| τ | Gas phase stress tensor | $Kg/msec^2$ |
| σ | Standard deviation | m |

Subscripts

| | |
|-----------|------------------------------|
| 0 | Initial condition |
| α | Particle index |
| a | Particle a |
| ab | Between particle a and b |
| b | Particle b |
| agg | Aggregation |
| bed | Fluidized bed |
| break | Breakage |
| coll | Collision |
| cell | Cell size |
| expt | Experiment |
| i, j, k | Index |
| n | Normal |
| step | Time step |
| sim | Simulation |
| t | Tangential |

Superscripts

| | |
|----------|------------------------|
| – | Mean or average values |
| \wedge | Simulated value |
| n | Value at n th level |

Acronyms

| | |
|------|--------------------------------------|
| CA | Cell Average |
| DPM | Discrete Particle Model |
| DEM | Discrete Element Method |
| EKE | Equi-partition Kinetic Energy kernel |
| IPSD | Initial Particle Size Distribution |
| KTGF | Kinetic Theory of Granular Flow |
| PBE | Population Balance Equation |
| PSD | Particle Size Distribution |
| RE | Relative Error |
| SSE | Sum of Square of Errors |

Contents

| | | |
|----------|---|-----------|
| 1 | General Introduction | 1 |
| 1.1 | Introduction | 1 |
| 1.2 | Fluidized bed spray granulation | 2 |
| 1.3 | Particle formation mechanisms | 3 |
| 1.3.1 | Agglomeration | 4 |
| 1.3.2 | Nucleation | 4 |
| 1.3.3 | Growth | 4 |
| 1.4 | Modelling of the spray granulation processes | 5 |
| 1.4.1 | Multi scale modelling of fluidized beds | 5 |
| 1.4.2 | Micro-Macro modelling of the fluidized bed | 7 |
| 1.5 | Outline of the thesis | 8 |
| 2 | Population Balance Equations | 10 |
| 2.1 | Introduction | 10 |
| 2.2 | Aggregation equation | 11 |
| 2.2.1 | Continuous form of the aggregation equation | 12 |
| 2.3 | Scaling of the equations | 13 |
| 2.3.1 | Dimensional analysis for discrete equation | 13 |
| 2.3.2 | Dimensional analysis of the continuous equation | 14 |
| 2.3.3 | Number density selection and dimensional analysis of the kernel in applications | 14 |
| 2.4 | Properties of agglomeration kernels | 15 |
| 2.4.1 | Theoretical kernels | 16 |
| 2.4.2 | Empirical kernels | 21 |
| 2.4.3 | Experimental kernels | 24 |
| 3 | Discrete Particle Model | 27 |
| 3.1 | Introduction | 27 |
| 3.2 | The discrete particles | 28 |
| 3.3 | The gas-phase | 30 |
| 3.3.1 | Initial and boundary conditions | 31 |
| 3.4 | Two-way coupling | 32 |
| 3.4.1 | Hard sphere collision model | 33 |

| | | |
|----------|---|-----------|
| 3.5 | Numerical calculations | 36 |
| 4 | Modelling of collision frequency functions using DPM | 43 |
| 4.1 | Introduction | 43 |
| 4.2 | Derivation of collision frequency functions | 44 |
| 4.3 | Correction to the aggregation equation | 46 |
| 4.4 | Physical description of the flow pattern inside fluidized beds | 47 |
| 5 | Simulation results | 49 |
| 5.1 | Initial parameters | 49 |
| 5.1.1 | Initial assumptions | 49 |
| 5.1.2 | Initial particle size distributions | 50 |
| 5.2 | Evaluation of the bed parameter | 53 |
| 5.3 | Simulation results for a pseudo 3D bed | 55 |
| 5.3.1 | Log-Normal distribution | 62 |
| 5.4 | Simulation results for 3D beds | 63 |
| 6 | Evaluation of aggregation efficiency rate | 66 |
| 6.1 | Evaluation of the aggregation efficiency rate | 66 |
| 6.2 | Simulation results for the aggregation efficiency rate | 68 |
| 6.2.1 | Aggregation in pseudo 3D fluidized bed | 69 |
| 6.2.2 | Aggregation in 3D fluidized beds | 71 |
| 6.2.3 | Aggregation in pseudo 3D fluidized bed with log-normal distribution | 74 |
| 6.3 | Numerical methods for population balance equations | 74 |
| 6.4 | Computation of the particle size distributions | 77 |
| 6.4.1 | Computation of the particle size distribution for pseudo 3D fluidized bed | 77 |
| 6.4.2 | Computation of the particle size distribution for 3D fluidized bed | 79 |
| 6.4.3 | Computation of the particle size distribution for 3D fluidized bed with log normal distribution | 79 |
| 7 | General conclusions and outlook | 81 |
| A | | 83 |
| A.1 | Analytical derivation of shear kernel for fluidized bed | 83 |
| A.2 | Analytical solution for shear kernel for monodisperse initial conditions | 85 |
| B | | 87 |
| B.1 | Physical and Numerical parameters of the simulations | 87 |
| B.2 | Initial particle size distributions | 88 |
| B.2.1 | Particle size distribution for 5000 particles | 88 |
| B.2.2 | Particle size distribution corresponding to 15000 particles | 90 |

Chapter 1

General Introduction

1.1 Introduction

Mathematical modelling plays a vital role in all disciplines of science and engineering. Its aim is to describe the real world phenomena through mathematics. Due to enormous improvements in computational speed and algorithms, simulating many real world phenomena is within reach. Using these simulation results modelers try to apply them to the realistic problems in different fields such as industry, environment and weather prediction, life sciences, and sports in order to make more efficient mathematical models. Further details of such improved models and applications can be found in (42). The present thesis is concerned with such an application of modelling and simulations for fluidized bed granulation in process engineering.

Gas-fluidized beds are widely applied in the chemical process industry. Typical applications cover a wide variety of physical and chemical processes such as fluidized bed combustion, catalytic cracking of oil and fluidized bed granulation (detergents, fertilizers, food industry) to name a few. They have several advantageous properties like isothermal conditions throughout the bed, excellent heat and mass transfer properties and possibility of continuous operation. Apart from the above advantages they have a special application of minimizing the industrial waste, which results to the reduction of the environmental pollution.

We have different mathematical models to describe the fluidized bed spray granulation. Development of multiscale analysis techniques and algorithms to describe the exchange between mechanical, thermal, and chemical processes in heterogeneous spatial scales of the fluidized beds is still a challenging task to the researchers. A continuous heat and mass transfer model for the fluidized bed granulation was developed by Heinrich (50). Further, the model was extended with the inclusion of a drying mechanism by Peglow (39). An efficient numerical scheme for these fluidized bed granulation models has been studied in Nagaiah (8). These models give on the macro level physical insight into the fluidized bed granulation process and the results are comparable to laboratory experiments.

A main property required for the end product is the particle size. To understand the changes in the particle size distribution, population balance equations are widely applied for the fluidized bed. A detailed modelling and numerical aspects of these population balance equations for the fluidized bed are described in Peglow (39) and Kumar (30).

The final product is not only dependent on these macro properties but also on the micro properties like particle movement, particle collisions, etc. and on the material properties like viscosity, density, etc. There exist no proper experimental techniques to understand these micro particle properties in great detail. To analyse these micro properties, computer simulations based on the discrete element methods (DEM) are widely used in the research.

In the present thesis we study a model which includes the micro and macro properties. To study these micro-macro models, multi phase models are widely used in the research. In this work we used a two phase model which is known as Discrete Particle Model (DPM). In this model compressible Navier-Stokes equations are used to describe the gas flow (macro model) and Newtons equations to describe the particle movement (micro model) for a batch system. A review of the use of the discrete particle models for understading the flow phenomena inside the fluidized beds is found in (11).

1.2 Fluidized bed spray granulation

Particle size enlargement can be done by using different mechanisms. Granulation is one of the important techniques which are widely used in industry. Important granulation instruments, which are widely used in industry are pan, drum, and fluidized beds, etc. Major processes in the granulation are agglomeration, nucleation, growth and breakage, etc. Some typical products from granulation process are given in the Figures 1.1 and we can observe that the particle size is the most important desired property.

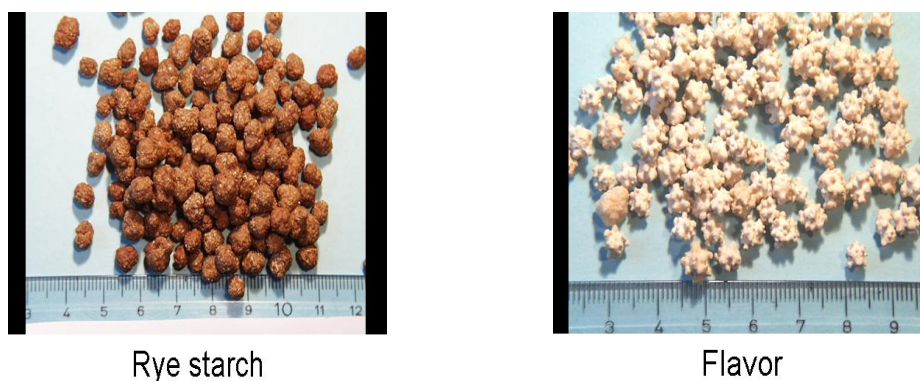


Figure 1.1: Typical products of fluidized bed

A model for an industrial fluidized bed is given in the Figure 1.2. Important ingredients of the

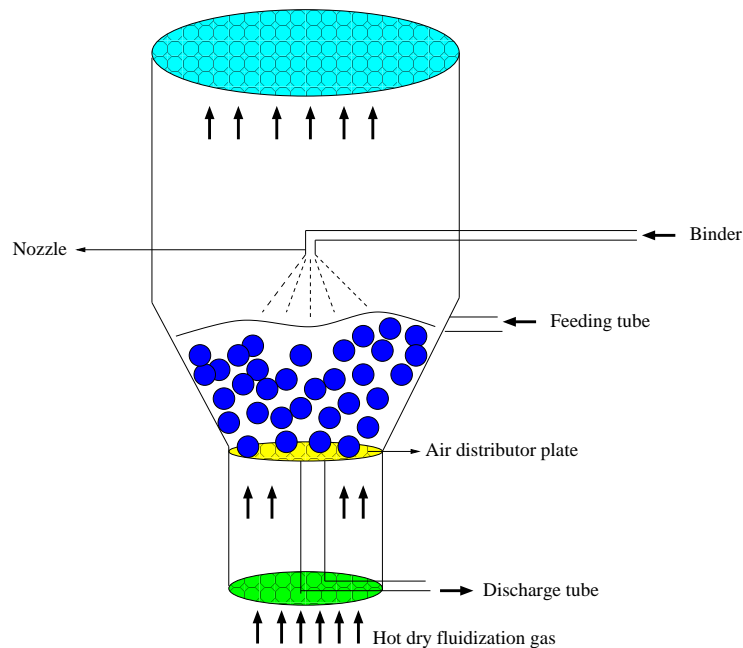


Figure 1.2: Schematic representation of a spray granulation process

granulation process are the liquid binder and solid particles. The particles are mixed by supplying continuous hot dry gas flow from the bottom of the bed. The gas is distributed into the main body of the bed through air distributor. The liquid binder is sprayed from the top of the bed through the nozzle. The spraying in can occur from the top down, from the bottom up, or sideways. The liquid binder evaporates in the hot, unsaturated fluidizing gas and the liquid binder sticks to the particles and grows in layers on the particle surface. This process is called *granulation* or *layered growth process*.

The particles are fed through the feeding tube. The binder droplets are deposited on the particles and distributed through spreading. After getting enough binder, the particles sticks together and forms bigger size particles. Once the desired particle size is achieved, the particles are removed from the bed via a discharge tube inserted at the bottom of the bed. Typical particle formation mechanism are explained in the next section.

1.3 Particle formation mechanisms

Granulation is a complex process involving several physical and chemical phenomena. Combination of all these phenomena ultimately leads to the formation of particles. We will divide these phenomena into three groups of rate processes. In the following subsections we will explain these particle formation mechanisms.

1.3.1 Agglomeration

This process has different linguistic names in the literature based on the applications. For example in the fluidized bed industry *agglomeration*, in atmospheric sciences *coagulation*, etc. But from the mathematical point of view all these processes are treated as same. The process of agglomeration is represented pictorially in the Figure 1.3. In this picture the granule is denoted by blue color and the binder is denoted with color green.

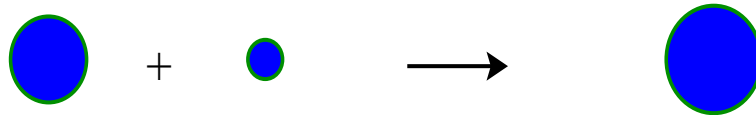


Figure 1.3: Binary aggregation

In this process particles combine to form a larger particle. In the agglomeration process the particle surface is wetted with the binder, and particles with sufficient binder layer stick together and then forms the bigger size particles. If this process is among two particles then we call it binary aggregation otherwise we call it multiparticle aggregation. In fluidized beds binary aggregation is more frequent in comparison with multi particle aggregation.

1.3.2 Nucleation

This is the process in which new particles are formed from vapour molecules due to condensation. In this process we have only birth of particles from the vapour phase. This process is explained in the Figure 1.4 as the blue colored molecular matter condenses and forms a new particle. Nucleation has significant effect on the total number of particles but less effect on the total

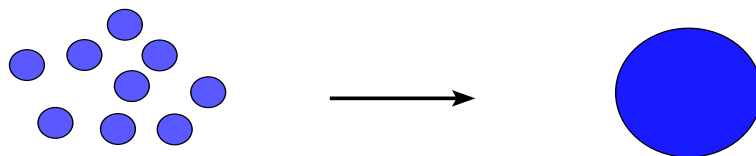


Figure 1.4: Nucleation

volume of particles. The nuclei are usually treated as the smallest possible particles in the system.

1.3.3 Growth

The particle grows as a result of spreading of the liquid binder on the surface of the particles. This process is also known as layering or coating. A graphical representation of growth process is provided in the Figure 1.5.

In a fluidized bed, a liquid is sprayed on to solid particles by an injection nozzle. The liquid drops are deposited onto the solid particles and are distributed through spreading. The intensive

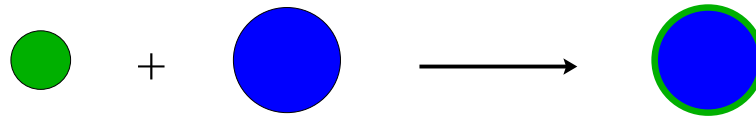


Figure 1.5: Growth

heat and mass transfer, due to the supply of the hot gas, results in a rapid increase of hardness of the fluid film through drying. In this growth process the number of particles does not change but the total volume of particles increases.

1.4 Modelling of the spray granulation processes

Particle size distributions give one of the most important descriptions of the granulation process. Macroscopic models like Population Balance Models are widely used to evolve the particle size distribution in granulation processes. The use of population balance modelling was hampered by the kinetic parameters like kernels have proven more difficult to predict PSD and are very sensitive to operating conditions and material properties. Therefore to model the effect of these parameters a microscopic model involving the particle collision mechanism, material properties, etc. needs to be developed.

1.4.1 Multi scale modelling of fluidized beds

Chemical engineering uses mathematical models to simulate different processes like polymerization, granulation, etc. The development of granulation processes via drum, pan or fluidized bed granulation is a multiscale operation, where the typical macro analysis of continuum mechanisms must be connected to micro operations. A review of systems modelling and applications in granulation are explained in (7). Enormous increase in computer power and algorithm development, fundamental modelling of granulation process in a fluidized bed has come recently within reach. In last decade a significant research efforts have been made to develop detailed micro balance models to study the complex hydrodynamics of gas-fluidized beds. Broadly speaking two different types of hydrodynamic models can be distinguished, Eulerian (continuum) models and Lagrangian (discrete element) models.

Hoomans (20, p.14) states that, "In order to model a large (industrial) scale fluidized bed a continuum model, where the gas phase and the solids phase are regarded as interpenetrating continuous media, is the appropriate choice. This Eulerian-Eulerian type of model have been developed and successfully applied over the last two decades" These models require closure relations for the solids phase stress tensor and the fluid-particle drag relation. Improved empirical closure relations for the solids phase stress tensor and fluid-particle drag coefficient can be obtained by using kinetic theory of granular flow and lattice Boltzmann simulations (3) respectively.

"In discrete particle models the Newtonian equations of motion are solved for each individual

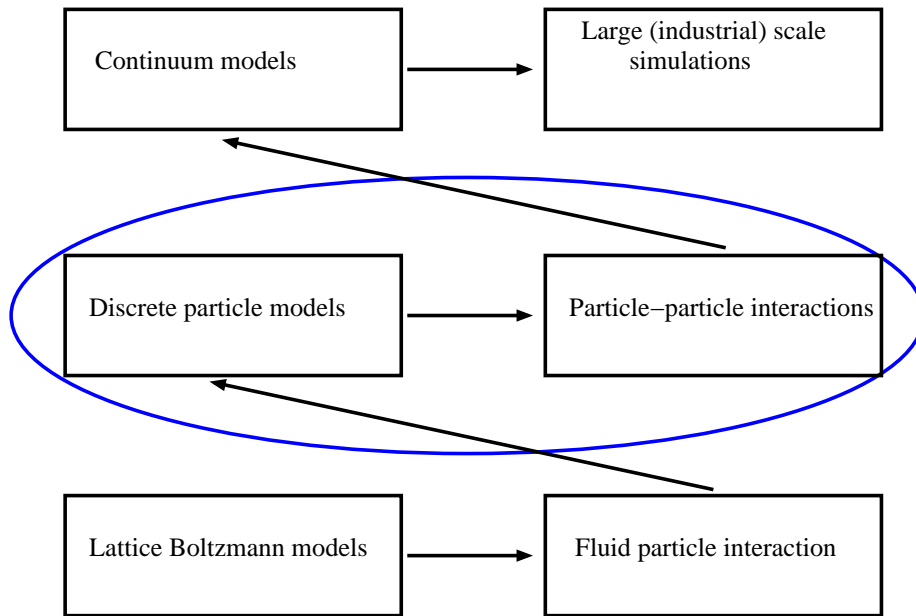


Figure 1.6: Multi scale modelling of the spray granulation process

solid particle in the system. In this Eulerian-Lagrangian type of model a closure relation for the solids phase rheology is no longer required since the motion of the individual particles is solved directly. However, the number of particles that can be taken into account in this technique is limited ($< 10^{-6}$ [sic] $< 10^6$). Therefore, it is not yet possible, even with modern day super computers, to simulate a large (industrial) scale system (20, p.14)." Despite this the discrete particle model is useful in understanding the influence of particle properties on the hydrodynamics of gas-fluidized beds and particle-particle collisions in a microscopic level.

According to Hoomans (20, p.15), "When the gas flow is resolved on a length scale smaller than the particle size these closure relations for fluid-particle drag are no longer required. Instead they can actually be obtained from the simulations. The Lattice Boltzmann technique seems to be best suited for such simulations because it is very flexible in dealing with complex flow geometries It is important to realise that these Lattice Boltzmann simulations are limited to systems consisting of a number of particles that is significantly smaller ($< 10^{-3}$ [sic] $< 10^3$) than the number of particles that can be taken into account using discrete particle models ($< 10^{-6}$ [sic] $< 10^6$).

In short the multi-scale concept as presented in [Figure 1.6] consists of three classes of models where more detail of the two-phase flow is resolved going from continuum models to discrete particle models to Lattice Boltzmann models. This goes at the cost of increased computational requirements which necessitates a size reduction of the simulated system. The model capable of simulating a larger system is fed with a closure relation obtained from a more microscopic simulation. In return the results of these simulations can be used to pass on information to

models capable of simulating the flow on a larger scale."

1.4.2 Micro-Macro modelling of the fluidized bed

In the previous section we have seen three different types of models for simulating the fluidized bed spray granulation. Very few researchers are working in the direction of comparing these models with the existing macro models. In the Graduate school GKMM-828, a considerable amount of work was done in the direction of finding the micro-macro transitions in structured media and particulate systems. The work involves the study of different kinds of micro structures like

- different phases of solids in polycrystalline materials during the processing
- material reinforcement in composite materials for studying the mechanical properties of the materials
- solid particles moving in fluids or gases for environmental applications
- mixtures of interacting particles or liquids and gases in porous solid media for drying technology applications

etc. Different algorithms and simulation softwares are developed to calculate the micro properties of these structures. The results of the Micro-macro comparisons of the models are given in the book (5).

Population balance equations describe the rate of change of the particle number density of a system on a macroscopic level. These equations are widely applied to calculate the number density distribution in fluidized bed spray granulations. Kernels are the most important quantity representing microscopic kinetics of the population balance equations, which dictate the dynamics of the particle number density distribution. Determination of the kernels requires the microscopic simulations of the fluidized bed.

The aggregation equation is an important example of macroscopic population balance equation. This is an integro-partial differential equation and is given as

$$\frac{\partial n(t, x)}{\partial t} = \frac{1}{2} \int_0^x K(t, x - y, y) n(t, x - y) n(t, y) dy - n(t, x) \int_0^\infty K(t, x, y) n(t, y) dy, \quad (1.1)$$

with the initial condition $n(0, x) = n_0(x) \geq 0$. The Kernel $K(t, x - y, y)$ describes the aggregation frequency of particles of size $x - y$ with particles of size y . The aggregation kernel can be decomposed into size dependent and time dependent functions, i.e., $K(t, x, y) = K_0(t)K(x, y)$.

The derivation of kernels involves the following two steps:

- Determination of the collision frequency function $K(x, y)$, or reaction rates in chemical terminology, as given coefficients. For the aggregation process we have a second order reaction.

- Make some physical assumptions on the interaction mechanism of the particles to calculate an explicit expression for the aggregation efficiency function $K_0(t)$.

The calculations of the kernels were evolved from two different approaches. 1. Calculation with realistic experimental results. 2. Computer simulation of the experiments with simple mathematical models. For the last two decades few advances were made in the direction of determination of the kernels using computer simulations.

Recently Tan et al. (51) have made an attempt to build a population balance model for fluidized bed melt granulation from the kinetic theory of granular flow (KTGF). They showed that the distribution of particle velocities obtained from Discrete Particle Modelling (DPM) are same as those obtained from the kinetic theory of granular flow. With this result he assumed that an Equi Kinetic Energy (EKE) kernel will be a suitable choice. He compared the particle size distributions obtained from the experiments and Discretized Population Balance (DPB) modelling with EKE kernel.

A comparison of the experimental results and the simulated results of Discretized Population Balance (DPB) equations with EKE kernel are given in (51) for aggregation process.

1.5 Outline of the thesis

This thesis starts with an introduction to the population balance equations in Chapter 2. In Section 2.2 we explain the assumptions and properties of the discrete and continuous forms of the aggregation equation. Section 2.3 involves the dimensional analysis of these equations and their importance in the modelling of the the aggregation kernels and number density selection for various applications. Different aggregation kernels exist in the literature based on theoretical derivation for the physical process, empirical the observations of the experiments and from the analysis of the experimental data. Properties of the some of these kernels are explained in the Section 2.4.

Chapter 3 is concerned with the Discrete Particle Model (DPM), which is a two phase flow model. We give a short introduction to the model in Section 3.1. Section 3.2, 3.3 explain the governing equations describing solid particle phase and gas phase respectively. The closure laws coupling these phases are described in Section 3.4 and Section 3.4.1 explains the hard sphere collision model for the solid particle interactions. We end this chapter with explanations of the numerical calculations and the modifications made to the existing code for calculating the collision frequency function.

Modeling of the kernels is explained in Chapter 4. The introductory Section 4.1 explains the recently existing literature for modeling of kernels. Section 4.2 explains the derivation of the collision frequency functions. A correction to the aggregation equations and its effect on the aggregation equation is explained in Section 4.3. The last Section 4.4 is concerned with the physical description of the flow pattern inside fluidized beds based on particle Reynolds number.

The particle Reynolds number shows that the shear forces are dominating. This gives an indication for use of the shear kernel.

Simulation results for modeling collision frequency functions are given in Chapter 5. Section 5.1.1 explains the various initial parameters and assumptions for the computer simulations. Section 5.1.2 gives the various particle size distributions. In Section 5.2 we explain the evaluation of the bed parameter. Simulation results for a pseudo 3D bed are given in Section 5.3 and a special case of particle size distribution (normal distribution) results are given in Section 5.3.1. Simulation results for a 3D bed are given in Section 5.4. We end this chapter with the discussion of the results in Section 5.5.

Chapter 6 involves the crucial part of the thesis involving a micro-macro comparison. In Section 6.1 we explain the assumptions on the simulations for the evaluation of the aggregation efficiency. In Section 6.2, we calculated the aggregation efficiency function from the discrete particle model simulations for pseudo 3d and 3d fluidized beds. Section 6.3 explains the numerical methods for solving the population balance equations, in particular the cell average technique. Computation of the particle size distributions with the newly derived, simulation based kernels are given in Section 6.4.

Chapter 7 gives the general conclusions and outlook of the present thesis.

In Appendix A we explain the analytical derivation of the shear kernel based on geometry. Appendix B explains the major simulation parameters of the Discrete Particle Model (DPM). Appendix C gives the initial particle size distributions for different number of particles.

Chapter 2

Population Balance Equations

In this chapter we describe population balance equations for particulate systems. We describe various forms of the aggregation equation and its mathematical properties. This chapter gives a deep insight into the modelling aspects of the aggregation kernel. We end up this chapter with the some important properties of theoretical, phenomenological and experimental kernels which are widely used in the applications.

2.1 Introduction

Population balance equations are used to determine the particle number density distribution on a macroscopic level. A general one particle property, e.g. particle volume, equation for a well mixed system is given by the following

$$\frac{\partial n(t, x)}{\partial t} + \frac{\partial [G(t, x)n(t, x)]}{\partial x} = F(t, x) \quad (2.1)$$

where

$$F = B_{nucleation}(t, x) + B_{agg}(t, x) + B_{break}(t, x) - D_{agg}(t, x) - D_{break}(t, x). \quad (2.2)$$

The above equation describes the change of particle size distribution $n(t, x)$ with respect to time $t \geq 0$ corresponding to the particle property, volume $x \geq 0$. The second term on left hand side of the Equation (2.1) represents the particle growth due to the addition of liquid binder to the particles and $G(t, x) = \frac{dx}{dt}$. The first three terms on the right hand side of (2.2) represent the birth of particles due to nucleation, aggregation and breakage. The last two terms on the right hand side of (2.2) represent the death of particles due to aggregation and breakage. The initial and boundary conditions required for (2.1) are generally stated as

$$n(0, x) = n_0(x)$$

and

$$n(t, 0) = 0,$$

respectively. The latter condition indicates that there are no particles of zero size, which is physically well justified.

2.2 Aggregation equation

Disperse systems describe the solid particles or liquid droplets suspended in a medium, usually in a gas. Applications have covered a wide range of disperse systems, especially solid-gas, solid-liquid, solid-liquid-gas, liquid-liquid,...etc.

The disperse systems are dynamic in time due to the movement of the particles in the medium. The particles are set in motion by external fields like gas flow, stirrer, ...etc. As a result of this movement, the particles collide. The collision and aggregation in this system leads to the change in the particle size, here we describe the particle volume in terms of a distribution function.

Population balance equations are very frequently used to study the particle size distribution in the disperse systems. To understand this particle distribution, Smoluchowski (49) derived an infinite set of nonlinear ordinary differential equations for his theory of rapid coagulation processes with the following assumptions:

- The number of particles per unit volume of the fluid is sufficiently small, i.e. we describe a dilute system.
- Binary collisions are assumed to occur simultaneously.
- Incompressible spherical particles are assumed to collide.
- There is no fluid interaction with the particles.

Based on the above assumptions he derived the following system of ordinary differential equations

$$\frac{dn_i(t)}{dt} = \frac{1}{2} \sum_{j=1}^{i-1} K_{i-j,j} n_{i-j}(t) n_j(t) - n_i \sum_{j=1}^{\infty} K_{i,j} n_j(t) \quad (2.3)$$

for $i = 1, 2, 3, \dots$, with the initial conditions $n_i(0) = n_i^{(0)} \geq 0$.

The above equation is known as the discrete coagulation equation. The complexity of the above system is dependent on the form of the kernel $K_{i,j}$. The function $K_{i,j}$ is known as the coagulation kernel. It describes the intensity of the particle interactions between particle classes i and j . The coagulation kernel is non-negative and symmetric, i.e. $K_{i,j} \geq 0$ and $K_{i,j} = K_{j,i}$. Different kernels exist in the literature based on different applications. Detailed discussion of various kernels can be seen in the next section. The unknown non-negative function $n_i(t)$ is the concentration of particles with size $i, i \geq 1$.

The term $\frac{1}{2} \sum_{j=1}^{i-1} K_{i-j,j} n_{i-j}(t) n_j(t)$ is known as the birth term and $n_i \sum_{j=1}^{\infty} K_{i,j} n_j(t)$ is known as the death term.

2.2.1 Continuous form of the aggregation equation

Müller (36) derived the continuous form for the above equation as an integro partial differential equation that is given as

$$\frac{\partial n(t, x)}{\partial t} = \frac{1}{2} \int_0^x K(t, x - y, y) n(t, x - y) n(t, y) dy - n(t, x) \int_0^\infty K(t, x, y) n(t, y) dy, \quad (2.4)$$

with the initial condition $n(0, x) = n_0(x) \geq 0$.

The Kernel $K(t, x - y, y)$ describes the coagulation of particles of size $x - y$ with particles of size y . The first term on the right hand side of (2.4) describes birth of the particles. The second term on the right hand side of the equation (2.4) describes the death of the particles.

Mathematical classification

Mathematically the integral operators of (2.4) are classified as follows

- The birth term of the coagulation equation (2.4) is a nonlinear Volterra integral operator,
- The death term of the coagulation equation (2.4) is a quasilinear Fredholm integral operator.

Remark 2.1 *One should note that in the discrete as well as in the continuous case the time t is always a continuous coordinate. The difference is in the property coordinate x (volume or mass) only.*

Moments of the aggregation equation

The moments of the aggregation equation play a vital role in characterizing the properties of the particle distribution. The j^{th} moment of the particle size distribution $n(t, x)$ of the aggregation equation (2.4) is defined as

$$\mu_j = \int_0^\infty x^j n(t, x) dx. \quad (2.5)$$

The moments represent some important properties of the distribution. The zeroth ($j = 0$) and first ($j = 1$) moments are proportional to the total number and the total mass of particles respectively. In addition to the first two moments, the second moment of the distribution will be used to compare numerical results, see (30). The second moment is proportional to the light scattered by particles in the Rayleigh limit (18) and is used in atmospheric sciences for study of the rain drop coagulation process.

2.3 Scaling of the equations

For analysis of a particle system one needs to evaluate the change in the population of particles in the dispersed phase. It involves both, a local and a global environment. The local environment involves the particle properties like diameter, volume, mass, ...etc. These are the state variables. The global environment consists of the space variables.

Usually for particulate systems one considers the influence of the local properties, and the effect of the global environment is neglected with the assumption of a homogenized medium. But when we do modelling one needs to consider the global environment, in order to understand whether the system is a homogenized or not. To understand the particle interactions, we need to consider the physical description of the system. For this purpose we need to do dimensional analysis.

Dimensional analysis is applied in order to remove the influence of the arbitrary choice of physical units for the systems. In the dimensionless form we can determine the influence of large and small terms in the system in order to simplify it.

To discuss the concepts of dimensional analysis, we need the following definitions:

- We define the mass M of a representative particle by using the unit $\text{kg} = \text{kilogram}$.
- We define the volume for two physical quantities:
 1. Volume of fluid as V_{fluid} and has the dimension length L^3 for notational purpose we write it as L_{fluid} , which is an external parameter corresponding to the space coordinate with unit $L = m$.
 2. Volume of particles as $V_{particles}$ and has the dimension length L^3 for notational purpose we write it as $L_{particles}$, which is an internal parameter corresponding to the particle property with unit $L = m$.
- We define time as T with unit $T = s$.

Remark 2.2 *Here we wish to give a note on particle number density $n(t, x)$. The population is described with the use of suitable external or internal or both the variables, usually number of particles, sometimes with other variables such as mass (extensively used in crystalization process), length (suitable to describe growth process) or volume of particles.*

2.3.1 Dimensional analysis for discrete equation

- Particle concentration $n_i(t)$ is defined as the number of particles per unit volume of the fluid and has the dimension L_{fluid}^{-3}
- The coagulation kernel $K_{i,j}$ is defined as the number of particle interactions in unit volume of fluid per unit time and has the dimension $L_{fluid}^3 T^{-1}$

2.3.2 Dimensional analysis of the continuous equation

Case 1:

- The particle concentration $n(t, x)$ is defined as the number of particles per unit volume of fluid per unit particle volume and has the dimension $L_{fluid}^{-3} L_{particle}^{-3}$
- Dimension of the kernel $K(t, x, y)$ is $L_{fluid}^3 T^{-1}$

Case 2:

- Suppose that for the continuous equation we have dimension of $n(t, x)$ as number of particles per unit volume of particles. That is we are considering the number density as a function of time and material volume with the dimension $L_{particle}^{-3}$.
- Dimension of the kernel $K(t, x, y)$ is T^{-1} . This is usually called a collision frequency kernel in the literature.

2.3.3 Number density selection and dimensional analysis of the kernel in applications

When we are trying to use this aggregation equation for a particulate process, the above dimensional analysis can be used as follows:

In the study of aerosol sciences the particle volume is not effective compared to the volume of the air. So in such models the discrete kernel is widely used by considering the number density as a function of fluid and time. In this case the discrete kernel $K(t, x, y)$ has the dimension $L_{air}^3 T^{-1}$.

In a fluidized bed the volume of the bed is not constant. Therefore the porosity of the bed changes with the time. So in such situations it is necessary to consider both, the volume of fluid and volume of the particles in the calculation of particle concentration. Since the porosity is not constant in our DPM, we consider the case 1 and the kernel has the dimension $L_{fluid}^3 T^{-1}$.

As we stated earlier, the number density can be a function of any material coordinate. In certain applications the mass of the particles is important compared to volume of the particles.

In crystallization processes, particles are formed as a result of change in the thermodynamics of the material. So in such processes the number density solely depends on the amount of material present in the vessel. Therefore we can replace the number density as a function of material and time, and having the dimension $M^{-1} L^{-3}$. In this case the aggregation kernel has the dimension of $ML^3 T^{-1}$. Here L^3 represents the volume of the vessel.

In case of evaluating the numerical solution of the population balance equations with growth, breakage, aggregation and nucleation terms, the number density plays a vital role. One needs

to pay considerable attention to describing the equation satisfying the number and mass conservation properties. A detailed discussion of numerical problems for various number density representations arising in crystallization modeling can be found in Costa et al. (9).

2.4 Properties of agglomeration kernels

Population balance equations are applied to determine the particle number density distribution in a macroscopic level. A binary agglomeration equation for a well mixed system is given as

$$\frac{\partial n(t, x)}{\partial t} = \frac{1}{2} \int_0^x K(t, x - y, y) n(t, x - y) n(t, y) dy - n(t, x) \int_0^\infty K(t, x, y) n(t, y) dy, \quad (2.6)$$

and $n(0, x) = n_0(x) \geq 0$, where $K(t, x, y)$ is the agglomeration kernel. The equation (2.6) describes the number density distribution as a function of one particle property and time. In order to understand the agglomeration process, one needs to explore the physical significance and mathematical nature of the agglomeration kernel. Up to now there is no proper kernel to describe the particle size distribution for fluidized bed granulation. In the current section we are exploring the properties of different existing kernels and their usage.

The agglomeration kernel $K(t, x, y)$ represents the rate at which particles of volume $x - y$ and y aggregating to form particle of volume x . The complexity of solving the equation depends on the form of the kernel $K(t, x, y)$ and it satisfies the following properties

- The kernel is symmetric i.e., $K(t, x, y) = K(t, y, x)$
- non-negative $K(t, x, y) \geq 0$ for all $x, y > 0$
- The kernel is a continuous function on $(0, \infty) \times (0, \infty)$
- Most kernels are homogeneous functions of non-negative degree
- By scaling time, we can eliminate a multiplicative constant from the kernel, e.g. $K(x, y) = xy$ instead of $K(x, y) = cxy$ for constant c

Sastry (46) proposed that the aggregation kernel is a product of two factors, and it is now common practice to view the aggregation kernel as the product of agglomeration efficiency $K_0(t)$ and collision frequency $K(x, y)$, i.e.

$$K(t, x, y) = K_0(t)K(x, y). \quad (2.7)$$

The discrete variant of the agglomeration kernel $K_{i,j}$ among the classes i and j is defined as the product of the collision frequency $K_{i,j}$ of the particles and the agglomeration efficiency $K_0(t)$ i.e.,

$$K_{i,j}(t) = K_0(t)K_{i,j}.$$

The first term, $K_0(t)$, is the efficiency rate constant, which is dependent on various process parameters like kinetic energies of particles, their trajectories and collision orientation, particle characteristics (e.g. mechanical properties and surface structure), viscous dissipation between approaching particles and inter-particle forces, and binder properties, coalescence mechanism, ...etc. Generally $K_0(t)$ is assumed to remain constant throughout the experiment and is size-independent.

The collision frequency $K(x, y)$ or $K_{i,j}$ is a function of particles size, gas velocity, system temperature, ...etc. Most of the models assume that the collision frequency is a function of particle size. Determination of collision frequency function is a complex task in most of the models and it is very difficult to determine from the experiments. In the present thesis we try to fix a size dependent collision frequency function through the simulations.

As we have seen in the previous paragraphs that the agglomeration kernel can be resolved as product of time dependent and internal variable (length, volume, mass, ... etc) dependent components. The time dependent component is a function of the agglomeration process, whereas the internal variable dependent component is a function of transportation process. In the fluidized bed the transportation of particles is due to gas flow. Therefore this function is determined by flow of the gas inside the bed. Based on this flow mechanism of gas we have different kernels. In the next subsections we are giving a detailed account of various kernels used for fluidized bed granulation.

We have different collision frequency functions for different kernels in the literature based on theoretical, empirical and experimental calculations and observations. The Table 2.1 below gives an account of different collision frequency functions.

2.4.1 Theoretical kernels

We have very few kernels in the literature that are derived theoretically, and these kernels are determined based on the mechanism producing relative motion of the particles. In the following sections we give a brief discussion on the derivation of the theoretical kernels and their physical significance.

Brownian kernel

Collisions among the particles of size larger than the mean free path of the gas are diffusion limited. Smoluchowski derived an expression for the collisions of the spherical particles with volume $x^{\frac{1}{3}}$ and $y^{\frac{1}{3}}$ suspended in an infinite medium (gas) in 1917 (49). During this derivation he assumed that the particle motion is random, diffusive. The collision frequency function is given as

$$K(x, y) = 4\pi(D_x + D_y)(x^{\frac{1}{3}} + y^{\frac{1}{3}}) \quad (2.8)$$

| Name of the kernel | Kernel $K(x, y)$ | Comment | Physical application |
|--------------------|---|---------------------------------|----------------------|
| Size-independent | c (26) | All events equally probable | Droplet coalescence |
| Brownian motion | $K_0(x+y)(x^{-1} + y^{-1})(49)$ | Random movement of particles | Aerosols |
| Product | $K_0(xy)$ | large-large, small-small | Polymers |
| Gravitation | $K_0(x+y)^2 x-y (4)$ | Gravitational force is dominant | Aerosols |
| Shear stress | $K_0(x+y)^3(49)$ | Large-large events favored | Fluidized bed |
| Particle inertia | $K_0(x+y)^2 x^2 - y^2 (26)$ | Inertial forces are dominant | Aerosols |
| EKK | $K_0(x+y)^2\sqrt{\frac{1}{x^3} + \frac{1}{y^3}}(22)$ | Large-small events favored | Granulation |
| Kapur | $K_0\left(\frac{(x+y)^a}{(xy)^b}\right)(27)$ | Phenomenological | Granulation |
| Sastry | $K_0(x^{2/3}y^{2/3})(1/x + 1/y)(46)$ | Phenomenological | Granulation |
| Polymerisation | $K_0(x^{1/3} + c)(y^{1/3} + c)$ | Polymers | Branched polymers |
| Adetayo and Ennis | $k(\text{constant}), \text{ if } W < W^*$ $0, \text{ if } W > W^*$ (1) | cutoff kernel | Fluidized bed |

Table 2.1: A summary of proposed kernels in the literature

^awhere a, b, c, K_0 are constants

^bwhere W^* is the critical volume of the particle

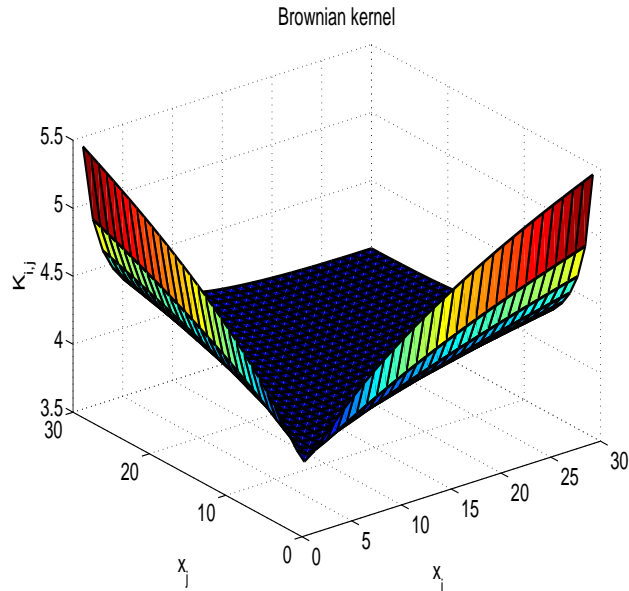
where D_x, D_y are the diffusion constants for the particle classes of volumes $x^{\frac{1}{3}}$ and $y^{\frac{1}{3}}$. If the Stokes-Einstein relation holds for the diffusion coefficient, then this expression becomes

$$K(x, y) = \frac{2kT}{3\mu}(x^{\frac{1}{3}} + y^{\frac{1}{3}})(x^{-\frac{1}{3}} + y^{-\frac{1}{3}}) \quad (2.9)$$

where k is the Boltzmann constant, T the absolute temperature, μ the viscosity of the medium. The Stokes-Einstein relation for the classes i and j is given as

$$D_{ij}R_{ij} = D_1r_1 \left(\frac{1}{r_i} + \frac{1}{r_j} \right) (r_i + r_j)$$

The collision surface among 10 classes of particles for the Brownian kernel is plotted in the figure below. In this figure we can observe the large number of collisions among the large-small size classes and the lower number of collisions among large-large classes.



Remark 2.3 *The Brownian kernel corresponds to disperse systems in an open domain, e.g., a typical aerosol: colloidal sol, liquid droplets, or air bubbles suspended in an agitated liquid. In a fluidized bed the particle motion is induced by the gas flow rather than random, diffusive motion. Therefore the Brownian kernel will not be a suitable choice.*

Remark 2.4 *For monodisperse systems i.e., by setting $x = y$, the collision frequency is given by*

$$K(x, x) = \frac{8kT}{3\mu} = c, \quad (2.10)$$

where c is a constant independent of particle size.

Shear kernel

Smoluchowski (49) derived the shear kernel while modelling the discrete aggregation equation. He derived the shear kernel in terms of geometrical property, volume with the following assumptions

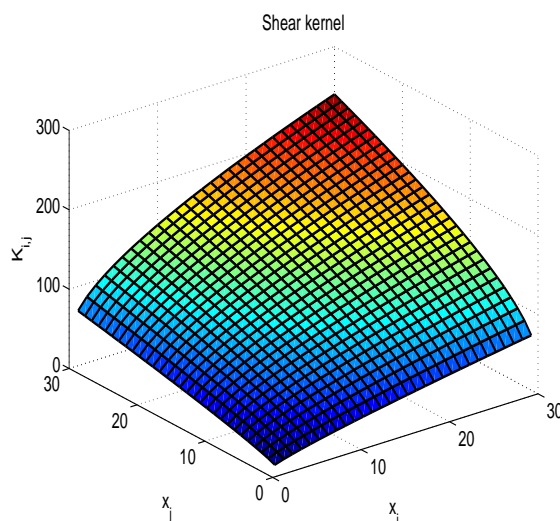
- Particles are spherical in shape
- Particles move in rectilinear paths
- There is no fluid interaction with the particles
- Particles move due to their shear motion
- Brownian motion does not exist in the system

The collision frequency function for shear motion is given as (49)

$$K(x, y) = \frac{4}{3} \Gamma (x^{\frac{1}{3}} + y^{\frac{1}{3}})^3, \quad (2.11)$$

where Γ is the laminar shear velocity of the gas. The derivation of this kernel is explained in Appendix A.

The collision surface among 10 classes of particles for the shear kernel is plotted in the figure below. In this figure we can observe that large number of collisions among the large-large size classes and less number of collisions among small-small classes.



Remark 2.5 *This kernel is widely used in fluidized beds and granulators to model the population balance equations. In the fluidized beds the particles move due to the gas flow. In the granulators, the particle mixing is due to impeller. These two mechanisms cause the laminar shear flow as opposed to the random fluctuations.*

Remark 2.6 *This shear kernel is derived based on geometric approximations of particle paths. So this kernel is not exact, but it is an upper bound.*

Equipartition of kinetic energy kernel

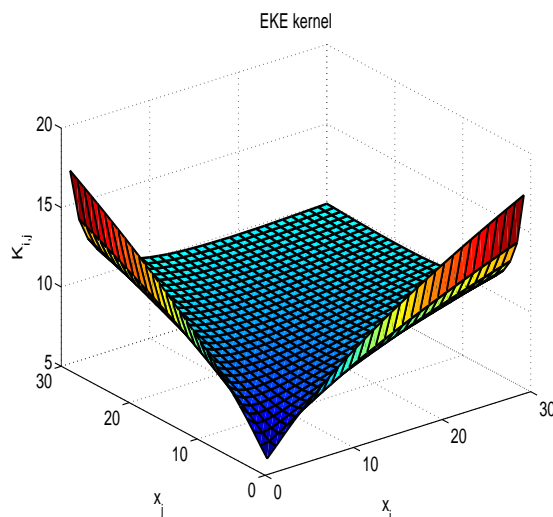
This kernel is based on the assumption that the kinetic theory of granular flow (KTGF) provides an acceptable description of granular flow in a high shear mixer. Hounslow (22) derived an agglomeration kernel based on the following assumptions:

- The kinetic theory of granular flow is an extension of the classical kinetic theory of dense gases.
- The particles are assumed to be spherical, smooth and elastic.
- In a high shear mixer the granules adopt significant rotational velocities they also display noticeable deviations from the local average velocity.
- Each individual particle velocity \bar{v} is decomposed into a local mean velocity \bar{u} and a random fluctuating velocity \bar{V} described by $\bar{v} = \bar{u} + \bar{V}$.

By using the above assumptions, he derived a kernel which is known as Equi-partition of Kinetic Energy (EKE) kernel given as

$$K(t, x, y) = K_0(t)(x^{\frac{1}{3}} + y^{\frac{1}{3}})^2 \sqrt{\frac{1}{x^2} + \frac{1}{y^2}}, \quad (2.12)$$

where $x, y > 0$, and $K_0(t)$ is given separately in concrete situations. The collision surface of the



EKE kernel is plotted in the above figure. We can observe that the collision surface is almost resembling to the Brownian kernel with almost twice the number of collisions due to the local mean velocity supplied by the high shear mixer.

Remark 2.7 *Kinetic theory assumes that all collisions are binary and instantaneous. In dense flows which are commonly found in high shear mixers, this assumption may not be valid.*

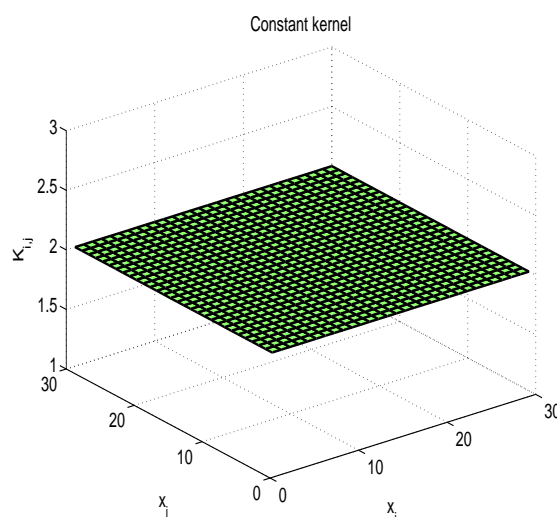
Remark 2.8 *This kernel is widely used in crystallization processes. Here the crystals are formed as a result of stirrer movement and thermodynamic forces which cause the random deviations to the local velocity caused by the stirrer rotations.*

2.4.2 Empirical kernels

Based on intuitive arguments, some of the requirements to be satisfied by the aggregation kernels can be specified. Most of the empirical kernels are determined based on these arguments. But most of the time the validity of the kernels are questioned due to lack of their physical relevance to the experimental results. Several empirical functional forms of the kernels were fitted to the experimental data i.e., empirical kernels are not unique. In spite of all these difficulties, they were widely used in the literature, because explicit solutions are available, and the mathematical properties of the aggregation equation are easily explored.

Size independent or constant kernel

This most simple kernel available in the literature was proposed by Kapur and Fuerstenau (26). In this kernel it is assumed that the particle interactions are random with no higher probability for agglomeration between any two preferred sizes. That means the kernel is constant throughout the experiment, which is very far from the real fluidized bed granulation. But the simplicity of the kernel gives the advantage of having an exact solution to the aggregation equation and is used as a test case in evaluating the efficiency and accuracy of the numerical schemes applied to the population balance equations.



The collision frequency surface among the classes i and j can be seen in the above figure for the constant kernel $K(t, x, y) = 2$.

Remark 2.9 *The continuous models with this kernel have the following limitations:*

- *It provides no information on the higher moments of the size distribution.*
- *The models tends to break down for powders of comparatively large specific surface area.*

Kapur kernel

Kapur and Fuerstenau(28) proposed a population balance equation for nonrandom aggregation of discrete size granules. This equation differs from Smoluchowski's well known aggregation equation, where the aggregation rate is proportional to the product of number concentrations of the two reacting species.

On the other hand, for a given size distribution the concentration of particles in a loosely packed granulating bed is more or less fixed by the packing constraints. Indeed, to a first approximation the packing characteristics (bed porosity and coordination number) are not expected to change appreciably in course of granulation. In this situation, an agglomerate is most likely to encounter only its nearest neighbours which form a cage around it. Consequently, the aggregation in granulation was stipulated in terms of the product of the number of species of one kind with the number fraction of the second kind. This kind of aggregation process is also known as pseudo-first-order rate process.

They proposed the following population balance equation for a batch, restricted-in-space, granulation system as

$$\frac{dn_i(t)}{dt} = -\frac{\lambda(t)n_i(t)}{N(t)} \sum_{j=1}^{\infty} n_j(t) + \frac{\lambda(t)}{2N(t)} \sum_{j=1}^{i-1} n_i(t)n_{i-j}(t) \quad (2.13)$$

where $n_i(t) = \frac{N_i(t)}{V_{bed}}$ is the number of granules of size x_i by volume V_{bed} at time t , $N(t) = \sum_{i=1}^I N_i$ is the total number of granules in the batch, and $\lambda(t)$ is the specific aggregation rate function. Here one should remember that $\lambda(t)$ is not the same as $K(t, x, y)$.

Kapur (27) proposed a phenomenological kernel based on an empirical rate function which, in continuous sample space, is given by

$$\lambda(t) = \beta_0 \frac{(x+y)^a}{(xy)^b} \quad (2.14)$$

where β_0 is a function of water content, particle size distribution and surface area of the powder, nature of the balling device, etc. It does not depend on the granulate size. The other term reflects the non-random nature of the mechanism governing the process. The adjustable parameters a and b as well as β_0 should provide sufficient flexibility for a realistic equivalent mathematical representation of the kinetics.

Remark 2.10 • *Although the kernel (2.14) gives satisfactory results when compared with experimental data, it is only an empirical one.*

- *This kernel did not give any physical insight into the granulation mechanism except for the non-random nature.*

Remark 2.11 *Some of the moments of the similarity function may turn out to be physically meaningless as reported by Wang, and Kapur (27). This is due to the presence of the singularities at $x = 0$ and $x = \infty$.*

Sastry kernel

Sastry (46) proposed an empirical kernel for nonrandom aggregation based on experimental observations and intuitive arguments. He considered that the driving force or potential for aggregation is determined by the surfaces, and that resistance for further deformation is offered by the volumes of the participating species. Thus, the larger the surface area of an agglomerate is, the more potential it has to grow, while at the same time it offers more resistance. Based on these ideas, the following functional form that satisfies most of the above described criteria is chosen:

$$K(t, s, s', x, y) = K_0(t)(s + s') \left(\frac{1}{x} + \frac{1}{y} \right) \quad (2.15)$$

where s, s' and x, y are the surface area and volume of the particles respectively. Given ρ , the apparent agglomerate density, the above equation becomes

$$K(t, m, m') = K_0(t)(36\pi\rho)^{\frac{1}{3}}(m^{2/3} + m'^{2/3}) \left(\frac{1}{m} + \frac{1}{m'} \right). \quad (2.16)$$

Therefore

$$K(m, m') = (m^{2/3} + m'^{2/3}) \left(\frac{1}{m} + \frac{1}{m'} \right). \quad (2.17)$$

The above kernel can be written in terms of volume as

$$K(x, y) = \left(x^{\frac{2}{3}} + y^{\frac{2}{3}} \right) \left(\frac{1}{x} + \frac{1}{y} \right) \quad (2.18)$$

Remark 2.12 *The empirical kernel $K(x, y)$ is a homogeneous function and has **degree or order** $(-1/3)$. The order of the kernel has a major effect on the shape and evolution of particle size distribution. In general, the higher the kernel order, the broader the particle size distribution that results.*

2.4.3 Experimental kernels

Two approaches are widely used to extract the parameters of the agglomeration kernels from the experimental data. Those two are the integral and differential approaches. In this section we are describing these two approaches for evaluating the parameters of the aggregation kernels.

In Chapter 2.4 we have neglected the time dependency of the kernels, but in a more general approach one can supply an additional time dependent factor $K_0(t)$ and write it as

$$K(t, x, y) = K_0(t)K(x, y).$$

Therefore modeling of the agglomeration kernel involves these two functions. Frequently an integral approach is used to determine aggregation rates, in which a kinetic model, containing a number of adjustable parameters, is fitted to an integral form of the rate equations. For a given values of the parameters the experimental data may be simulated by integrating a combination of the rate and kinetic equations. The parameters are usually selected to optimize the fit of the simulated results to those obtained experimentally.

There exists an empirical size-dependent kernel proposed by Kapur (27) for non-random aggregation process of the form

$$K(x, y) = \frac{(x + y)^a}{(xy)^b},$$

where a and b are the empirical parameters to be evaluated. Peglow (39) used this empirical kernel for modelling the fluidized bed spray agglomeration. He evaluated the values of the parameters a and b by using a least squares fit to the experimental data. The values of a and b are 0.7105 and 0.062. He calculated the time dependent parameter $K_0(t)$ for each experiment and observed that the agglomeration rate $K_0(t)$ is independent of process parameters. For details of the process parameters and experimental results, we refer to Peglow (39).

Hounslow (23) developed a technique to determine nucleation, growth and aggregation rates from steady-state experimental data. Having first determined the moments of the experimental size distribution, he determined the growth, aggregation and nucleation rates from these moments. For details of the technique we refer (23).

MMMfT-1.2.cgi.html

Bramley et al. (6) developed a differential technique to determine the growth and aggregation rates from experimental data. For size-independent aggregation in a batch system, he calculated the rate of change of zeroth and third moments, using length as the internal coordinate. They are given as

$$\frac{d\mu_0}{dt} = -\frac{1}{2}K_0\mu_0^2 \quad (2.19)$$

$$\frac{d\mu_3}{dt} = 3G\mu_2 \quad (2.20)$$

where μ_0 , μ_2 and μ_3 are the zeroth, second and third moments. So if the rates of change of the zeroth and third moments are known, values of the aggregation rate K_0 and growth rate G can be calculated directly from the experimental data using the equations (2.19), (2.20).

The differential method outlined above is valid only for size-independent growth and aggregation. For evaluating the rate constants of size dependent kernels, Bramley et al (6) modified the above differential technique by including a source function. Details of the modified differential technique can be see in (6). The differential technique is simple, but its main short coming is that we cannot estimate the errors of fitting.

He compared the simulated and experimental particle size distributions and their moments by using sum of square of errors. The Sum of Squares of Errors (SSE) is defined as

$$SSE = \sum_i (N_{i,sim} - N_{i,expt})^2 \quad (2.21)$$

where $N_{i,sim}$, $N_{i,expt}$ are number of particles in the i^{th} size interval from simulation and experiment. By using SSE it was shown that it is possible to distinguish between the kernels and determine which is appropriate for modeling the aggregation of calcium oxalate monohydrate. It was found that the size independent kernel is most appropriate.

Recently Adetayo et al. (1) proposed a two-stage sequential size independent kernel for the drum granulation of the fertilizers. The shifting criteria is based on the critical effective size of the granule. The kernel is given as

$$K(t, x, y) = \begin{cases} k, & \text{if } W \leq W^* \\ 0, & \text{if } W > W^* \end{cases} \quad (2.22)$$

where W is known as the effective volume and W^* is the critical limit of particle volume having enough binder for possible agglomeration. This critical volume W^* is also referred to as *cutoff size* and it varies with both binder and material properties, and can be determined by micro level studies of the agglomeration process.

The effective volume W is defined as

$$W = \frac{(xy)^b}{(x+y)^a},$$

where a and b are empirical constants. These constants are measurable due to their close physical relationship to the process of particle collision, deformation, and agglomeration process. Detailed characteristics of the cutoff kernel (2.22) with respect to the empirical constants a , b and cutoff size W^* are explained in (1). Adetayo (1) used the coalescence mechanism based on a physical theory developed by Norio et al. (37) to calculate the time dependent part of the coagulation kernel $K_0(t)$.

Population balance equations are widely applied in nano particle preparation and their characterization. Hintz et al. (19) applied population balance equations involving aggregation and breakage in the preparation of titanium dioxide nanoparticles. They evaluated an equilibrium constant as well as an agglomeration and a breakage constant were calculated for a real polydisperse system on the basis of particle and aggregate size distributions.

Chapter 3

Discrete Particle Model

Fluidized beds are widely used in many industries, for example fertilizer industries, food industries, etc. Population balance equations are widely applied to understand the quality of the final product. The most important parameter in these population balance equations is the kernel. Modelling of the kernel involves the understanding of the particle flow inside the fluidized bed.

Fluidized beds involve multiphase flows. Understanding the multiphase flow inside bed is very difficult by using experimental techniques. Sometimes these experimental techniques may disturb the flow field. In recent times computer simulations are widely used to understand the flow inside the bed.

In the present chapter we explain the model which is used to understand the flow mechanism inside the fluidized bed. This is a two phase flow model consisting of solid particles in gas flow. This model is known as the Discrete Particle Model (DPM) and was developed by Anderson et al. (2). We treat the gas phase as a continuous phase, where as each solid particle is treated as a single entity. The gas-solid phases are coupled through empirical relations and the solid particle interactions are calculated through hard sphere collision model.

3.1 Introduction

In this model we considered a rectangular fluidized bed within a Lagrangian frame work. Initially the particles with positions $\mathbf{x}_\alpha \in \mathbb{R}_+^3$ are placed inside the bed domain Ω and the gas is supplied from the bottom of the bed with a minimum fluidization velocity \mathbf{u} under isothermal conditions. The collisions of the particles with the bed walls are considered as elastic reflections. The schematic representation of the bed can be seen in Figure 3.1.

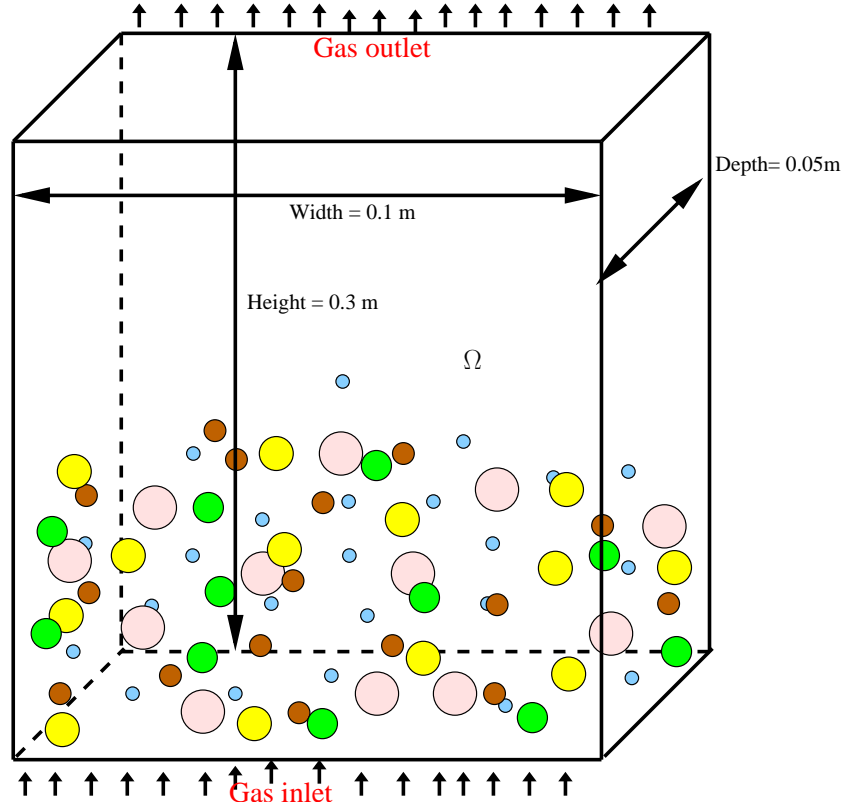


Figure 3.1: Schematic representation of the fluidized bed

3.2 The discrete particles

The motion of each individual particle α with mass m_α and volume V_α is calculated from Newton's second law

$$m_\alpha \frac{d\mathbf{v}_\alpha}{dt} = m_\alpha \frac{d^2\mathbf{x}_\alpha}{dt^2} = m_\alpha g + \frac{V_\alpha \beta}{(1 - \epsilon)} (\mathbf{u} - \mathbf{v}_\alpha) - V_\alpha \nabla p + F_{contact, \alpha}, \quad (3.1)$$

where \mathbf{v}_α is the velocity and \mathbf{x}_α is the position vector of the particle α . The first three terms on the right hand side of the equation are due to external forces acting on the particles, while the fourth term is due to particle collisions. The first term on the right hand side is due to gravity. The second term is due to the drag force where β represents an inter-phase momentum exchange coefficient as it usually appears in two-fluid models. The third term is the pressure gradient and the fourth term is due to contact forces, i.e. hard sphere collisions.

The angular momentum of the particles is computed with

$$I_\alpha \frac{d\boldsymbol{\omega}_\alpha}{dt} = T_\alpha, \quad (3.2)$$

where T_α is the torque and I_α is the moment of inertia. The moment of inertia for the spherical particles with radius R_α is equal to $I_\alpha = \frac{2}{5}m_\alpha R_\alpha^2$.

The inter-phase momentum transfer coefficient β is frequently modelled by combining the Ergun (13) equation for dense regimes ($\epsilon < 0.8$)

$$F_{Ergun} = \frac{\beta d_\alpha^2}{\mu} = 150 \frac{(1 - \epsilon)^2}{\epsilon} + 1.75(1 - \epsilon)Re_\alpha, \quad (3.3)$$

and the correlation proposed by Wen and Yu (53) for more dilute regimes ($\epsilon > 0.8$)

$$F_{Wen,Yu} = \frac{\beta d_\alpha^2}{\mu} = \frac{3}{4}C_d Re_\alpha (1 - \epsilon)\epsilon^{-2.65}. \quad (3.4)$$

The drag coefficient C_d is a function of the particle Reynolds number

$$C_d = \begin{cases} \frac{24}{Re_\alpha} (1 + 0.15(Re_\alpha)^{0.687}) & \text{if } Re_\alpha < 1000 \\ 0.44 & \text{if } Re_\alpha \geq 1000 \end{cases}.$$

The particle Reynolds number in this case is defined as

$$Re_\alpha = \frac{\epsilon \rho |\mathbf{u} - \mathbf{v}_\alpha| d_\alpha}{\mu},$$

where d_α is the diameter of the particle α and μ is the viscosity of the gas.

Normally segregation occurs due to the difference in size or density of the particles. This phenomenon occurs due to difference in drag force and/or gravity. As a result of this difference, defluidization occurs in the fluidized beds. Small/low density particles will move to the top of the layers and large/high density particles moves to the bottom layers of the bed.

The present CFD models are not able to predict it accurately. The present coefficients are not valid for a wide range of particle diameters, densities, etc. Recently a new coefficient was proposed by Beetstra et al. (3), which is obtained based on lattice Boltzmann simulations. This corrected coefficient gives better results for polydisperse particle systems, which accounts for the effect of the drag coefficient for polydispersity. The new drag coefficient is given as

$$F_i(\epsilon, \langle Re \rangle) = (\epsilon y_i + (1 - \epsilon)y_i^2 + 0.064\epsilon y_i^3) F(\epsilon, \langle Re \rangle) \quad (3.5)$$

where $y_i = \frac{d_i}{\langle d \rangle}$, $\langle Re \rangle = \frac{\rho \mathbf{u} \langle d \rangle}{\mu}$, $\frac{1}{\langle d \rangle} = \sum_i \frac{\xi_i}{d_i}$, with ξ_i is the mass fraction of the class i . In the equation (3.5), $F(\epsilon, \langle Re \rangle)$ is the normalised drag force of a monodisperse system at the same porosity and at Reynolds number $\langle Re \rangle$. This new $F(\epsilon, \langle Re \rangle)$ is given as

$$F_{Beetstra} = 10 \frac{1 - \epsilon}{\epsilon^2} + \epsilon^2 \left(1 + 1.5\sqrt{1 - \epsilon} \right) + \frac{0.413Re}{24\epsilon^2} \left(\frac{\epsilon^{-1} + 3\epsilon(1 - \epsilon) + 8.4Re^{-0.343}}{1 + 10^{3\phi} Re^{-0.5-2\phi}} \right) \quad (3.6)$$

where $\phi = 1 - \epsilon$, $Re = \frac{\rho \mathbf{U}(d)}{\mu}$ and \mathbf{U} is the relative velocity between a particle and the fluid flow.

In the segregation process we have the formation of particle layers. As a result of this we expect more collisions among the neighbour classes compared to far neighbour classes.

3.3 The gas-phase

The gas-phase hydrodynamics are calculated from the volume-averaged Navier-Stokes equations.

Continuity equation of gas phase:

$$\frac{\partial(\epsilon\rho)}{\partial t} + \nabla \cdot (\epsilon\rho\mathbf{u}) = 0. \quad (3.7)$$

Momentum equation of gas phase:

$$\frac{\partial(\epsilon\rho\mathbf{u})}{\partial t} + \nabla \cdot (\epsilon\rho\mathbf{u} \otimes \mathbf{u}) = -\epsilon\nabla p - \nabla \cdot (\epsilon\boldsymbol{\tau}) - S + \epsilon\rho\mathbf{g}. \quad (3.8)$$

In the present work we considered an isothermal system, i.e. constant temperature. The three-dimensional motion which implies that four basic variables have to be specified. The four basics variables in this model are the pressure, p and the three velocity components of the gas-phase, u_x , u_y and u_z . The void fraction ϵ , and the momentum exchange source term S are obtained from solid phase and will be explained in the Section 3.4.

The gas-phase density ρ is related to the pressure p and the gas temperature T by the ideal gas law

$$\rho = \left(\frac{M}{RT} \right) p, \quad (3.9)$$

where R is the gas constant and M is the average molecular weight of air.

The viscous stress tensor $\boldsymbol{\tau}$ is assumed to depend only on the gas motion. The general form for a Newtonian fluid has been implemented as

$$\boldsymbol{\tau} = - \left[\left(\lambda - \frac{2}{3}\mu \right) (\nabla \cdot \mathbf{u}) \mathbf{I} + \mu ((\nabla \mathbf{u}) + (\nabla \mathbf{u})^T) \right],$$

where the bulk viscosity λ can be set to zero for gases and μ is the gas phase shear viscosity. The constant \mathbf{I} denotes the unit tensor.

Remark 3.1 *Note that no turbulence modelling was taken into account. For bubbling beds this can be justified since the turbulence is damped out in the bed due to the very high solid fraction.*

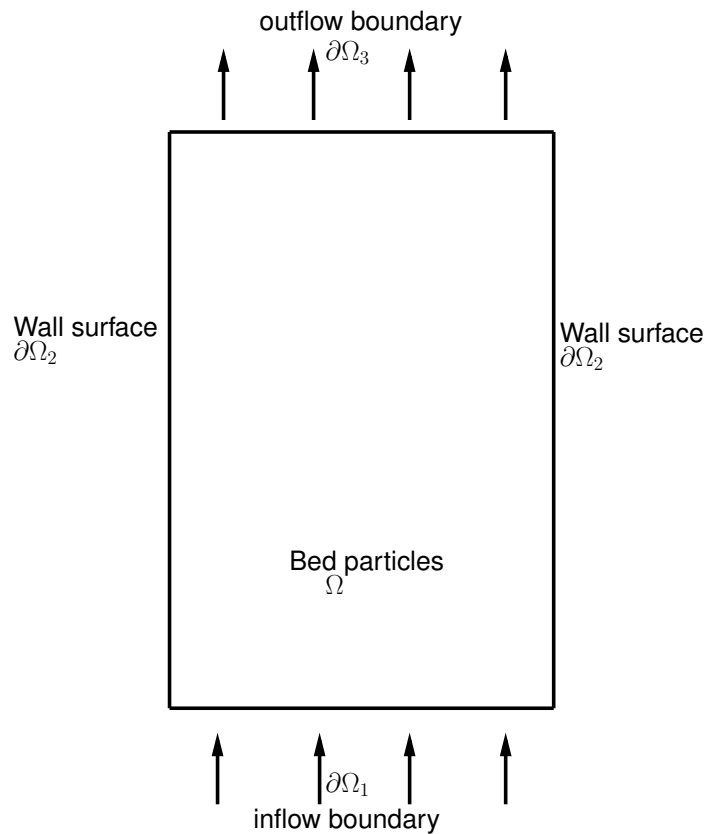


Figure 3.2: Initial and boundary conditions

3.3.1 Initial and boundary conditions

Initial conditions for Newtons equations of motion:

$\mathbf{x}_\alpha(0) \in \Omega$ and $\dot{\mathbf{x}}_\alpha(0) \in \mathbb{R}^3$.

Boundary conditions for Newtons equations of motion:

Elastic reflections of $\mathbf{x}_\alpha \in \partial\Omega (= \cup_{i=1}^3 \partial\Omega_i)$.

Initial conditions for Navier-Stokes equations:

$\mathbf{u}(0, x) = \mathbf{u}_0(x)$ and $p(0, x) = p_0(x)$ are given functions.

Boundary conditions for Navier-Stokes equations:

$\mathbf{u}|_{\partial\Omega_2} = 0$, $\mathbf{u}|_{\partial\Omega_1}$ is a given function.

3.4 Two-way coupling

An important issue in granular dynamics simulations of two-phase flow is the two-way coupling. The equations for the gas-phase are coupled with those of the particle phase through the calculation of porosity and the inter-phase momentum exchange. All relevant quantities should be averaged over a volume, which is large compared to the size of the particles, and in such a way that they are independent of the Eulerian grid size. In the following paragraph it is explained how two-way coupling is achieved in the model used in this work.

The two-way coupling between the gas-phase and the particles is enforced via the sink term S in the momentum equations of the gas-phase, which is computed from

$$S = \frac{1}{V_{cell}} \int_{V_{cell}} \sum_{\alpha=0}^{N_{\alpha}} \frac{V_{\alpha}\beta}{(1-\epsilon)} (\mathbf{u} - \mathbf{v}_{\alpha}) D(\mathbf{x} - \mathbf{x}_{\alpha}) dV, \quad (3.10)$$

where V_{cell} is the volume of the Eulerian grid cell. The distribution function D ensures that the reaction force acts as a point force at the position of the particle in the system. In the numerical implementation this force per volume term is distributed to the four nearest grid nodes using the area weighted averaging technique described in Section 3.5.

A straightforward method for the calculation of the porosity was given by Hoomans (20). In his work, the porosity in an Eulerian cell is calculated as follows

$$\epsilon_{cell} = 1 - \frac{1}{V_{cell}} \sum_{\forall i \in cell} f_{cell}^i V_{\alpha}^i, \quad (3.11)$$

where f_{cell}^i is the fractional volume of particle i residing in the cell under consideration. This method works well when the size of the grid cells is much larger than that of the particles, i.e. $V_{cell} \gg V_{\alpha}$.

From a numerical point of view, sometimes it is desirable to obtain a grid-independent solution. To resolve this, it is required to use small computational cells in order to resolve all relevant details of the gas flow field. Unfortunately, the method of Hoomans (20) generates problems once V_{cell} approaches V_{α} . That is, computational cells can be fully occupied by a particle, which leads to numerical problems. The calculation of the porosity and the two-way coupling between the gas-phase and the particles through the fluid-particle interactions requires the ratio between the size of the computational grid cells and the size of the particles to be large. To overcome these contradictory demands regarding the computational grid Link et al. (33) developed an alternative inter-phase coupling method for the DPM.

In this method the porosity and the force exerted by the gas-phase on the particles are calculated in a grid-independent manner, thus allowing a sufficiently fine solution of the gas flow field. Link et al. (33) represent the particles as porous cubes, where this geometry was selected because of

its computational advantages.

The diameter of the cube depends on the particle diameter and a constant factor a . The constant factor a is defined as the ratio between the cube and particle diameter.

$$a = \frac{d_{cube}}{d_\alpha} \quad (3.12)$$

The volume of the cube should be larger than or equal to the volume of the particle, resulting in

$$a \geq \left(\frac{\pi}{6}\right)^{\frac{1}{3}} \approx 0.8. \quad (3.13)$$

In practice, a typically takes a value from 3 to 5. In the numerical implementation, we had this a as a parameter of the window function. The porosity of a porous cube representing a particle can be easily calculated as

$$\epsilon_{cube} = \frac{V_\alpha}{V_{cube}} = \frac{\pi}{6a^3}.$$

Finally, the porous cube representation can be used to calculate the gas fraction in a computational cell in a manner analogous to the equation (3.11) as

$$\epsilon_{cell} = 1 - \epsilon_{cube} \sum_{\forall i \in cell} f_{cell}^i, \quad (3.14)$$

where f_{cell}^i is the volume fraction of the cell under consideration that is occupied by the cube i .

The incorporation of the cube representation to the model eliminates some problems, but also introduces a new problem. Near the wall, the cube can overlap with the wall. The cube is not allowed to overlap with the wall because the particles do not interact with the wall except for collisions.

The solution for this problem is to mirror the part of the cube back over the wall. The details and implementation issues of this mirroring procedure for various possible cases are explained in (16).

3.4.1 Hard sphere collision model

The collision model described in this simulation is based on the hard-sphere model developed by Hoomans et al. (20), which considers the binary interactions of the spherical particles. In this model it is assumed that the interaction forces are impulsive and therefore all other finite forces are negligible during a collision.

Consider two colliding spherical particles a and b with position vectors \mathbf{x}_a and \mathbf{x}_b having radii R_a and R_b , see 5.3. The particle velocities prior-to-collision are indicated by the subscript 0 and the relative velocity at the contact point c is defined as follows

$$\mathbf{v}_{ab} := \mathbf{v}_{a,c} - \mathbf{v}_{b,c} = (\mathbf{v}_a - \mathbf{v}_b) - (R_a\omega_a + R_b\omega_b) \times \mathbf{n}_{ab}. \quad (3.15)$$

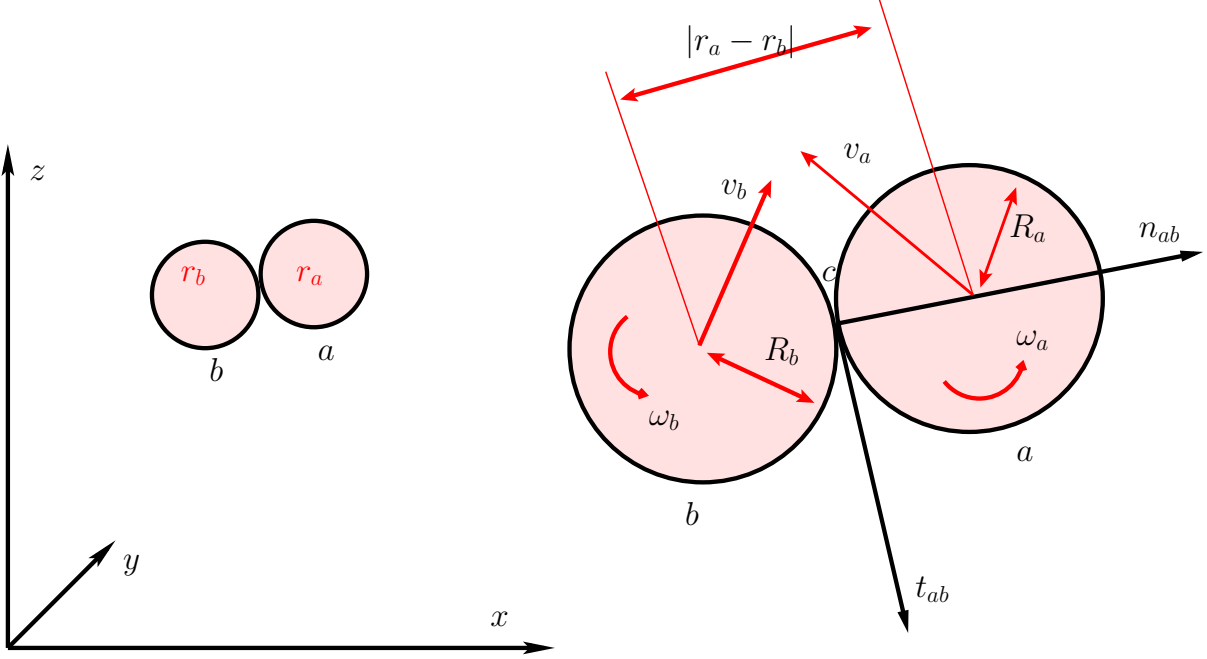


Figure 3.3: Hard sphere collision model

The normal and tangential unit vectors are respectively defined as

$$\mathbf{n}_{ab} = \frac{\mathbf{x}_a - \mathbf{x}_b}{|\mathbf{x}_b - \mathbf{x}_a|} \quad (3.16)$$

$$\mathbf{t}_{ab} = \frac{\mathbf{v}_{ab,0} - \mathbf{n}_{ab} \cdot \mathbf{v}_{ab,0}}{|\mathbf{v}_{ab,0} - \mathbf{n}_{ab} \cdot \mathbf{v}_{ab,0}|}. \quad (3.17)$$

As defined in Hoomans (20, p.33) "For a binary collision of these spheres, the following equations can be derived by applying Newton's second and third laws

$$m_a(\mathbf{v}_a - \mathbf{v}_{a,0}) = -m_b(\mathbf{v}_b - \mathbf{v}_{b,0}) = \mathbf{J}, \quad (3.18)$$

$$\frac{\mathbf{I}_a}{R_a}(\omega_a - \omega_{a,0}) = -\frac{\mathbf{I}_b}{R_b}(\omega_b - \omega_{b,0}) = -\mathbf{n}_{ab} \times \mathbf{J}. \quad (3.19)$$

The moment of inertia of a particle of mass m , radius R is given by

$$I = \frac{2}{5}mR^2. \quad (3.20)$$

The equations (3.18) and (3.19) can be rearranged to obtain

$$\mathbf{v}_{ab} - \mathbf{v}_{ab,0} = \frac{7\mathbf{J} - 5\mathbf{n}_{ab}(\mathbf{J} \cdot \mathbf{n}_{ab})}{2m_{ab}}, \quad (3.21)$$

where m_{ab} is the reduced mass given by

$$m_{ab} = \left(\frac{1}{m_a} + \frac{1}{m_b} \right)^{-1}. \quad (3.22)$$

In order to calculate the post-collision velocities, a closure model consisting of three parameters is used to describe the impulse vector \mathbf{J} .

The first parameter is the coefficient of (normal) restitution ($0 \leq e_n \leq 1$),

$$\mathbf{v}_{ab} \cdot \mathbf{n}_{ab} = -e_n(\mathbf{v}_{ab,0} \cdot \mathbf{n}_{ab}). \quad (3.23)$$

The second parameter is the coefficient of (dynamic) friction ($\mu \geq 0$),

$$|\mathbf{n}_{ab} \times \mathbf{J}| = -\mu(\mathbf{n}_{ab} \cdot \mathbf{J}). \quad (3.24)$$

The third parameter is the coefficient of tangential restitution ($0 \leq \beta_0 \leq 1$),

$$\mathbf{n}_{ab} \times \mathbf{v}_{ab} = -\beta_0(\mathbf{n}_{ab} \times \mathbf{v}_{ab,0}). \quad (3.25)$$

Following (20, p.36), "Combining equations (3.21) and (3.23) yields the following expression for the normal component of the impulse vector:

$$\mathbf{J}_n = -(1 + e_n)m_{ab}(\mathbf{v}_{ab,0} \cdot \mathbf{n}_{ab}). \quad (3.26)$$

For the tangential component, two types of collisions can be distinguished that are called *sticking* and *sliding*. If the tangential component of the relative velocity is sufficiently high in comparison to the coefficients of friction and tangential restitution that gross sliding occurs throughout the whole duration of the contact, the collision is of the *sliding* type. The non-sliding collisions are of the *sticking* type. When β_0 is equal to zero the tangential component of the relative velocity becomes zero during a *sticking* collision. When β_0 is greater than zero in such a collision, reversal of the tangential component of the relative velocity will occur. The criterion to determine the type of collision is as follows:

$$\begin{aligned} \mu \mathbf{J}_n &\geq \frac{2}{7}(1 + \beta_0)m_{ab}(\mathbf{v}_{ab,0} \cdot \mathbf{t}_{ab}) && \text{sticking,} \\ \mu \mathbf{J}_n &< \frac{2}{7}(1 + \beta_0)m_{ab}(\mathbf{v}_{ab,0} \cdot \mathbf{t}_{ab}) && \text{sliding.} \end{aligned}$$

For collisions of the *sticking* type, the tangential impulse is given by:

$$\mathbf{J}_t = -\frac{2}{7}(1 + \beta_0) \times m_{ab}(\mathbf{v}_{ab,0} \cdot \mathbf{t}_{ab}). \quad (3.27)$$

For collisions of the *sliding* type, the tangential impulse is given by:

$$\mathbf{J}_t = -\mu \mathbf{J}_n. \quad (3.28)$$

The total impulse vector is then simply obtained by addition:

$$\mathbf{J} = \mathbf{J}_n \mathbf{n} + \mathbf{J}_t \mathbf{t}. \quad (3.29)$$

The post-collision velocities can now be calculated from the equations (3.18) and (3.19).

In particle-wall collisions the mass of particle b (i.e. the wall) is infinitely large which makes all terms $\frac{1}{m_b}$ equal to zero. It is possible to implement a moving/rotating wall through the velocity vectors \mathbf{v}_b and ω_b but in the simulations performed for this work these velocities are all set equal to zero."

The particle collision characteristics play an important role in the overall system behaviour, as was shown by Hoomans et al. (21) and Goldschmidt (17). Hoomans (20) studied the effect of the particles properties on the hydrodynamics of fluidized beds with homogeneous inflow conditions. Influence of the coefficient of normal restitution e_n , friction μ and coefficient of tangential restitution β_0 on the fluidized bed for the two extreme cases $e_n = 1.0, \mu = 0.0$ (ideal) and $e_n = 0.9, \mu = 0.3$ (non-ideal) were studied.

Therefore realistic collision properties of the particles are supplied to the model, i.e. the coefficient of the normal and tangential restitution are respectively set to $e_n = 0.97$ and $\beta_0 = 0.1$, and the coefficient of friction is set to $\mu = 0.3$. The values of the collision parameters for particle-particle collisions were taken to be equal for particle-wall collisions. The influence of the particle-wall interaction on the overall bed hydrodynamics was investigated as well. This influence was found to be negligible. The trends observed in the pseudo 2-D simulations are clearly confirmed in the 3-D simulations for the above parameters.

3.5 Numerical calculations

The numerical solution strategy applied to this model follows Hoomans (20). The flow diagram of the numerical strategy is explained in the Figure 3.5. We used two different time steps for two phases. For solving the continuous phase equations and the coupling terms, we use a constant time step δt_{flow} . While for particle-particle interaction a different time step is used, which depends on the particle collision model, usually it is smaller than δt_{flow} .

Apart from the existing code, we introduced a new subroutine as shown in the dotted box 3B of the Figure 3.5. In this new subroutine 3B, we calculated the collisions among the particles of different and the same size classes. We made proper modifications to the initial input box 1, according to the initial particle size distribution strategies. Different initial particle sizes for pseudo 2-D and 3-D bed simulations are explained in the Chapter 5. We modified the code in the fluid-particle interaction box 2, with the new drag coefficient given in Section 3.2.

For integration of Newton's equations of motion, an explicit first order scheme is used to update

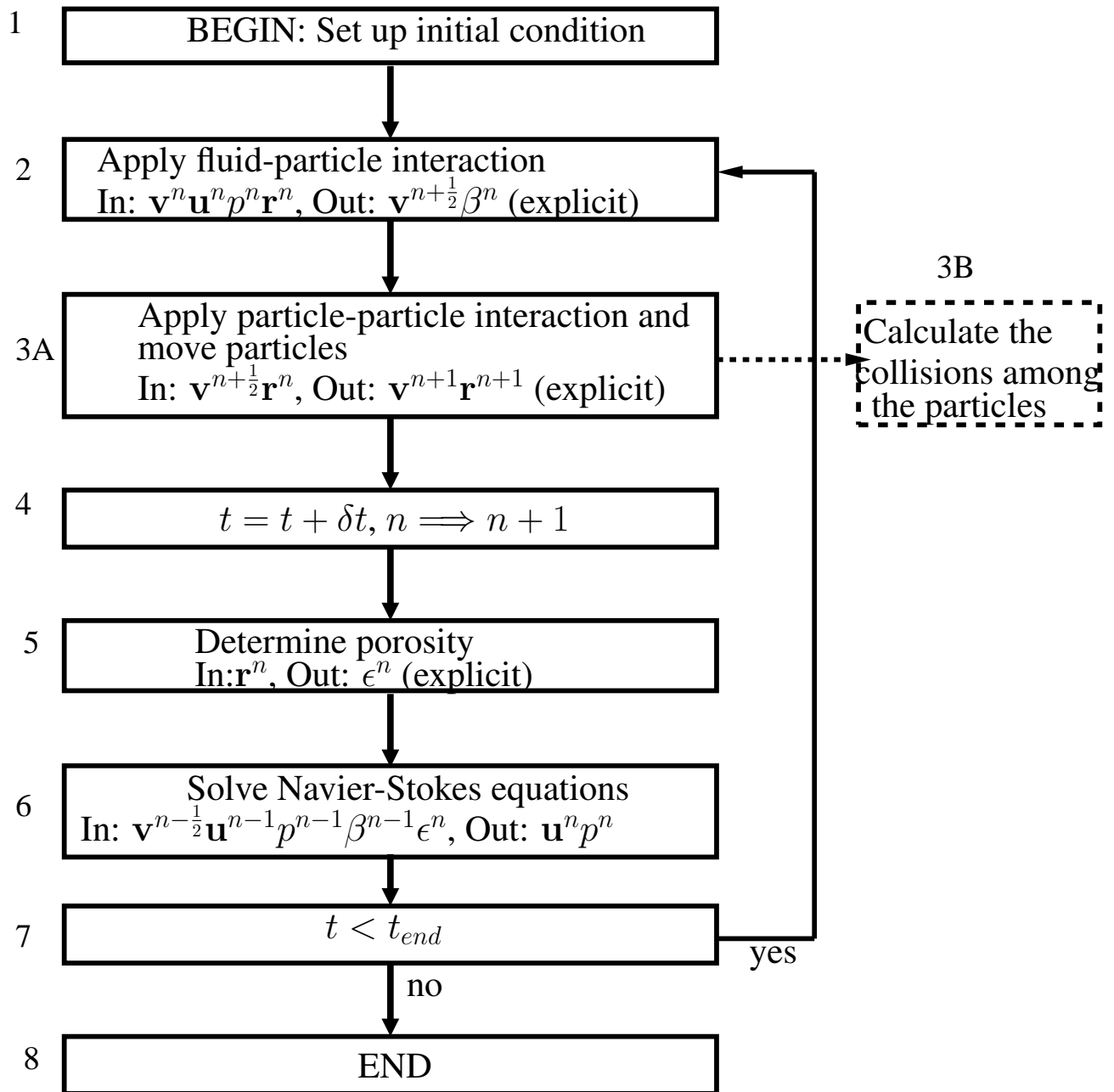


Figure 3.4: Flow diagram of the discrete particle model

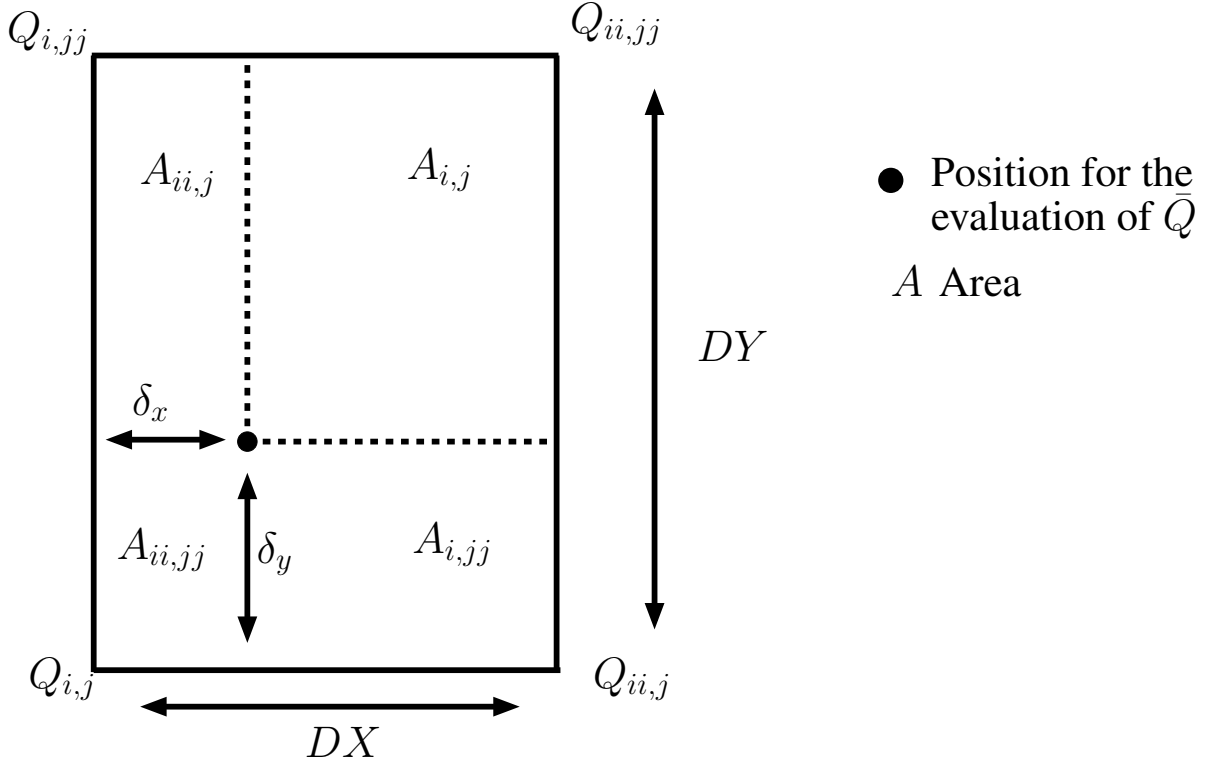


Figure 3.5: Area weighted averaging (20, p.68)

the velocities and the positions

$$\mathbf{v}_\alpha = \mathbf{v}_{\alpha,0} + \left(\frac{d\mathbf{v}_\alpha}{dt} \right) dt \quad (3.30)$$

$$\mathbf{x}_\alpha = \mathbf{x}_{\alpha,0} + (\mathbf{v}_\alpha)dt. \quad (3.31)$$

The right hand side of the Newton equations are calculated by using an area weighted averaging technique. In this technique we obtain the local averaged value \bar{Q} of a quantity $Q(i, j)$ from the four surrounding computational nodes as shown in Figure 3.5.

Based on Hoomans (20, p.67) "The local averaged value is calculated as follows

$$\bar{Q} = \frac{A_{i,j}Q_{i,j} + A_{ii,j}Q_{ii,j} + A_{ii,jj}Q_{ii,jj} + A_{i,jj}Q_{i,jj}}{DXY} \quad (3.32)$$

where

$$\begin{aligned} A_{i,j} &= (DX - \delta_x)(DY - \delta_y) \\ A_{ii,j} &= \delta_x(DY - \delta_y) \\ A_{ii,jj} &= \delta_x\delta_y \\ A_{i,jj} &= (DX - \delta_x)\delta_y \end{aligned}$$

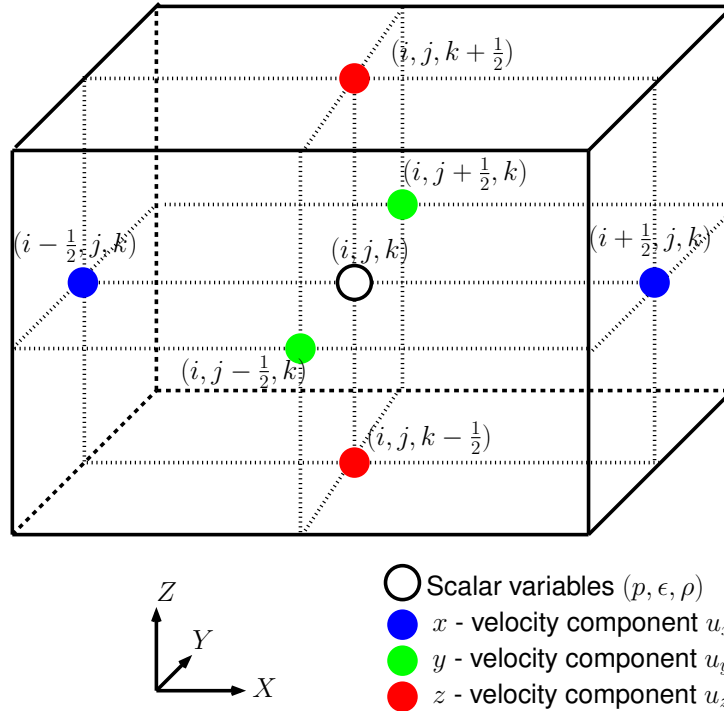


Figure 3.6: A typical computational cell in the staggered grid where key variables are evaluated

The distances δ_x and δ_y , necessary in this averaging technique, are calculated from the position of the particle in the staggered grid."

The flow solver is the most complicated function of this model, therefore it needs some more explanation. To solve the Navier-Stokes equations for the gas phase a standard finite difference technique, employing a staggered grid to improve numerical stability, is used. The cells are labelled by indices i , j , and k located at their centers and a staggered grid configuration is applied. According to this configuration the scalar variables, pressure p , porosity ϵ and the density of the gas ρ are defined at the cell centers whereas the velocity components u_x , u_y and u_z are defined at the cell faces, as indicated in the Figure 3.5.

The Navier-Stokes equations are solved using the SIMPLE algorithm (38). An ICCG solver is used to solve the sparse matrices. The main steps of the numerical scheme applied is given below.

We discretize the continuity equation (3.7) with a first-order time differencing and treating the

convective fluxes implicitly as

$$\begin{aligned}
(\epsilon\rho)_{i,j,k}^{n+1} - (\epsilon\rho)_{i,j,k}^n &+ \frac{\delta t}{\delta x} \left\{ \langle \epsilon\rho u_x \rangle_{i+\frac{1}{2},j,k}^{n+1} - \langle \epsilon\rho u_x \rangle_{i-\frac{1}{2},j,k}^{n+1} \right\} \\
&+ \frac{\delta t}{\delta y} \left\{ \langle \epsilon\rho u_y \rangle_{i,j+\frac{1}{2},k}^{n+1} - \langle \epsilon\rho u_y \rangle_{i,j-\frac{1}{2},k}^{n+1} \right\} \\
&+ \frac{\delta t}{\delta z} \left\{ \langle \epsilon\rho u_z \rangle_{i,j,k+\frac{1}{2}}^{n+1} - \langle \epsilon\rho u_z \rangle_{i,j,k-\frac{1}{2}}^{n+1} \right\} = 0,
\end{aligned} \tag{3.33}$$

where n and $n + 1$ represents the old and new time level respectively.

The momentum equation (3.8) for the gas phase is discretized in the direction of x as

$$(\epsilon\rho u_x)_{i+\frac{1}{2},j,k}^{n+1} = A_{i+\frac{1}{2},j,k}^n + \epsilon_{i+\frac{1}{2},j,k}^{n+1} \frac{\delta t}{\delta x} (p_{i,j,k}^{n+1} - p_{i+1,j,k}^{n+1}) - \Delta t \beta_{i+\frac{1}{2},j,k}^n u_x^{n+1}. \tag{3.34}$$

The pressure and velocity terms are calculated implicitly, the stresses, gravity and a part of the drag is taken into account explicitly,

$$\begin{aligned}
A_{i+\frac{1}{2},j,k}^n &= (\epsilon\rho u_x)_{i+\frac{1}{2},j,k}^n + \frac{\delta t}{\delta x} \left\{ \langle \epsilon\rho u_x u_x \rangle_{i,j,k}^n - \langle \epsilon\rho u_x u_x \rangle_{i+1,j,k}^n \right\} \\
&+ \frac{\delta t}{\delta y} \left\{ \langle \epsilon\rho u_y u_x \rangle_{i+\frac{1}{2},j-\frac{1}{2},k}^n - \langle \epsilon\rho u_y u_x \rangle_{i+\frac{1}{2},j+\frac{1}{2},k}^n \right\} \\
&+ \frac{\delta t}{\delta z} \left\{ \langle \epsilon\rho u_z u_x \rangle_{i+\frac{1}{2},j,k-\frac{1}{2}}^n - \langle \epsilon\rho u_z u_x \rangle_{i+\frac{1}{2},j,k+\frac{1}{2}}^n \right\} \\
&+ \frac{\delta t}{\delta x} \left\{ (\epsilon(\lambda - \frac{2}{3}\mu))_{i+1,j,k}^n \left(\frac{(u_x)_{i+\frac{3}{2},j,k}^n - (u_x)_{i+\frac{1}{2},j,k}^n}{\delta x} + \frac{(u_y)_{i+1,j+\frac{1}{2},k}^n - (u_y)_{i+1,j-\frac{1}{2},k}^n}{\delta y} + \frac{(u_z)_{i+1,j,k+\frac{1}{2}}^n - (u_z)_{i+1,j,k-\frac{1}{2}}^n}{\delta z} \right) \right. \\
&\quad \left. - (\epsilon(\lambda - \frac{2}{3}\mu))_{i,j,k}^n \left(\frac{(u_x)_{i+\frac{1}{2},j,k}^n - (u_x)_{i-\frac{1}{2},j,k}^n}{\delta x} + \frac{(u_y)_{i,j+\frac{1}{2},k}^n - (u_y)_{i,j-\frac{1}{2},k}^n}{\delta y} + \frac{(u_z)_{i,j,k+\frac{1}{2}}^n - (u_z)_{i,j,k-\frac{1}{2}}^n}{\delta z} \right) \right\} \\
&+ 2 \frac{\delta t}{(\delta x)^2} \left\{ (\epsilon\mu)_{i+1,j,k}^n \left((u_x)_{i+\frac{3}{2},j,k}^n - (u_x)_{i+\frac{1}{2},j,k}^n \right) - (\epsilon\mu)_{i,j,k}^n \left((u_x)_{i+\frac{1}{2},j,k}^n - (u_x)_{i-\frac{1}{2},j,k}^n \right) \right\} \\
&+ \frac{\delta t}{\delta y} \left\{ (\epsilon\mu)_{i+\frac{1}{2},j+\frac{1}{2},k}^n \left(\frac{(u_x)_{i+\frac{1}{2},j+1,k}^n - (u_x)_{i+\frac{1}{2},j,k}^n}{\delta y} + \frac{(u_y)_{i+1,j+\frac{1}{2},k}^n - (u_y)_{i,j+\frac{1}{2},k}^n}{\delta x} \right) \right. \\
&\quad \left. - (\epsilon\mu)_{i+\frac{1}{2},j-\frac{1}{2},k}^n \left(\frac{(u_x)_{i+\frac{1}{2},j,k}^n - (u_x)_{i+\frac{1}{2},j-1,k}^n}{\delta y} + \frac{(u_y)_{i+1,j-\frac{1}{2},k}^n - (u_y)_{i,j-\frac{1}{2},k}^n}{\delta x} \right) \right\} \\
&+ \frac{\delta t}{\delta z} \left\{ (\epsilon\mu)_{i+\frac{1}{2},j,k+\frac{1}{2}}^n \left(\frac{(u_z)_{i+1,j,k+\frac{1}{2}}^n - (u_z)_{i,j,k+\frac{1}{2}}^n}{\delta x} + \frac{(u_x)_{i+\frac{1}{2},j,k+1}^n - (u_x)_{i+\frac{1}{2},j,k}^n}{\delta z} \right) \right. \\
&\quad \left. - (\epsilon\mu)_{i+\frac{1}{2},j,k-\frac{1}{2}}^n \left(\frac{(u_z)_{i+1,j,k-\frac{1}{2}}^n - (u_z)_{i,j,k-\frac{1}{2}}^n}{\delta x} + \frac{(u_x)_{i+\frac{1}{2},j,k}^n - (u_x)_{i+\frac{1}{2},j,k-1}^n}{\delta z} \right) \right\} \\
&+ \delta t \cdot (\epsilon\rho)_{i+\frac{1}{2},j,k}^n \cdot g_x + \delta t \beta_{i+\frac{1}{2},j,k}^n (v_x)_{i+\frac{1}{2},j,k}^{n+1}.
\end{aligned}$$

The value of $\epsilon\mu$ at a cell is calculated by averaging neighbour cell values as,

$$\begin{aligned}
(\epsilon\mu)_{i+\frac{1}{2},j+\frac{1}{2},k} &= \frac{(\epsilon\mu)_{i,j,k}^n + (\epsilon\mu)_{i+1,j,k}^n + (\epsilon\mu)_{i+1,j+1,k}^n + (\epsilon\mu)_{i,j+1,k}^n}{4} \\
(\epsilon\mu)_{i+\frac{1}{2},j,k} &= \frac{(\epsilon\mu)_{i,j,k}^n + (\epsilon\mu)_{i+1,j,k}^n}{2} \quad \text{etc.}
\end{aligned}$$

In a similar manner we can discretize the momentum equation in the y and z directions.

Solution of the finite difference equations

The numerical solution of the discretized equations evolves through a sequence of computational cycles, or time steps. For each computational cycle the advanced $(n + 1)$ -level values have to be calculated through the entire computational domain using the old n -level values. Each computational cycle consists of two distinct phases:

- Calculation of explicit terms A^n , B^n and C^n in the momentum equation for all interior cells.
- Implicit computation of the pressure for the entire computational mesh with an iterative procedure. This implicit procedure consists of several steps.

The first step involves the calculation of mass residual D_f from the continuity equation as

$$\begin{aligned} (D_f)_{i,j,k}^* &= (\epsilon\rho)_{i,j,k}^* - (\epsilon\rho)_{i,j,k}^n + \frac{\delta t}{\delta x} \left\{ \langle \epsilon\rho u_x \rangle_{i+\frac{1}{2},j,k}^* - \langle \epsilon\rho u_x \rangle_{i-\frac{1}{2},j,k}^* \right\} \\ &+ \frac{\delta t}{\delta y} \left\{ \langle \epsilon\rho u_y \rangle_{i,j+\frac{1}{2},k}^* - \langle \epsilon\rho u_y \rangle_{i,j-\frac{1}{2},k}^* \right\} \\ &+ \frac{\delta t}{\delta z} \left\{ \langle \epsilon\rho u_z \rangle_{i,j,k+\frac{1}{2}}^* - \langle \epsilon\rho u_z \rangle_{i,j,k-\frac{1}{2}}^* \right\}, \end{aligned} \quad (3.35)$$

where the superscript (*) refers to the most recently obtained values. If the convergence criterion

$$(D_f)_{i,j,k}^* < eps \cdot (\epsilon\rho)_{i,j,k}^*$$

is not satisfied for all interior computational cells, then a whole field pressure correction is calculated as

$$\begin{aligned} J_{i-1,j,k}^n \delta p_{i-1,j,k}^{new} &+ J_{i+1,j,k}^n \delta p_{i+1,j,k}^{new} + J_{i,j-1,k}^n \delta p_{i,j-1,k}^{new} + J_{i,j+1,k}^n \delta p_{i,j+1,k}^{new} \\ &+ J_{i,j,k-1}^n \delta p_{i,j,k-1}^{new} + J_{i,j,k+1}^n \delta p_{i,j,k+1}^{new} + J_{i,j,k}^n \delta p_{i,j,k}^{new} = -(D_f)_{i,j,k}^* \end{aligned} \quad (3.36)$$

with J^n the Jacobi matrix at the old time level n . The Jacobi matrix contains the derivatives of D_f with respect to the pressure. An explicit expression can be obtained from the continuity equation in combination with the momentum equation.

$$J_{i,j,k} = \frac{\partial (D_f)_{i,j,k}^n}{\partial p_{i,j,k}^n} \quad \text{etc.}$$

Applying (3.36) for all internal computational cells results in a set of linear equations that can be assembled in the matrix form as

$$\mathbf{J}^n \cdot \delta \mathbf{p}^{new} = -\mathbf{D}^*. \quad (3.37)$$

To save computational effort the elements of the Jacobi matrix are evaluated at the old time level. The banded matrix problem corresponding to the equation (3.37) is solved using a standard ICCG sparse matrix technique. Once the pressure have been obtained, the corresponding new gas phase densities are calculated.

D_f can be calculated from the continuity equation with these new values of density, pressure as

$$\begin{aligned} (D_f)_{i,j,k}^{n+1} = (\epsilon\rho)_{i,j,k}^{n+1} - (\epsilon\rho)_{i,j,k}^n &+ \frac{\delta t}{\delta x} \left\{ \langle \epsilon\rho u_x \rangle_{i+\frac{1}{2},j,k}^{n+1} - \langle \epsilon\rho u_x \rangle_{i-\frac{1}{2},j,k}^{n+1} \right\} \\ &+ \frac{\delta t}{\delta y} \left\{ \langle \epsilon\rho u_y \rangle_{i,j+\frac{1}{2},k}^{n+1} - \langle \epsilon\rho u_y \rangle_{i,j-\frac{1}{2},k}^{n+1} \right\} \\ &+ \frac{\delta t}{\delta z} \left\{ \langle \epsilon\rho u_z \rangle_{i,j,k+\frac{1}{2}}^{n+1} - \langle \epsilon\rho u_z \rangle_{i,j,k-\frac{1}{2}}^{n+1} \right\}. \end{aligned} \quad (3.38)$$

Provided that the corresponding estimates of the mass residual (3.35) do not meet the convergence criteria simultaneously for all interior computational cells, the pressure correction equation (3.36) is again calculated using the updated velocity field to compute the mass residual D_f for all cells. This iterative process is repeated until the convergence criteria is satisfied or the specified maximum allowable number of iterations reached.

For calculation of the convective mass and momentum fluxes, a second order accurate method is applied to reduce numerical diffusion.

Chapter 4

Modelling of collision frequency functions using DPM

In this chapter we present an approach for the modelling of collision frequency functions in a fluidized bed. The aggregation kernel can be decomposed as the product of size dependent and size independent functions. The size dependent functions are known as collision frequency kernel and the size independent functions are known as aggregation efficiency functions. In this chapter we give a general expression for evaluating the size dependent collision frequency function from computer simulation results.

4.1 Introduction

In recent times, due to the improvement of the computations, some authors (15; 51) have tried to extract the kernels from discrete element method (DEM) simulations. Tan et al. (51) investigated an agglomeration kernel based on the principle of kinetic theory of granular flow to the fluidized bed melt granulation. Using the simulation results of the discrete particle model (DPM), the authors showed that the velocity distribution of the particles inside the fluidized bed are in good agreement with those expected according to kinetic theory of granular flow (KTGF). Based on this kinetic theory of granular flow they assumed that the collision rate function is analogous to the existing equi-partition kinetic energy (EKE) kernel. This EKE kernel was originally derived by Hounslow (22) and it was discussed in Chapter 2, Section 2.4.1. Tan et al. (51) tried to fit the particle size distribution of the experimental results with the discretized population balance modelling with EKE kernel.

Recently Gantt et al. (15) observed the shear kernel for high-shear granulation using discrete element method simulations. For the discrete element method simulations, they assumed that the particles are spherical in shape and applied the soft sphere model as particle collision mechanism. In these simulations, the authors used an aggregation kernel for deformable wet granules derived by Liu et al. (35). A multi-scale shear kernel with four parameters for aggregation efficiency function is calculated using regression fit to the simulation data. Gantt et al. (15) con-

sidered pore saturation, porosity, particle velocity and particle diameter as the parameters of the aggregation efficiency function and calculated these parameters for two different types of particle binding mechanisms.

In the following sections we present the modelling of the aggregation frequency function using the Discrete Particle Model (DPM), which is a microscopic model developed by Hoomans et al. (20).

4.2 Derivation of collision frequency functions

Aggregation processes lead to a reduction in the total number of particles and an increase in the average size. Therefore agglomeration leads a major change in the system as the time changes. As a result, the aggregation rate will be effected, which is a function of collision frequency function and aggregation efficiency. Here we are deriving an expression for collision frequency function.

Let $N_{i,j}$ be the number of collisions occurring per unit time per unit volume between the two classes of particles of volumes v_i and v_j . All particles are assumed to be spherical in shape, and collisions are treated as binary hard sphere collisions. The collision frequency function $K_{i,j}$ can be written in terms of concentrations of particles of volumes v_i and v_j as:

$$N_{i,j} = K_{i,j}n_in_j, \quad 1 \leq i, j \leq I$$

where n_i, n_j are the number concentrations of classes i, j . The number I denotes the total number of classes. The parameter $K_{i,j}$ is the frequency function among different classes i and j . The collision frequency function $K_{i,j}$ is a function of flow properties, i.e. particle size, gas velocity, temperature, etc.

The number of collisions occurring during time t_{sim} in the fluidized bed of volume V_{bed} is given as

$$N_{i,j}^{tot} = K_{i,j} \frac{N_i}{V_{bed}} \frac{N_j}{V_{bed}} t_{sim} V_{bed}, \quad (4.1)$$

where N_i, N_j are the number of particles of class i, j present in the fluidized bed of volume V_{bed} , i.e. $n_i = \frac{N_i}{V_{bed}}, n_j = \frac{N_j}{V_{bed}}$.

Remark 4.1 *In the experimental analysis of bed volume, it consists of the measurement of the height of the fluidized layer. From the fluid flow point of view, the bed void fraction is important. The bed contains “bubbles”, called parvoids, that do not contain particles. Since the upper surface of the bed remains neither perfectly plane nor motionless, due to particular parvoid motion, the measurement of the mean level is not accurate. In order to overcome this difficulty*

we propose a new measurement technique involving time averaging and the calculation of the mean height of the bed. The mean height of the particles is considered as the height of the fluidized bed and it is calculated as

$$h_{bed}^i = \frac{\sum_{\alpha=1}^{N_0} z_{\alpha}}{N_0}, \quad N_0 = \sum_{i=1}^I N_i, \quad t_{sim} = t_{step} * \Delta t$$

$$h_{mean} = \frac{1}{t_{step}} \sum_{i=1}^{t_{step}} h_{bed}^i$$

where z_{α} is the height of the particle α , t_{step} are the number of time steps and Δt is the time step. The volume of the bed is obtained by averaging it over the simulation time t_{sim}

$$V_{bed} = length \times depth \times h_{mean}.$$

From the Equation (4.1), the collision rate function is obtained as

$$K_{i,j} = \frac{N_{i,j}^{tot}}{N_i N_j} \cdot \frac{V_{bed}}{t_{sim}}. \quad (4.2)$$

In case of collisions within a size class, i.e. $i = j$, the collision rate function is obtained as

$$K_{i,i} = \frac{N_{i,i}^{tot}}{\frac{N_i(N_i-1)}{2}} \cdot \frac{V_{bed}}{t_{sim}} \quad (4.3)$$

which differs from the previous one due to the correction for self collisions of the particles, which was observed by Hu and Mei (24). The authors observed a deviation of about 2 percent in their simulations. This correction is negligible in the case of continuous spectrum, because of the assumption of large concentrations, in which, we take the approximation $N_i(N_i - 1)/2 \approx N_i^2/2$. The details of the derivation of (4.3) by using a combinatorial approach can be found in Sastry (47).

We obtain $N_{i,j}^{tot}$ from DPM simulation, by collecting the collisions among different classes i and j . We plotted the collisions among different classes i and j and we observed a larger number of collisions among bigger particles and fewer collisions among smaller particles as can be seen in Figure 4.1. This kind of behaviour is exhibited by a shear flow. Besides this the physical description of flow inside the bed, see Section 4.4, infers that the flow is a shear flow. Therefore we assumed that the collision rate function is shear kernel. We fitted the simulated values with this shear kernel defined as

$$K(x, y) = \eta \left(x^{\frac{1}{3}} + y^{\frac{1}{3}} \right)^3 \quad (4.4)$$

where η is the bed parameter to be fitted for the volumes of the particles x and y . The bed parameter η for various simulation conditions is described in the next chapter.

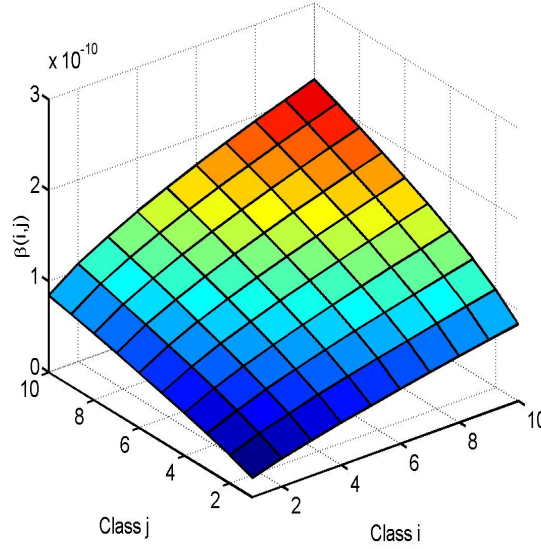


Figure 4.1: Particle collisions among different classes

4.3 Correction to the aggregation equation

Let us consider the combinatorial approach of the particle collisions among different classes and within the same class of particles. Here classes are based on the volume of the particle, i.e., $V_0, 2V_0, 3V_0, \dots$ and V_0 is the initial particle volume class.

The Figure 4.3 describes the number of possible collisions among two classes A and B which contain 2 and 3 particles respectively. The number of possible collisions between A and B are 6. The number of possible collisions among the particles of class B are 3.

We can generalize the above approach as follows. Suppose there are N_i particles of i th class and N_j particles of j th class at a given instant. Then the number of possible collisions among i th class and j th class are $N_i N_j$. When we have collisions among the particles of class i , then the number of possible collisions are $N_i(N_i - 1)/2$.

We can apply the above combinatorial approach to the fluidized bed as follows. Let $K_{i,j}$ be the collision frequency function of the fluidized bed. Then the number of collisions among the classes i and j per unit time and per unit volume are $N_{i,j} = K_{i,j} N_i N_j$. In case of collisions among the particles in the i th class are $N_{i,j} = K_{i,j} N_i(N_i - 1)/2$. The case of collisions among the same class are not considered during the derivation of the aggregation equation. So here we are showing the effect of this in modelling the aggregation kernel in Table 4.1. In this simulation

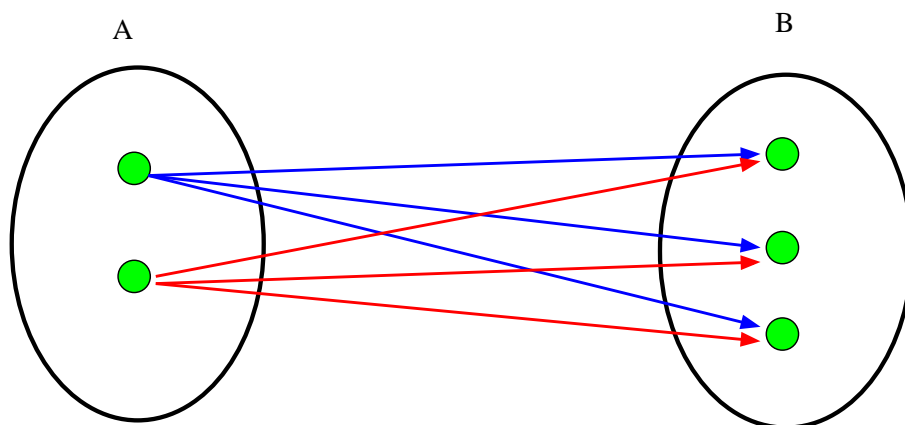


Figure 4.2: Combinatorial calculation of the particle collisions

| simulation | N_0 | Same size collisions 4.3 | Same size collisions 4.2 | Difference |
|------------|-------|--------------------------|--------------------------|------------|
| 1 | 5000 | 6.7155e-05 | 6.7088e-05 | 6.7155e-08 |
| 2 | 10000 | 1.6566e-05 | 1.6557e-05 | 8.2828e-09 |
| 3 | 15000 | 1.4514e-05 | 1.4509e-05 | 4.8379e-09 |
| 4 | 20000 | 1.1776e-05 | 1.1773e-05 | 2.9440e-09 |

Table 4.1: Simulations for same size collisions

we considered 10 classes of particles with an equal number of particles in each class. For details of initial conditions of the simulations see the Appendix B.2. We made simulations with an increasing the number of particles.

From the above simulation Table 4.1, we can observe that when the number of particles is high, i.e. N_0 is large enough, this new correction term has little effect on the aggregation equation. Therefore in industrial level fluidized beds the new correction is negligible, since the number of particles is very high.

4.4 Physical description of the flow pattern inside fluidized beds

The flow inside the bed is the most significant factor effecting the collision frequency of the particles, which affects the aggregation. So one needs to capture the flow pattern inside the bed. The physical description of the flow pattern inside the bed can be described by using the dimensionless quantity Reynolds number.

The particle Reynolds number is given as (54)

$$Re_\alpha = \frac{\epsilon \rho_g U_\alpha d_\alpha}{\mu}, \quad (4.5)$$

where $U_\alpha = |u - v_\alpha|$ is the relative velocity between a particle and the fluid flow. The particle Reynolds number is a function of particle diameter, velocity, porosity, density and viscosity.

The particle Reynolds number characterizes the flow regime inside the bed. Frequently used flow regimes are

- **The Stokes Regime:** The flow regime is Stokes regime if $Re_\alpha < 0.2$. The Stokes law regime is also known as creeping flow regime. In this regime, the viscosity of the fluid is dominating.
- **The Intermediate Regime:** The flow regime is known as intermediate regime if $0.2 < Re_\alpha < 500$. In this regime the drag force is a function of the particle's Reynolds number.
- **The Newton's Law Regime:** If $Re_\alpha > 500$. In this regime inertia of the fluid is larger than the viscosity of the fluid.

Recently a new methodology for calculating the agglomeration kernels was proposed by Steven (10) for the Stokes regime. He assumed uncertainty in the Stokes regime and evaluated the coefficients of uncertainty using a method proposed by Tatang (52). The newly postulated agglomeration kernel is given as

$$K(t, x, y) = K_0 \int_{-\infty}^{S_t^*} f(t, \phi) d\phi$$

where $f(t, \phi)$ is the discrete probability density function for the Stokes number, and S_t^* is the critical stokes number. The constant K_0 is determined from the experimental data.

In our DPM simulations the viscosity, density of the particles and gas velocity are constant with respect to time, the only varying variables are particle velocity and diameter for different sets of simulations. We studied the particle Reynolds number for a wide range particle diameters in order to understand the flow pattern inside the fluidized bed. It was observed that the particle Reynolds number always lies below 500 and above 100. This shows that the flow inside the bed is dominated by shear forces. From this microscopic/macroscopic observation, we can expect a shear kernel.

Chapter 5

Simulation results for modelling of aggregation kernels using DPM

In this chapter we describe the simulation results for modelling of aggregation kernels using the Discrete Particle Model (DPM) which is explained in Chapter 3. Section 1 explains the essential initial parameters for the simulations. The second and third sections show the simulation results for pseudo 3-D and 3-D fluidized beds. In these simulations we are trying to fit the simulation results with the shear kernel. We calculated the fitting parameter η for each simulation and named it the bed parameter. The influence of this bed parameter for various initial particle size distributions is analysed.

5.1 Initial parameters

Initial parameters play a significant role in the simulations of any model. All the major parameters used for our simulations are given in Appendix B.

5.1.1 Initial assumptions

In the present thesis we model the aggregation kernels with some assumptions and some simplifications of the discrete particle model for easy numerical calculations. Here in this section we explain those assumptions. We have the following assumptions in our simulations:

1. ***Particle size characterization***

The particle size is characterized by one or more linear dimensions. In the present simulations we considered an ideal particle like a sphere characterized by its diameter.

2. ***Particle collisions***

We considered binary hard sphere collisions among the particles. The particles collide according to the hard sphere collision model as explained in the Chapter 3, Section 4. The parameters of the collision model are given in the Appendix B.

3. *Basic particle size class: Volume based size class*

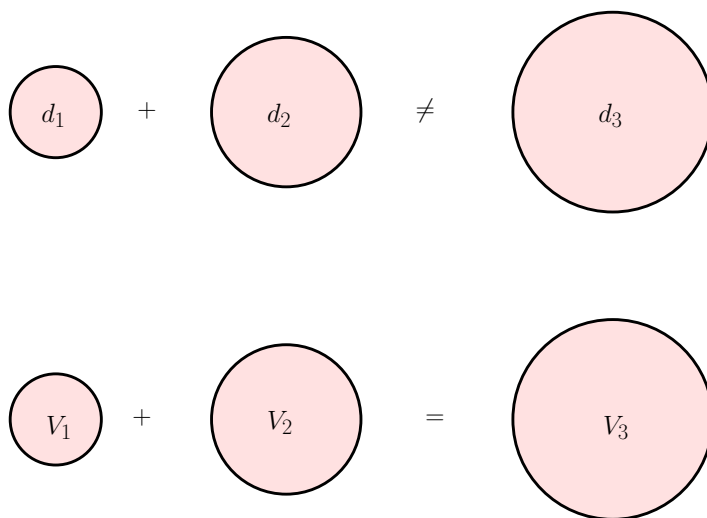


Figure 5.1: Schematic example for the choice of the volume based size class

It is necessary that population balance equation must be consistent with mass. This is satisfied automatically if we consider volume as the intrinsic particle property as suggested by Pouw et al. (40). Since volume is additive in a binary aggregation event, where as diameter is not. Figure 5.1 illustrates the obvious fact that the aggregation of particles of diameter $d_1 = 1$ and $d_2 = 2$ do not form a particle of diameter $d_3 = 1 + 2$, but particles of volumes $V_1 = 1$ and $V_2 = 2$ produce an agglomerate particle of volume $V_3 = 1 + 2$.

Therefore in the present simulations we considered volume based size classes with volumes $V_0, 2V_0, 3V_0, \dots$, where V_0 is the volume of the smallest particle in the system.

4. *No aggregation*

In these simulations no aggregation, compaction or breakage takes place. Only particle collisions due to gas flow are considered.

5.1.2 Initial particle size distributions

In most of the practical cases fluidized beds are consisting of particles of different sizes, known as *polydisperse* systems. Initial particle size distribution is very important in granulations process, since the final product is dependent on the initial size distribution. In this section we derive different particle size distributions satisfying certain properties.

Let us consider N_0 number of particles with N_i number of particles of classes $i = 1, 2, \dots, I$ with volume $V_0, 2V_0, 3V_0, \dots, IV_0$. Now we will determine different possible particle size distributions

based on different criteria. The following gives the different possible criteria and the particle size distributions.

1. Equal zeroth moment

We consider the first criterion satisfying equal zeroth moment in each class, i.e. the number of particles in each class i are equal and the total number of particles of all classes is N_0 ,

$$\begin{aligned} N_1 &= N_2 = \dots = N_I, \\ \sum_i N_i &= N_0. \end{aligned} \quad (5.1)$$

2. Equal length

Let L_1, L_2, \dots, L_I be the length of particles of classes 1, 2, ..., I . Consider the case satisfying the equal length criterion, i.e. the total length of the particles in each class i is equal and the total number of particles of all classes is N_0 ,

$$\begin{aligned} N_1 L_1 &= N_2 L_2 = \dots = N_I L_I, \\ \sum_i N_i &= N_0. \end{aligned} \quad (5.2)$$

3. Equal surface area

Let A_1, A_2, \dots, A_I be the length of particles of classes 1, 2, ..., I . Consider the case satisfying the equal surface area criterion, i.e. the total length of the particles in each class i is equal and the total number of particles of all classes is N_0 ,

$$\begin{aligned} N_1 A_1 &= N_2 A_2 = \dots = N_I A_I, \\ \sum_i N_i &= N_0. \end{aligned} \quad (5.3)$$

4. Equal first moment (Equal volume)

Let V_1, V_2, \dots, V_I be the length of particles of classes 1, 2, ..., I . We consider simulations satisfying the equal volume criteria, i.e. the total volume of the particles in each class i is equal and the total number of particles of all classes is N_0 ,

$$\begin{aligned} N_1 V_1 &= N_2 V_2 = \dots = N_I V_I, \\ \sum_i N_i &= N_0. \end{aligned} \quad (5.4)$$

5. Different number of particles

We calculate the particle size distribution satisfying the above four criteria 1-4 with different number of particles, i.e. $N_0 = 5000, 10000, 15000$.

6. Particles with three classes

The number of particles in each class N_i are determined with three number of classes, i.e. $I = 5, 10, 15$ for above four criteria 1-4.

7. Increasing volume of particles

We considered a particle size distributions satisfying the one of the above criteria 1-4 and then we increased the volume V_0 . That is the first simulation is started with $V_0, 2V_0, 3V_0, \dots, IV_0$, second simulation with $2V_0, 3V_0, \dots, (I + 1)V_0$, and so on.

| Simulation | Criteria | Number of particles |
|------------|----------|------------------------------|
| 1 | 1 | 2000, 2000, 2000, 2000, 2000 |
| 2 | 2 | 2701, 2144, 1873, 1702, 1580 |
| 3 | 3 | 3510, 2211, 1686, 1293, 1200 |
| 4 | 4 | 4380, 2190, 1460, 1095, 876 |

Table 5.1: Five classes

| Simulation | Criteria | Number of particles |
|------------|----------|--|
| 5 | 1 | 1000, 1000, 1000, 1000, 1000, 1000, 1000, 1000, 1000, 1000 |
| 6 | 2 | 1608, 1276, 1115, 1013, 940, 885, 840, 804, 773, 746 |
| 7 | 3 | 2426, 1528, 1166, 963, 830, 735, 663, 606, 560, 523 |
| 8 | 4 | 3414, 1707, 1138, 854, 683, 569, 488, 427, 379, 341 |

Table 5.2: Ten classes

| Simulation | Criteria | Number of particles |
|------------|----------|--|
| 9 | 1 | 667, 667, 667, 667, 667, 667, 667, 667, 667, 667, 667, 667, 667, 667, 667 |
| 10 | 2 | 1197, 950, 830, 754, 700, 659, 626, 599, 576, 556, 538, 523, 509, 497, 480 |
| 11 | 3 | 1987, 1252, 955, 789, 679, 602, 543, 497, 459, 428, 402, 379, 359, 342, 327 |
| 12 | 4 | 3014, 1507, 1004, 754, 603, 502, 430, 377, 335, 301, 274, 251, 232, 215, 201 |

Table 5.3: Fifteen classes

The Tables 5.1-5.3 show initial particle number for different sets of simulations. Table 5.1 gives the number of particles in each class, having $I = 5$ classes, satisfying the criterias 1, 2, 3 and 4 with $N_0 = 10000$. Table 5.2 gives the number of particles in each class, having $I = 10$ classes, satisfying the criterias 1, 2, 3 and 4 with $N_0 = 10000$. Table 5.3 gives the number of particles in each class, having $I = 15$ classes, satisfying the criterias 1, 2, 3 and 4 with $N_0 = 10000$.

Corresponding to the above tables, we plotted the figures for the number of particles versus classes. The bar diagram Figure 5.2 represents the number of particles in each of the five classes satisfying the criteria 1-4 corresponding to the Table 5.1. The bar diagram Figure 5.3 represents

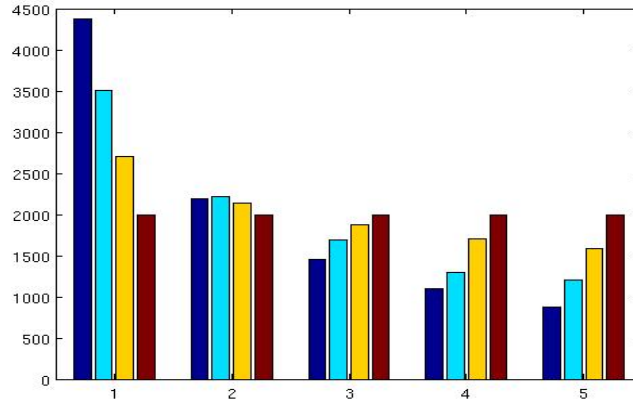


Figure 5.2: Initial condition for the simulations

the number of particles in each of ten classes satisfying the criteria 1-4 corresponding to the Table 5.2. The bar diagram Figure 5.4 represents the number of particles in each of fifteen classes satisfying the criteria 1-4 corresponding to the Table 5.3.

In a similar manner we obtained the number of particles in each class satisfying the criterias 1-4 with $N_0 = 5000$ and $N_0 = 15000$ for three classes $I = 5, 10, 15$. The values and the figures corresponding to these criteria are given in Appendix B.

5.2 Evaluation of the bed parameter

We calculate the collision rate function using the formula (4.2), which is derived in Chapter 4, Section 2. From the physical description of flow inside the fluidized bed as shown in Chapter 4, Section 4, we expect a shear kernel. Therefore we try to fit the simulated data of the collisions to the shear kernel by using a least squares fit. We introduced a new fitting parameter η . We call it the bed parameter.

Define the predicted collision frequency as a set of collisions represented by $K(v_i, v_j)$ and the observed collisions of the fluidized bed simulations as the set of $K'(v_i, v_j)$, then by the least square method

$$S = \sum_i \sum_j (K'(v_i, v_j) - \eta K(v_i, v_j))^2 \quad (5.5)$$

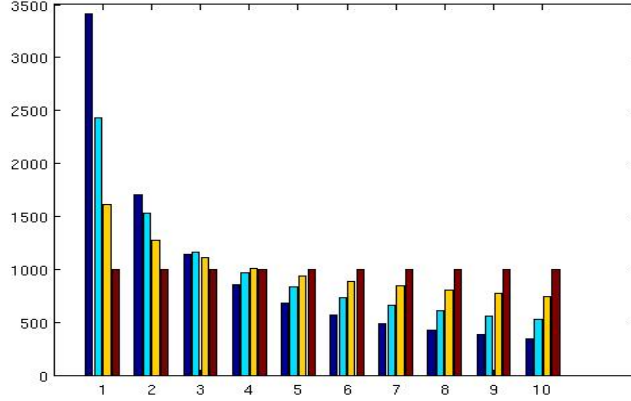


Figure 5.3: Initial condition for the simulations

where η is bed parameter to be evaluated and $K'(v_i, v_j) = \frac{N_{ij} V_{bed}}{n_i n_j t_{step}}$

$$\begin{aligned}
 S &= \sum_{i,j} \left(\frac{N_{ij} V_{bed}}{n_i n_j t_{step}} - \eta K(v_i, v_j) \right)^2 \\
 \frac{\partial S}{\partial \eta} &= 0 \Rightarrow -2 \sum_{i,j} \left(\frac{N_{ij} V_{bed}}{n_i n_j t_{sim}} - \eta K(v_i, v_j) \right) K(v_i, v_j) = 0 \\
 \Rightarrow \eta &= \frac{\sum_{i,j} \frac{N_{ij} V_{bed}}{n_i n_j t_{step}} K(v_i, v_j)}{\sum_{i,j} K^2(v_i, v_j)}. \tag{5.6}
 \end{aligned}$$

Here $K(v_i, v_j)$ is the shear kernel given in Chapter 2. The bed parameter η is obtained for various initial particle size distributions and for different classes of particles. The bed parameter for different simulation conditions are given in the next section.

Relative error

The relative error is calculated as

$$R.E. = \frac{\|X^{exact} - X^{sim}\|}{\|X^{exact}\|}, \tag{5.7}$$

where $\|\cdot\|$ is the L_2 norm. The L_2 norm of a vector $X = (x_1, x_2, \dots, x_n)$ is given as $(\sum_{k=0}^n x_k^2)^{1/2}$. The values $\|X^{exact}\|$ and $\|X^{sim}\|$ are the exact and simulated values of the shear kernel (4.4).

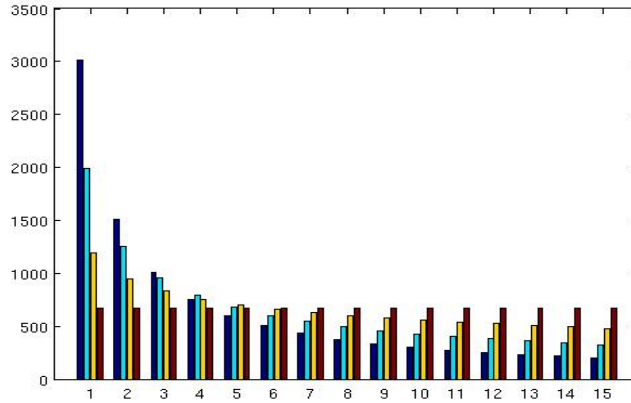


Figure 5.4: Initial condition for the simulations

5.3 Simulation results for a pseudo 3D bed

We consider the pseudo-3D bed for these simulations. Since gas phase hydrodynamics are resolved in two dimensions and the particle movements are three dimensional, we can call it a pseudo-3D bed. This can be justified since the simulated system is a flat fluidised bed with a depth of 1cm where the motion of the gas phase in the third dimension can be neglected, if we disregard the boundary layer.

All the physical parameters like bed dimension, fluidization velocity, etc. are fixed and are the same for all the pseudo 3D fluidized bed simulations. So the only changing parameter is particle number N_0 and the number of classes I . The parameters of the simulation are shown in the Appendix B. We observe the collision rate function among different classes using the DPM at different time intervals.

The Figures 5.5 shows the snapshots of the DPM simulations with bubbles. The colour of the particles shows the position of the particles with respect to their depth from the front view of the fluidized bed. The simulation data are considered after $t = 5$ sec in order to get the spatially homogeneous fluidized bed. We run the simulation for $t = 15$ sec. We consider three different sets of particle classes based on their volume, like particles with 5 classes, 10 classes and 15 classes. In each simulation we collected the collisions among different classes of particles at different time intervals.

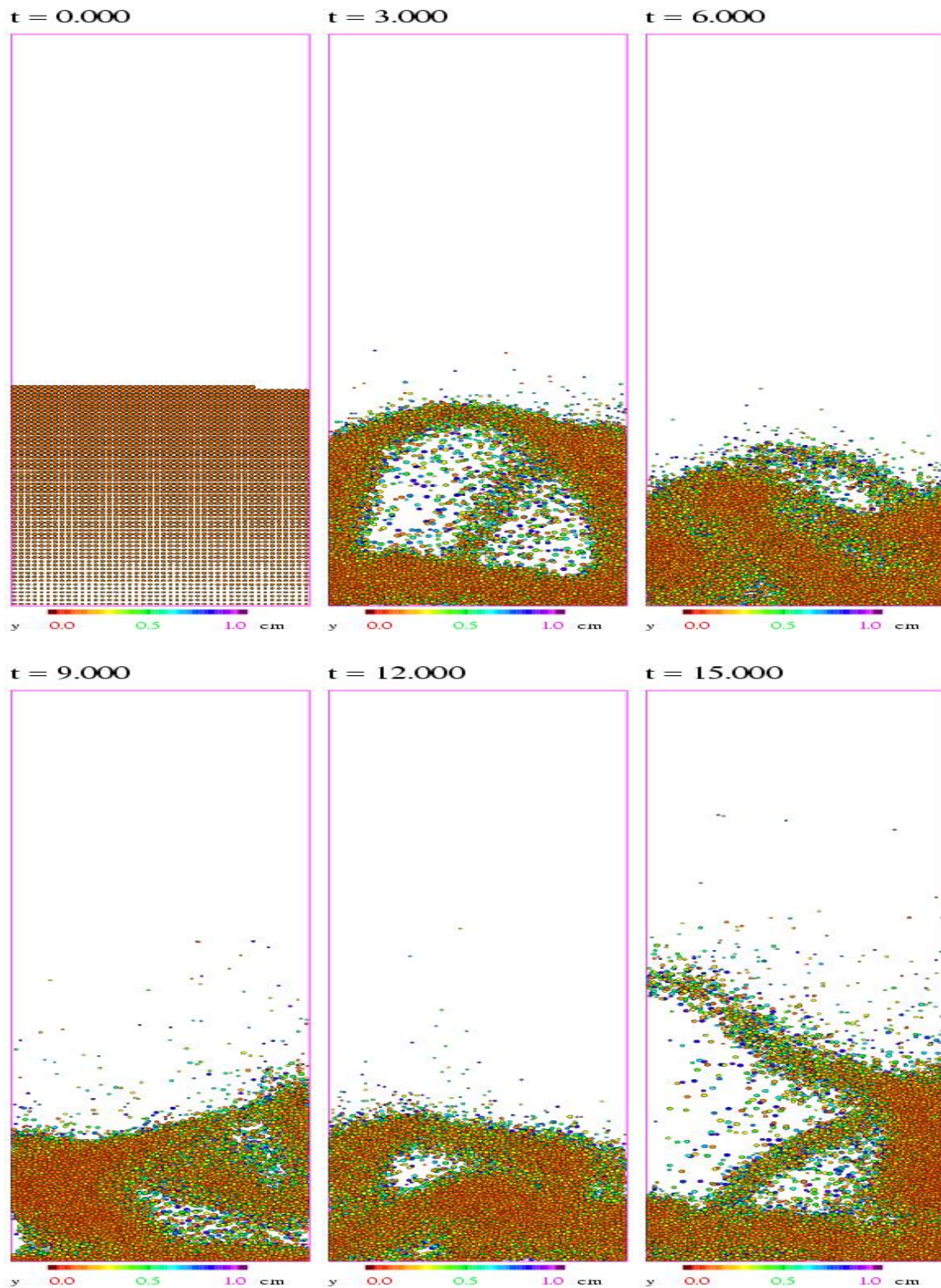


Figure 5.5: Snapshots of fluidized bed simulations at various time intervals $t = 0, 3, 6, 9, 12, 15$ sec for a pseudo 3-Dimensional fluidized bed

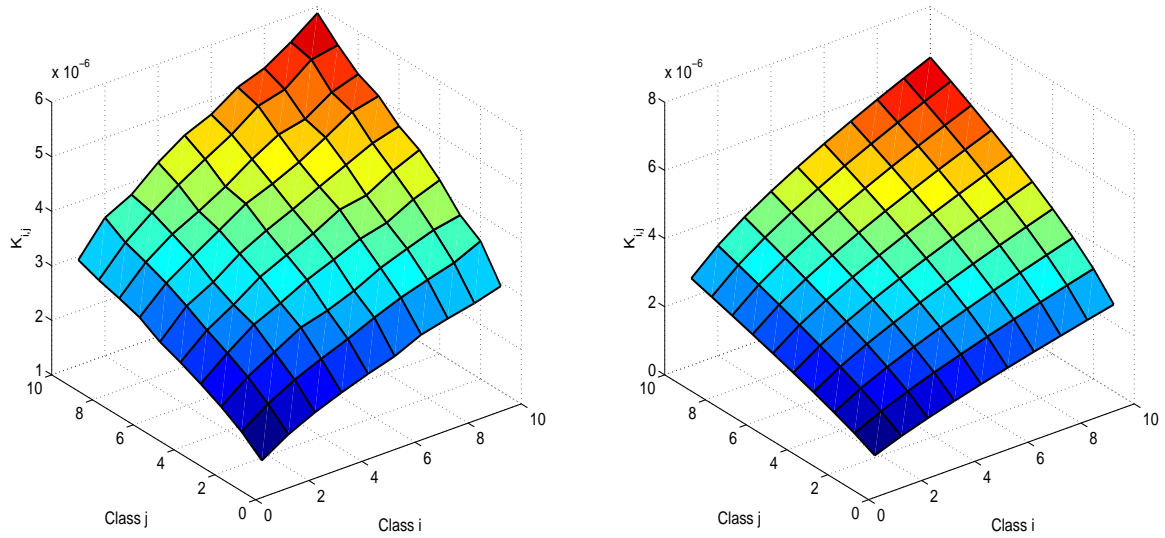


Figure 5.6: Simulated and Fitted collision frequency functions during the time interval 5 to 10 seconds of DPM simulation

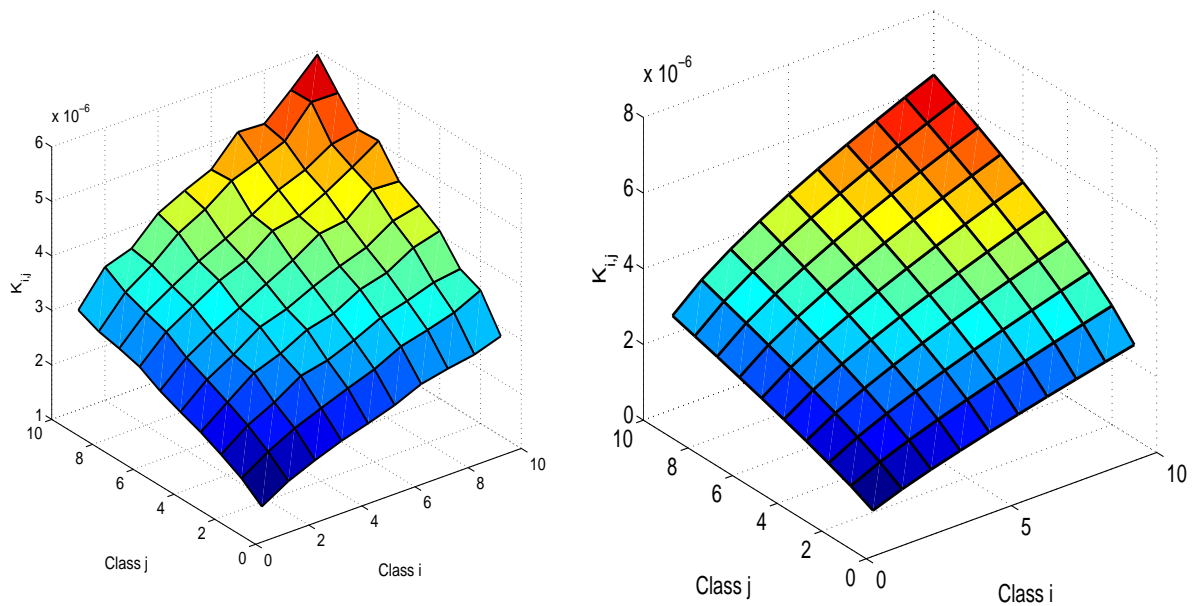


Figure 5.7: Simulated and Fitted collision frequency functions during the time interval 5 to 15 seconds of DPM simulation

The Figures 5.6, 5.7 represent the collisions among the ten classes of the particles of volume $V_0, 2V_0, 3V_0, \dots, 10V_0$. The top Figures 5.6 represents the collisions among the particles during the time interval $t = [5.0 \ 10.0]$ sec and the bottom Figures 5.7 are for the time interval $t = [5.0 \ 15.0]$ sec with an initial particle number satisfying first moment for 10000 particles in a pseudo 3D fluidized bed. The Figures in the left side are the simulated values and the right side are the figures with the fitting parameter. In all these Figures 5.6, 5.7, we can observe that large-large particle size collisions are more favourable. This shows that the shape of the surface is near to the shear kernel surface.

Table 5.4: Simulation results for different particle size distributions for 5000 particles

| Class | Character | Bed parameter η | Particle volume | Relative error |
|-------|---------------|----------------------|-----------------|----------------|
| 5 | Zeroth moment | 96.94 | 7.86E-6 | 0.2532 |
| 10 | Zeroth moment | 113.111 | 1.44E-5 | 0.1211 |
| 15 | Zeroth moment | 118.80 | 2.1E-5 | 0.1149 |
| 5 | Equal length | 100.87 | 7.15E-6 | 0.5810 |
| 10 | Equal length | 116.549 | 1.27E-5 | 0.1025 |
| 15 | Equal length | 124.71 | 1.49E-5 | 0.1217 |
| 5 | Equal area | 125.00 | 6.43E-6 | 0.6480 |
| 10 | Equal area | 137.294 | 1.07E-5 | 0.2072 |
| 15 | Equal area | 142.42 | 1.49E-5 | 0.1119 |
| 5 | First moment | 140.76 | 5.73E-6 | 0.7203 |
| 10 | First moment | 149.787 | 8.94E-6 | 0.1142 |
| 15 | First moment | 162.55 | 1.18E-5 | 0.2385 |

We calculated the kernel $K(x, y)$ from the simulation data using the formula (4.2) derived in Chapter 4 Sections 2. We evaluated the bed parameter η for each simulation using the Equation (5.6). The Table 5.4 gives the bed parameter η for $N_0 = 5000$ particles. We run the simulations for $t = 15$ seconds for the initial particle size distribution satisfying the four criteria for three different classes.

The value of the bed parameter, relative error of fitting, etc. can be seen in the Table 5.4. From the Table 5.4 we can observe that the value of the bed parameter increases with increase in the total particle volume. That means the number of collisions increases with increase of the particle volume. Here for all the simulations the dimensions of the fluidized bed were kept constant.

Figure 5.8 describes behaviour of the bed parameter with respect to the number of classes. Each line in the figure represents the bed parameter value corresponds to the character satisfied by the initial PSD for different particle classes. We can observe that the lines are parallel and are monotonically increasing with increase in number of classes.

The value of the bed parameter, relative error of fitting, etc. can be seen in the Tables 5.5, 5.6 for $N_0 = 10000$ and $N_0 = 15000$ respectively. From Tables 5.5, 5.6 we can observe that the

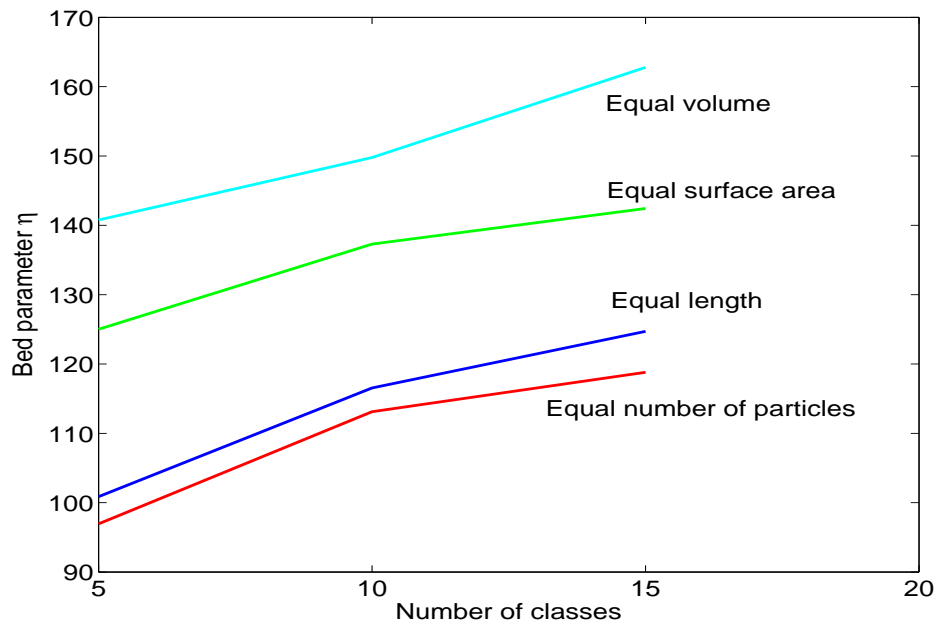


Figure 5.8: Bed parameter corresponding to various number of classes for 5000 particles

Table 5.5: Simulation results for different particle size distributions for 10000 particles

| Class | Character | Bed parameter η | Particle volume | Relative error |
|-------|---------------|----------------------|-----------------|----------------|
| 5 | Zeroth moment | 118.13 | 1.57E-5 | 0.1021 |
| 10 | Zeroth moment | 155.054 | 2.88E-5 | 0.1078 |
| 15 | Zeroth moment | 171.6367 | 4.19E-5 | 0.0936 |
| 5 | Equal length | 128.3580 | 1.43E-5 | 0.1057 |
| 10 | Equal length | 165.5839 | 2.53E-5 | 0.1074 |
| 15 | Equal length | 192.5386 | 3.62E-5 | 0.1021 |
| 5 | Equal area | 138.0706 | 1.28E-5 | 0.0859 |
| 10 | Equal area | 181.5455 | 2.15E-5 | 0.0904 |
| 15 | Equal area | 219.1333 | 2.98E-5 | 0.1118 |
| 5 | First moment | 151.6243 | 1.14E-5 | 0.0721 |
| 10 | First moment | 207.2792 | 1.78E-5 | 0.0966 |
| 15 | First moment | 246.8127 | 2.37E-5 | 0.0942 |

Table 5.6: Simulation results for different particle size distributions of 15000 particles

| Class | Character | Bed parameter η | Particle volume | Relative error |
|-------|---------------|----------------------|-----------------|----------------|
| 5 | Zeroth moment | 188.6722 | 2.36E-5 | 0.1118 |
| 10 | Zeroth moment | 199.7154 | 4.32E-5 | 0.0965 |
| 15 | Zeroth moment | 225.3654 | 6.28E-5 | 0.0796 |
| 5 | Equal length | 199.8196 | 2.15E-5 | 0.0894 |
| 10 | Equal length | 256.2417 | 3.79E-5 | 0.0978 |
| 15 | Equal length | 284.7975 | 5.42E-5 | 0.0967 |
| 5 | Equal area | 222.9835 | 1.93E-5 | 0.0817 |
| 10 | Equal area | 281.4234 | 3.23E-5 | 0.1053 |
| 15 | Equal area | 325.0151 | 4.48E-5 | 0.1061 |
| 5 | First moment | 235.3659 | 1.72E-5 | 0.0565 |
| 10 | First moment | 303.3080 | 2.68E-5 | 0.1112 |
| 15 | First moment | 357.4970 | 3.55E-5 | 0.1204 |

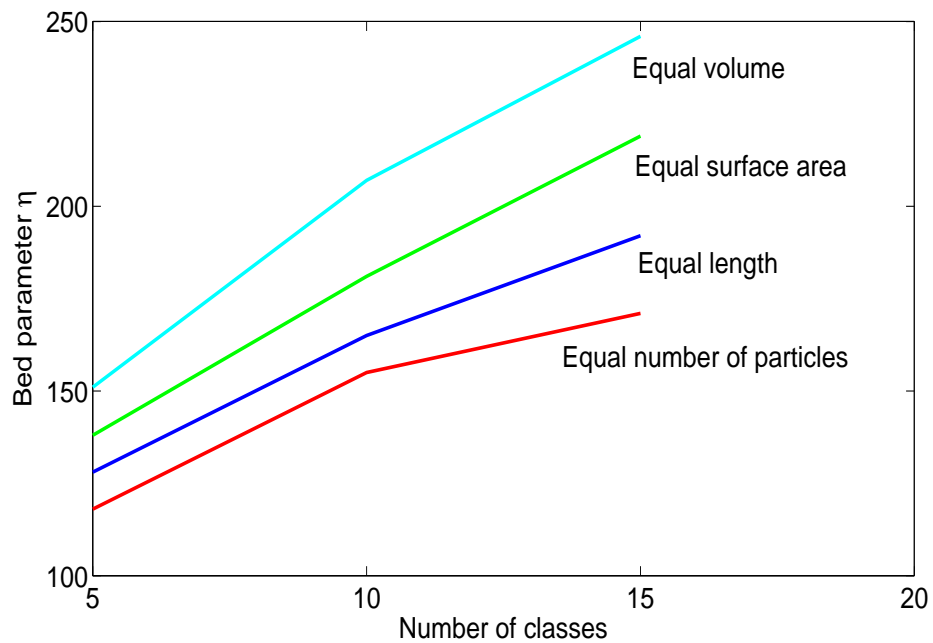


Figure 5.9: Bed parameter corresponding to various number of classes for 10000 particles

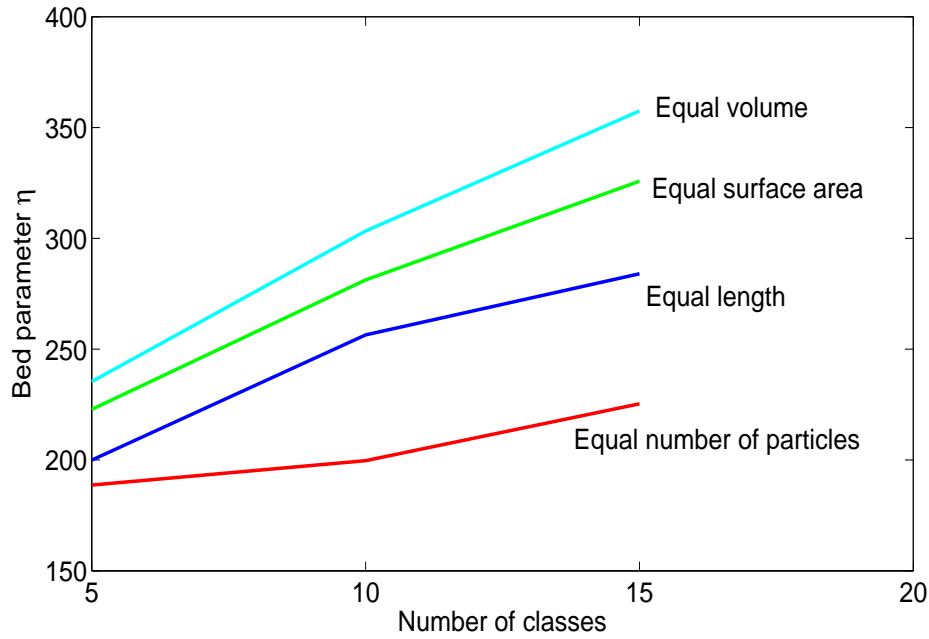


Figure 5.10: Bed parameter corresponding to various number of classes for 15000 particles

value of the bed parameter increases with increase in the total particle volume. That means the number of collisions increases with increase of the particle volume. Here for all the simulations the dimensions of the fluidized bed were kept constant.

The value of the bed parameter for 5, 10 and 15 classes is plotted in Figures 5.9, 5.10. The same kind of behaviour is observed as seen for $N_0 = 5000$.

We consider the another specific case of simulation to observe the particle collisions. In this case we consider the same initial particle size distribution for all cases, but we increases the particle diameter so that the total particle volume increases. This kind of specific consideration was

| Class | Simulation | Time | Parameter η | Volume of particles | Relative Error |
|-------|------------|----------|------------------|---------------------|----------------|
| 5 | 1 | 5-15 sec | 115.5 | 1.147e-5 | 0.0751 |
| 5 | 2 | 5-15 sec | 155.74 | 1.982e-5 | 0.0864 |
| 5 | 3 | 5-15 sec | 176.19 | 3.147e-5 | 0.0921 |
| 5 | 4 | 5-15 sec | 270.20 | 4.698e-5 | 0.0811 |
| 5 | 5 | 5-15 sec | 339.15 | 6.689e-5 | 0.0833 |
| 5 | 6 | 5-15 sec | 380.57 | 9.176e-5 | 0.0512 |

Table 5.7: Simulation result for increasing volume of the particles

explained in case 7 above. The value of the bed parameter, relative error of fitting, etc. can be seen in the Table 5.7. From Table 5.7 we can observe that the value of the bed parameter increases with increase in the total particle volume. That means the number of collisions increases with increase of the particle volume. Here for all the simulations the dimension of the fluidized bed was kept constant.

5.3.1 Log-Normal distribution

Frequently particle sizes are distributed using a log-normal distribution. We consider the initial particle size distribution as a discretized log-normal distribution with $\sigma = 0.001$ and minimum radius 0.00038 m for a pseudo 3-D fluidized bed. The particles are spread across 14 classes. The initial particle size distribution can be seen in Figure 5.11.

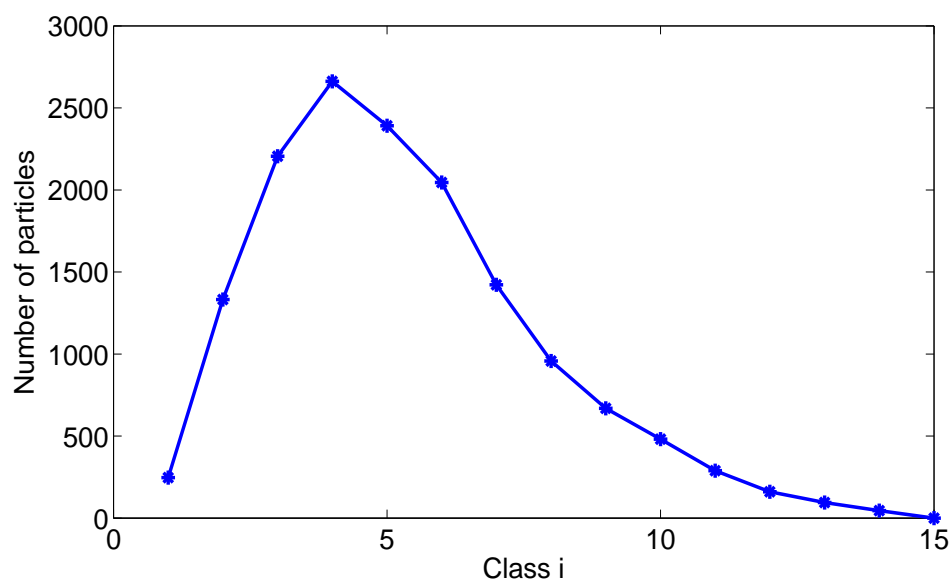


Figure 5.11: Initial particle size distribution

We collected the particle collisions among the fourteen size classes and the collision surface is plotted in the Figure 5.12. From the Figure 5.12 we can observe that the large number of collisions among big size class of particles and smaller number of collisions among small size class of particles. This shows that the collision surface is near to the shear kernel. So we try to fit the collision surface to the shear kernel and the bed parameter $\eta = 203.87$ and the relative error of fitting is 0.1021. The collision surface with the bed parameter η is given in the Figure 5.12.

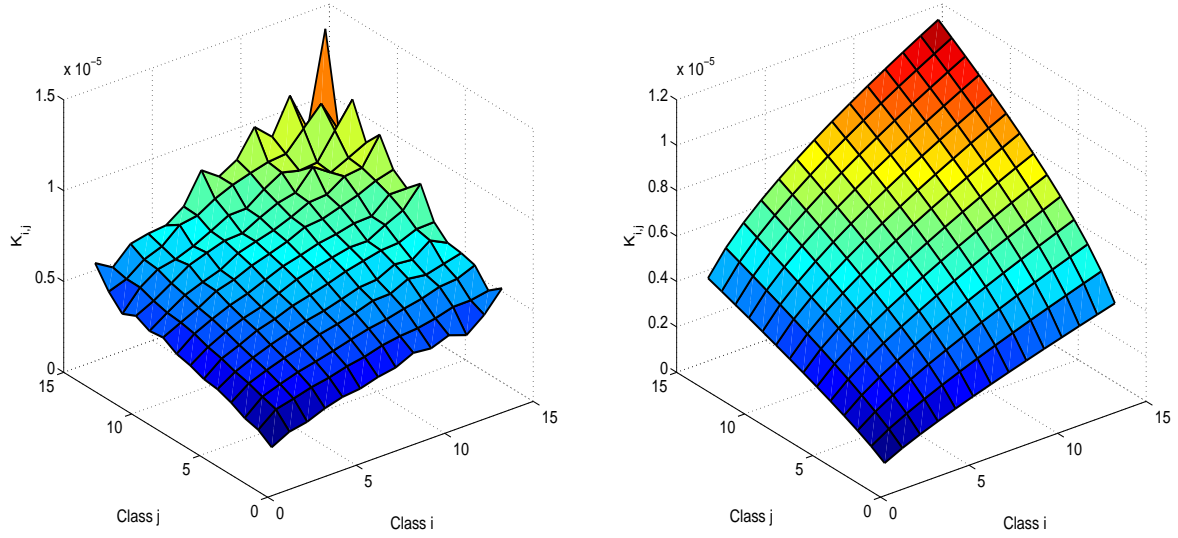


Figure 5.12: Collision surfaces for log-normal distribution of particles from the simulated and the corresponding fitted surfaces

5.4 Simulation results for 3D beds

We started the simulation with 15000 polydisperse spherical glass particles with smallest diameter of 1 mm in a 3D bed of dimension $10 \times 5 \times 60$ cm. The particle size classes are defined based on volume (i.e. $V_0, 2V_0, 3V_0, \dots$) with 5, 10 and 15 classes. Here the particles are distributed into various size classes based on certain criteria satisfied by each size class as given in the Section 5.1.2 cases 1-4. We used a hard sphere binary collision model for particle interactions and no aggregation process involved inside the bed.

For each particle size distribution we counted the collisions among different classes and plotted the collision surface. Figure 5.13 represents collisions among different class of particles during the time interval 5 to 15 seconds with particle size distribution satisfying the zeroth moment criteria i.e. equal number of particles in each size class i . We can observe that there are more collisions among particles of large size and a smaller number of collisions among the particles of smaller size which is also observed in case of shear kernel. So we try to fit the simulated result with the shear kernel and evaluated the bed parameter for each simulation. Figure 5.13 represents the collision surface with the bed parameter $\eta = 6.6569$.

The value of the bed parameter, relative error of fitting, etc. can be seen in the Table 5.8. From Table 5.8 we can observe that the value of the bed parameter increases with increase in the total particle volume. That means the number of collisions increases with increase of the particle volume. Here for all the simulations the dimensions of the fluidized bed kept constant.

Figure 5.14 describes behaviour of the bed parameter with respect to the number of classes. Each

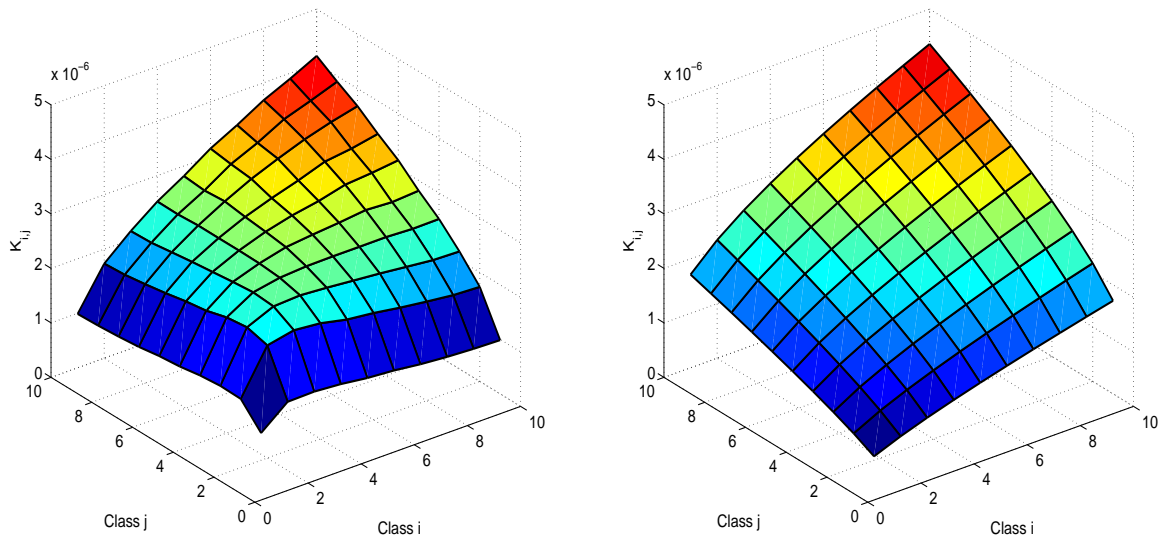


Figure 5.13: Collision surfaces for the zeroth moment criteria from the simulated (left) and the corresponding fitted surface (right) with bed parameter $\eta = 6.6569$

line in the Figure 5.14 represents the bed parameter value corresponds to the character satisfied by the initial PSD for different particle classes. We can observe that the lines are parallel and are monotonically increasing with increase in number of classes, due to the restricted size of the simulation domain there is a limit to the number of particles that may be taken. Otherwise they cannot move and just stick together. This kind of same behaviour is also observed in case of pseudo 3D fluidized bed simulations.

Remark 5.1 *From the above simulation results one can observe the difference in the bed parameter η for pseudo 3D and 3D fluidized bed simulations. This is due to difference in the number of collisions. We have a higher number of collisions in a pseudo 3D fluidized bed compared to a 3D fluidized bed.*

Table 5.8: Simulation results for different particle size distributions for 15000 particles

| Class | Character | Bed parameter η | Particle volume | Relative error |
|-------|---------------|----------------------|-----------------|----------------|
| 5 | Zeroth moment | 5.8205 | 3.68E-4 | 0.5366 |
| 10 | Zeroth moment | 6.6569 | 6.75E-4 | 0.1433 |
| 15 | Zeroth moment | 6.8240 | 9.82E-4 | 0.1253 |
| 5 | Equal length | 6.9836 | 3.33E-4 | 0.5333 |
| 10 | Equal length | 7.4238 | 5.93E-4 | 0.1560 |
| 15 | Equal length | 8.1200 | 8.47E-4 | 0.1217 |
| 5 | Equal area | 7.6093 | 3.02E-4 | 0.6417 |
| 10 | Equal area | 7.7532 | 5.05E-4 | 0.2131 |
| 15 | Equal area | 8.6486 | 7.00E-4 | 0.1373 |
| 5 | First moment | 7.6816 | 2.68E-4 | 0.7002 |
| 10 | First moment | 8.9191 | 4.19E-4 | 0.3683 |
| 15 | First moment | 8.9645 | 5.55E-4 | 0.2181 |

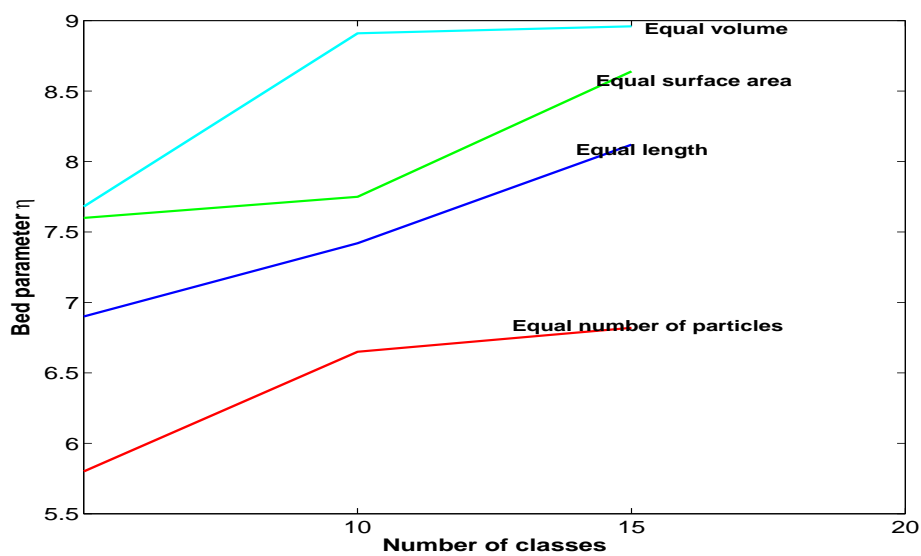


Figure 5.14: Bed parameter corresponding to various number of classes for 15000 particles

Chapter 6

Evaluation of aggregation efficiency rate

The present chapter contains the evaluation of the aggregation efficiency from the discrete particle model simulations with aggregation. We evaluated the aggregation efficiency rate for a random coalescence mechanism with the same initial conditions and parameters as used for the previous simulations. Out of all simulations, we selected two simulations of a pseudo 3D fluidized bed, two simulations from 3D fluidized bed and one with an initial particle size distribution having discrete normal distribution.

We calculated the particle size distribution by solving the aggregation equations with the newly calculated aggregation efficiency functions. A recently developed cell average technique is used to solve the aggregation equation. We end up this chapter with the computation of the particle size distributions from the macro model, population balance equations, for these new kernels.

6.1 Evaluation of the aggregation efficiency rate

In general, the aggregation kernel can be subdivided into two parts:

$$K(t, x, y) = K_0(t)K(x, y). \quad (6.1)$$

The collision frequency function $K(x, y)$ was evaluated in the Chapter 5 using discrete particle model simulations for various possible criteria. The aggregation rate function $K_0(t)$, determines the rate at which collisions result in successful aggregation of the particles. Usually it depends on the operating conditions, such as bed agitation, and material properties such as wettability and binder viscosity. We have the following assumptions in our simulations:

- The classes are based on volume based size class: $V_0, 2V_0, 3V_0, \dots$
- The particles are spherical.
- The particles aggregate randomly.
- Only binary aggregation is considered.

- A successful aggregation means that the two colliding particles appear in a larger volume class $V_i + V_j = V_{i+j}$.
- The granulation process is a batch process, so the total mass remains constant in time.
- The particle growth is due to aggregation process only. The effects of layering, breakage, etc. are neglected.

We made proper modifications to the Discrete Particle Model (DPM) code to incorporate the agglomeration process. When two particles aggregates, other particle has to be removed i.e., a ghost particle was created. As a result of this aggregation a ghost particle was created and its mass, volume and impulse are added to the new particle. The new particle is repositioned at the joint mass centre of the ghost particle and the original particle. This is described by formulae as

- mass conservation: $m' = m_1 + m_2$
- volume conservation: $V' = V_1 + V_2$
- momentum conservation: $\mathbf{v}' = \frac{m_1\mathbf{v}_1+m_2\mathbf{v}_2}{m_1+m_2}$
- repositioning of the particle: $\mathbf{x}' = \frac{m_1\mathbf{x}_1+m_2\mathbf{x}_2}{m_1+m_2}$

In these equations the subscripts 1 and 2 refer to the two aggregating particles and the prime refers to the newly formed particle.

The aggregation was done through the generation of a random number. We generate a random number z corresponding to each particle collision and it lies between 0 and 1. We dictate the particle aggregation or rebound based on the following criteria

```

if (z < 0.001)
if we have enough space for a new particle then aggregation
else
rebound

```

We calculated the number of successful aggregations per second. It is observed that the number of successful aggregations decreases with an increase of time. We fitted the obtained data $\hat{f}(t_i)$ corresponding to the time t_i with a two or three parameter polynomials $f(c_0, c_1t, \dots, c_nt^n)$ based on the nature of the aggregation. By using the least square method we evaluated the aggregation efficiency function $K_0(t)$ for the parameters c_0, c_1, \dots, c_n and is given by

$$I(c_0, c_1, \dots, c_n) = \min_{c_0, c_1, \dots, c_n} \sum_{i=0}^{t_{end}} \left[\hat{f}(t_i) - f(c_0, c_1t, \dots, c_nt^n) \right]^2. \quad (6.2)$$

The above process is incorporated into the DPM code by introducing new subroutines as shown in the dotted box 3B and 3C of the Figure 6.1. In the subroutine 3B we check for the availability

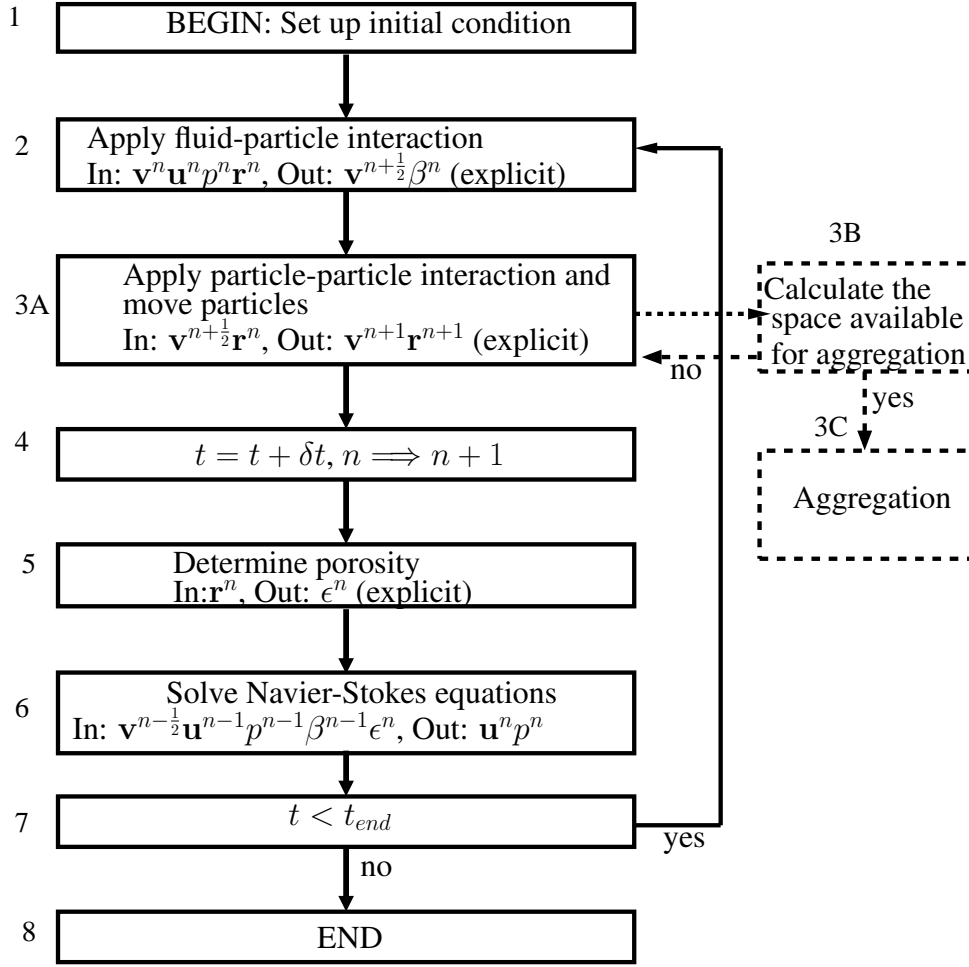


Figure 6.1: Flow diagram of the discrete particle model with aggregation

of enough space for the newly formed particle prior to the aggregation. If sufficient space is available for the new particle, then we move to the subroutine 3C. In this new subroutine 3C, we created the ghost particles and the new particles are formed according to the formulas given in items. We made proper changes in the other parts of the subroutines 2, 5 and 6 in order to avoid the interactions of the ghost particles with the gas phase and with the other particles.

Remark 6.1 *One should note that during this aggregation process, only the particle number will change and all other particle properties like mass, volume will remain constant.*

6.2 Simulation results for the aggregation efficiency rate

Out of all simulations, we selected five simulations with different initial particle size distributions. The simulations based on pseudo 3D fluidized bed, 3D fluidized bed and pseudo 3D

fluidized bed with discrete normal distribution as the initial particle size distribution.

6.2.1 Aggregation in pseudo 3D fluidized bed

Based on the assumptions of the previous Section 6.1, we consider the discrete particle model simulations with $N_0 = 15000$ with an initial particle size distribution of satisfying the zeroth moment criteria, i.e. equal number of particles in each size class for pseudo 3D fluidized bed. All the parameters are same as the previous Section 5.3 for pseudo 3D fluidized bed and are given in the Appendix A.

We started the aggregation process after 3 seconds of simulation in order to have a well mixed system and the simulation ran over a period of 30 seconds. We collected the number of successful aggregations in each step (1 second). We try to fit the obtained data with a two parameter polynomials based on the nature of the aggregation. By using the least square method we evaluated the aggregation efficiency function $K_0(t)$ and relative error of fitting for each function. The aggregation efficiency function $K_0(t)$ and its corresponding relative error of fitting are given in Table 6.1.

Table 6.1: Aggregation efficiency functions, case 1

| Aggregation efficiency $K_0(t)$ | Relative error |
|-----------------------------------|----------------|
| $443.8462 - 10.4335t$ | 0.0541 |
| $454.9983 - 12.7408t + 0.0824t^2$ | 0.0527 |
| $474.1814e^{-0.0361t}$ | 0.0551 |

From the above Table 6.1 we can observe that the relative error corresponding to the quadratic function is the smallest. Therefore suitable aggregation efficiency function for this simulation experiment is given by

$$K_0(t) = 454.9983 - 12.7408t + 0.0824t^2. \quad (6.3)$$

The Figure 6.2 shows the aggregation efficiency curve with initial particle size satisfying zeroth moment. The line in the dotted blue color shows the fitted one where as the red color curve corresponds to the simulated data. We found that the collision frequency function for these parameters is a shear kernel and the results for these cases are presented in Section 5.3. Therefore the complete agglomeration kernel is given as

$$K(t, x, y) = (454.9983 - 12.7408t + 0.0824t^2)(x^{\frac{1}{3}} + y^{\frac{1}{3}})^3. \quad (6.4)$$

We calculated the aggregation efficiency rate $K_0(t)$ with an initial particle size distribution satisfying the first moment criterion, i.e. equal total particle volume in each size class. We ran the

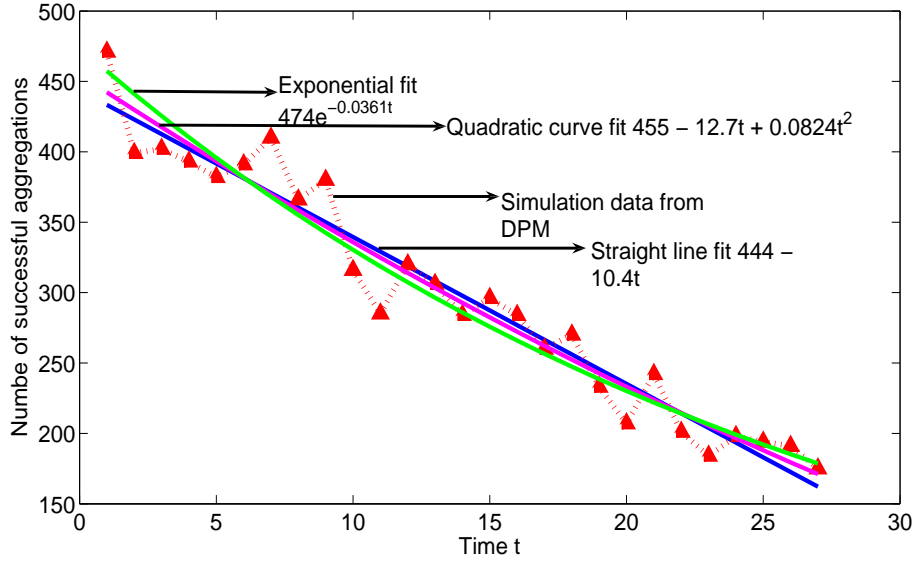


Figure 6.2: Aggregation efficiency $K_0(t)$ from simulated (red) and fitting functions

simulation for 30 seconds with the same parameters and assumptions of the previous simulation and collected the successful aggregations in each time step (1 second). By using the least square method we evaluated the aggregation efficiency function $K_0(t)$ and relative error of fitting for each function. The aggregation efficiency function $K_0(t)$ and its corresponding relative error of fitting are given in Table 6.2.

Table 6.2: Aggregation efficiency functions, case 2

| Aggregation efficiency $K_0(t)$ | Relative error |
|-----------------------------------|----------------|
| $489.8376 - 12.8297t$ | 0.0511 |
| $520.6427 - 19.2031t + 0.2276t^2$ | 0.0430 |
| $532.3746e^{-0.0425t}$ | 0.0423 |

From the above Table 6.2 we can observe that the relative error corresponding to the exponential function is smallest. Therefore a suitable aggregation efficiency function for this simulation experiment is given by

$$K_0(t) = 532.3746e^{-0.0425t}. \quad (6.5)$$

The Figure 6.3 shows the number of successful aggregations with an initial particle size satisfying equal first moment in each size class. The line in the dotted blue color shows the fitted one and the red color curve represents the simulated data. We found that the collision frequency function for these parameters is a shear kernel and the results for these cases are presented in Section 5.3.

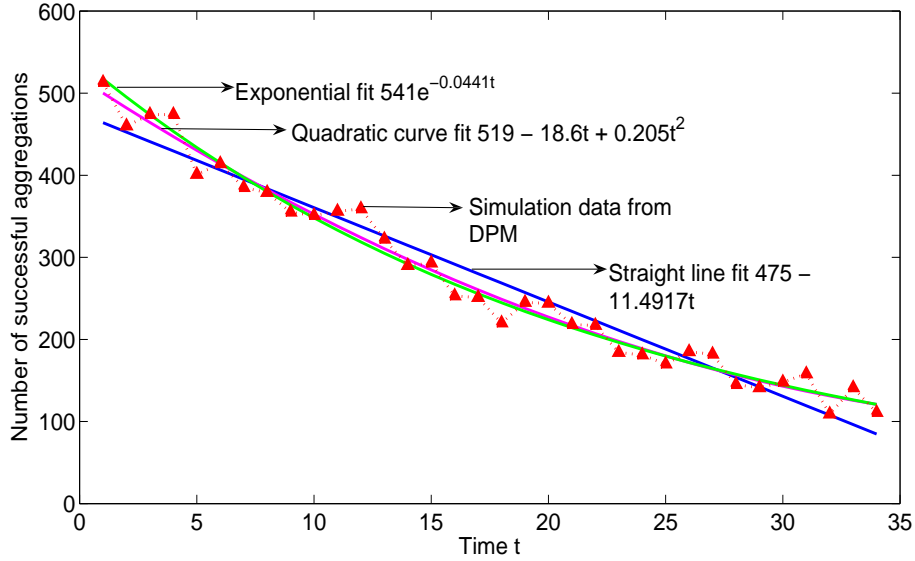


Figure 6.3: Aggregation efficiency $K_0(t)$ from simulated (red) and fitting functions

Therefore the complete agglomeration kernel is given as

$$K(t, x, y) = (532.3746e^{-0.0425t})(x^{\frac{1}{3}} + y^{\frac{1}{3}})^3. \quad (6.6)$$

6.2.2 Aggregation in 3D fluidized beds

In this section we are presenting the simulation results for a 3D fluidized bed. Based on the assumptions of the Section 6.1, we consider the discrete particle model simulations with $N_0 = 15000$ with an initial particle size distribution of satisfying the zeroth moment criteria, i.e. equal number of particles in each size class for 3D fluidized bed. All the parameters are same as the previous section 5.4 for 3D fluidized bed and are given in the Appendix B.

We started the aggregation process after 3 seconds of simulation in order to have a homogeneous system and the simulation ran over a period of 30 seconds. We collected the number of successful aggregations in each step (1 second). We try to fit the obtained data with a two or three parameter polynomials based on the nature of the aggregation. By using least square method we evaluated the aggregation efficiency function $K_0(t)$ and relative error of fitting for each function. The aggregation efficiency function $K_0(t)$ and its corresponding relative error of fitting are given in Table 6.3.

From the above Table 6.3 we can observe that the relative error corresponding to the exponential function is the smallest. Therefore suitable aggregation efficiency function for this simulation experiment is given by

$$K_0(t) = 377.7213e^{-0.0333t}. \quad (6.7)$$

Table 6.3: Aggregation efficiency functions

| Aggregation efficiency $K_0(t)$ | Relative error |
|-----------------------------------|----------------|
| $357.9373 - 8.0220t$ | 0.0550 |
| $374.4991 - 11.4486t + 0.1224t^2$ | 0.0528 |
| $377.7213e^{-0.0333t}$ | 0.0526 |

The Figure 6.4 shows the aggregation efficiency curve with initial particle size satisfying zeroth

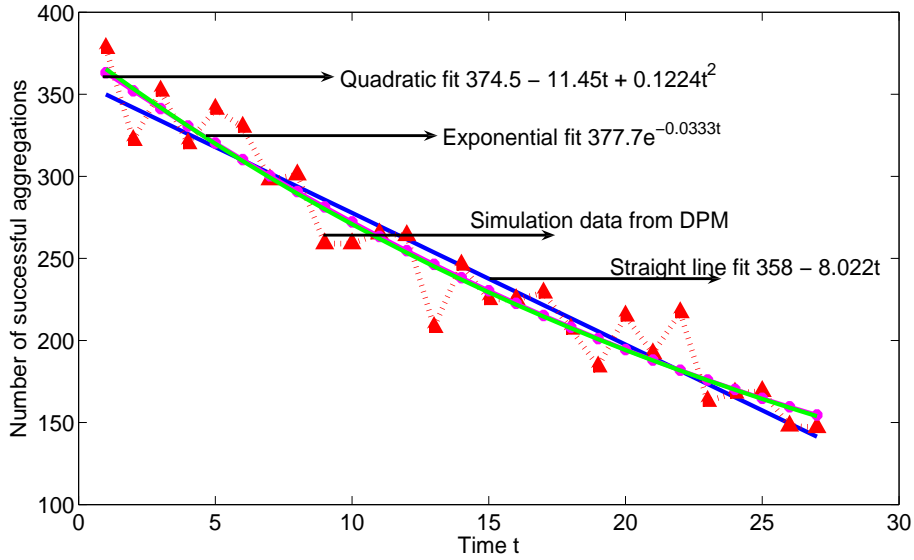


Figure 6.4: Aggregation efficiency $K_0(t)$ from simulated (red) and fitting functions

moment. The line in the dotted blue color shows the fitted one where as the red color curve corresponds to the simulated data. We found that the collision frequency function for these parameters is a shear kernel and the results for these cases are presented in Section 5.4. Therefore the complete agglomeration kernel is given as

$$K(t, x, y) = (377.7213e^{-0.0333t})(x^{\frac{1}{3}} + y^{\frac{1}{3}})^3. \quad (6.8)$$

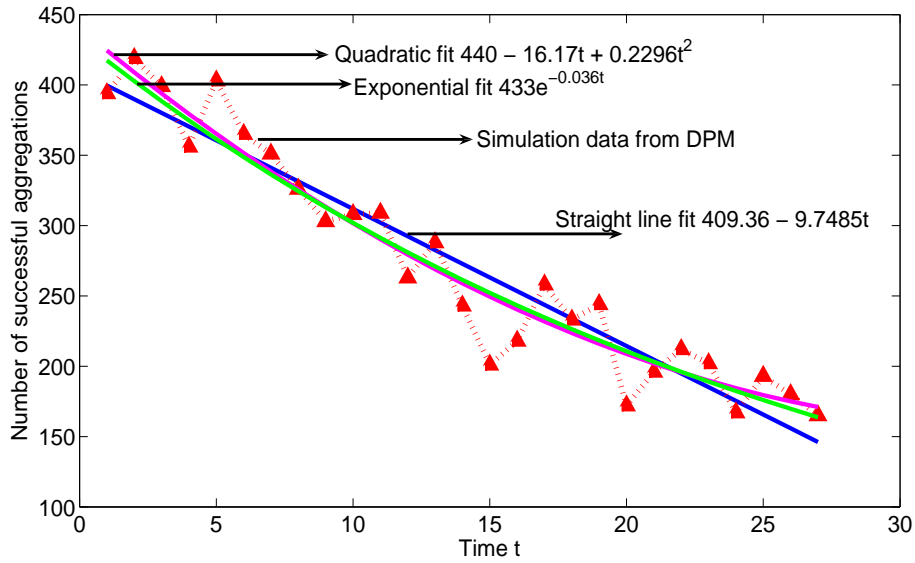
We calculated the aggregation efficiency rate $K_0(t)$ with an initial particle size distribution satisfying the first moment criteria, i.e. equal total particle volume in each size class. We ran the simulation for 22 seconds with the same parameters and assumptions of the previous simulation and collected the successful aggregations in each time step (1 second). By using the least square method we evaluated the aggregation efficiency function $K_0(t)$ and relative error of fitting for each function. The aggregation efficiency function $K_0(t)$ and its corresponding relative error of fitting are given in Table 6.4.

Table 6.4: Aggregation efficiency functions

| Aggregation efficiency $K_0(t)$ | Relative error |
|-----------------------------------|----------------|
| $409.3675 - 9.7485t$ | 0.0719 |
| $440.4410 - 16.1775t + 0.2296t^2$ | 0.0634 |
| $432.7832e^{-0.0360t}$ | 0.0653 |

From the above Table 6.4 we can observe that the relative error corresponding to the quadratic function less. Therefore suitable aggregation efficiency function for this simulation experiment is given by

$$K_0(t) = 440.4410 - 16.1775t + 0.2296t^2. \quad (6.9)$$

Figure 6.5: Aggregation efficiency $K_0(t)$ from simulated (red) and fitting functions

The Figure 6.5 shows the number of successful aggregations with an initial particle size satisfying first moment. The line in the dotted blue color shows the fitted one and the red color curve represents the simulated data. We found that the collision frequency function for these parameters is a shear kernel and the results for these cases are presented in Section 5.4. Therefore the complete agglomeration kernel is given as

$$K(t, x, y) = (440.4410 - 16.1775t + 0.2296t^2)(x^{\frac{1}{3}} + y^{\frac{1}{3}})^3. \quad (6.10)$$

6.2.3 Aggregation in pseudo 3D fluidized bed with log-normal distribution

In this section we consider a log-normal distribution as an initial particle size distribution. Based on the assumptions of the Section 6.1, we consider the discrete particle model simulations with $N_0 = 15000$ pseudo 3D fluidized bed. All the parameters are considered same as the Section 5.3.1 for pseudo 3D fluidized bed and are given in the Appendix A.

We started the aggregation process after 3 seconds of simulation in order to have a homogeneous system and the simulation run over a period of 30 seconds. We collected the number of successful aggregations in each step (1 second). We try to fit the obtained data with a multi parameter polynomials based on the nature of the aggregation. By using least square method we evaluated the aggregation efficiency function $K_0(t)$ and relative error of fitting for each function. The aggregation efficiency function $K_0(t)$ and its corresponding relative error of fitting are given in Table 6.5.

Table 6.5: Aggregation efficiency functions

| Aggregation efficiency $K_0(t)$ | Relative error |
|-----------------------------------|----------------|
| $414.9345 - 10.2705t$ | 0.0671 |
| $450.6718 - 17.6644t + 0.2641t^2$ | 0.0499 |
| $441.9886e^{-0.0382t}$ | 0.0523 |

From the above Table 6.5 we can observe that the relative error corresponding to the quadratic function to be the smallest. Therefore suitable aggregation efficiency function for this simulation experiment is given by

$$K_0(t) = 450.6718 - 17.6644t + 0.2641t^2 \quad (6.11)$$

The Figure 6.6 shows the aggregation efficiency curve with initial particle size having log-normal distribution. The line in the dotted blue color shows the fitted one where as the red color curve corresponds to the simulated data. We found that the collision frequency function for these parameters is a shear kernel and the results for this case are shown in Section 5.3.1. Therefore the complete agglomeration kernel is given as

$$K(t, x, y) = (450.6718 - 17.6644t + 0.2641t^2)(x^{\frac{1}{3}} + y^{\frac{1}{3}})^3. \quad (6.12)$$

6.3 Numerical methods for population balance equations

Analytical solutions for the population balance equations exists only for a few cases and for specific kernels. So most of the times one needs to solve these equations using numerical methods. We have a number of methods in the literature. Among these methods the fixed pivot method is

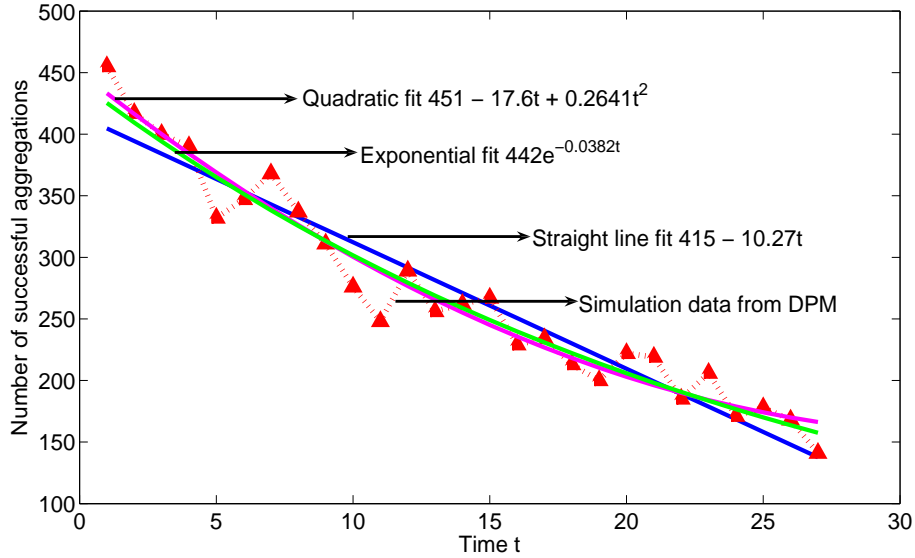


Figure 6.6: Aggregation efficiency $K_0(t)$ from simulated (red) and fitting functions

frequently used for the chemical engineering applications. Recently Kumar et al. (31) developed a new method known as the cell average technique, which gives better accuracy compared to fixed pivot technique. Here we are presenting some important steps in the formulation of the cell average technique to the aggregation equation.

Consider the binary aggregation equation of the form

$$\frac{\partial n(t, x)}{\partial t} = \frac{1}{2} \int_0^x K(t, x-y, y) n(t, x-y) n(t, y) dy - n(t, x) \int_0^\infty K(t, x, y) n(t, y) dy \quad (6.13)$$

where $t > 0$. The first term represents the birth of the particles of size x due to the aggregation of particles of sizes $x-y$ and y . The second term is called the death term. Here we shall refer to size as the particle volume.

The cell average technique is based on the averaging of particles volume within the cells. The discretisation of the equation (6.13) is based on the conditions of satisfying the first two moments. The net birth in i th cell is calculated using the volume average of all new born particles due to aggregation within three cells, $(i-1)$ th, i th and $(i+1)$ th. The particles should be assigned to the nearby representative sizes depending upon the position of the average value. If the volume average of $(i-1)$ th cell lies between x_{i-1} and $x_{i-1/2}$, then only a part of birth will appear in i th cell. The same arguments can be made for the i th and $(i+1)$ th cells. Similar to Kumar and Ramakrishna (32), the total birth in a cell is given by

$$B_{agg,i} = \frac{1}{2} \int_{x_{i-1/2}}^{x_{i+1/2}} \int_0^x K(t, x, x-y) n(t, x-y) n(t, y) dy dx. \quad (6.14)$$

Mathematically the number density function $n(t, x)$ can be approximated in terms of Dirac-delta distributions as

$$n(t, x) = \sum_{i=1}^I N_i \delta(x - x_i). \quad (6.15)$$

We first discretize the birth to compute the total birth rate in each cell and then redistribute the total birth to the neighboring nodes to get the consistency with moments. Since particles are assumed to be concentrated at representative sizes x_i , the number density $n(t, x)$ can be replaced by its Dirac-delta representation (6.15). Substituting the Dirac-delta representation of $n(t, x)$ in equation (6.14), for details of derivation see (30), we obtain

$$B_{agg,i} = \sum_{\substack{j \geq k \\ j,k \\ x_{i-1/2} \leq (x_j + x_k) < x_{i+1/2}}} \left(1 - \frac{1}{2} \delta_{j,k}\right) K_{j,k} N_j N_k. \quad (6.16)$$

Thus, B_i is the net rate of addition of particles to cell i by aggregation of particles in lower cells. The net flux of volume V_i into cell i as a result of these aggregations is therefore given by

$$V_{agg,i} = \sum_{\substack{j \geq k \\ j,k \\ x_{i-1/2} \leq (x_j + x_k) < x_{i+1/2}}} \left(1 - \frac{1}{2} \delta_{j,k}\right) K_{j,k} N_j N_k (x_j + x_k). \quad (6.17)$$

Consequently, the average volume of all newborn particles in the i th cell \bar{v}_i can be evaluated as

$$\bar{v}_{agg,i} = \frac{V_{agg,i}}{B_{agg,i}}. \quad (6.18)$$

Now we assume that the newborn particles B_i are assigned temporarily at \bar{v}_i . These particles have to be divided depending upon the value of \bar{v}_i to neighboring nodes in such a way that the formulation is consistent with the total number and mass. The birth according to the cell average technique is given as

$$B_{agg,i}^{CA} = B_{agg,i-1} \lambda_i^-(\bar{v}_{i-1}) H(\bar{v}_{i-1} - x_{i-1}) + B_{agg,i} \lambda_i^-(\bar{v}_i) H(x_i - \bar{v}_i) \\ + B_{agg,i} \lambda_i^+(\bar{v}_i) H(\bar{v}_i - x_i) + B_{agg,i+1} \lambda_i^+(\bar{v}_{i+1}) H(x_{i+1} - \bar{v}_{i+1}). \quad (6.19)$$

The function λ is defined as

$$\lambda_i^\pm(\bar{v}) = \frac{\bar{v} - \bar{v}_{i\pm 1}}{\bar{v}_i - \bar{v}_{i\pm 1}}.$$

The *Heaviside step function* is a discontinuous function also known as *unit step function* and is defined as

$$H(x) = \begin{cases} 1, & x > 0 \\ \frac{1}{2}, & x = 0 \\ 0, & x < 0. \end{cases} \quad (6.20)$$

The death term is the same as it was in Kumar and Ramakrishna (32) and is given as

$$D_{agg,i} = N_i \sum_{k=1}^I K_{i,k} N_k. \quad (6.21)$$

The final set of discrete equations can be written as

$$\begin{aligned} \frac{dN_i(t)}{dt} = & B_{agg,i-1} \lambda_i^-(\bar{v}_{i-1}) H(\bar{v}_{i-1} - x_{i-1}) + B_{agg,i} \lambda_i^-(\bar{v}_i) H(x_i - \bar{v}_i) \\ & + B_{agg,i} \lambda_i^+(\bar{v}_i) H(\bar{v}_i - x_i) + B_{agg,i+1} \lambda_i^+(\bar{v}_{i+1}) H(x_{i+1} - \bar{v}_{i+1}) \\ & - N_i \sum_{k=1}^I K_{i,k} N_k. \end{aligned} \quad (6.22)$$

The set of ordinary differential equations (6.22) resulting from the discretized technique is solved using a Runge-Kutta fourth and fifth order method with adaptive step-size control based on the embedded Runge-Kutta formulas.

Higher order schemes are also developed by Sandu (45) based on Newton-Cotes quadrature approach. He employed a semi-implicit Gauss-Seidel time integration method to the aggregation equation. This method gives fourth order accuracy. For the present comparison we use our inhouse code of cell average technique, whose accuracy is enough for our present application.

6.4 Computation of the particle size distributions

In this section we calculated the particle size distribution by solving the aggregation equations with the newly calculated shear kernels obtained from the previous sections. A recently developed cell average technique is used to solve the aggregation equation and is explained in the Section 6.3. We computed the particle size distributions for the new kernels obtained from the micro model. The results of the new particle size distributions are presented in Section 6.4 for different possible cases.

6.4.1 Computation of the particle size distribution for pseudo 3D fluidized bed

We considered two specific cases for the computation of the macro aggregation model. In the first case we considered the initial particle size distribution satisfying zeroth moment criteria, i.e. equal number of particles in each size class. For both the aggregation equation and discrete particle simulations we have taken the same initial condition and can be seen in the Figure 6.7 as blue line.

The final particle size distribution at the end of 30 seconds is plotted in the Figure 6.7 as the red line. For this specific simulation we calculated the aggregation kernel (6.3) using least square

fit in the Section 6.2. We substituted the kernel (6.3) into the aggregation and then we solved it using cell average technique developed by Kumar (30). We calculated the number of particles in each class from the aggregation equation and the result can be seen in the Figure 6.7. In a similar

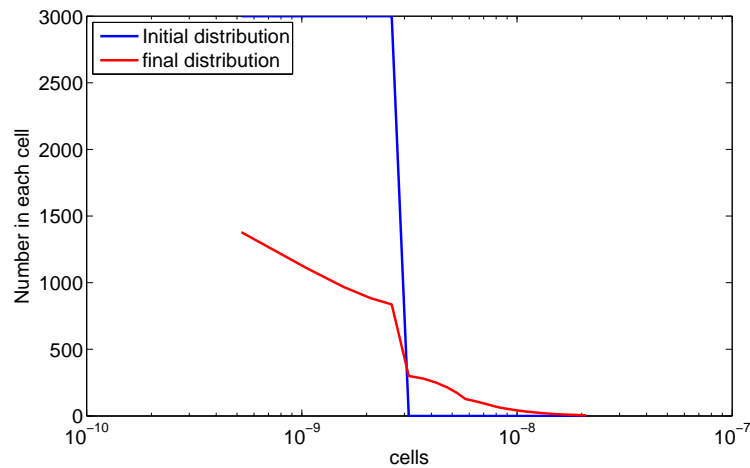


Figure 6.7: Aggregation starting with equal number (zero moment) criterion for pseudo 3D bed

manner we calculated the particle size distribution for the aggregation equation with the initial particle size distribution satisfying first moment criteria. The aggregation kernel calculated from the discrete particle model simulations was given in (6.4).

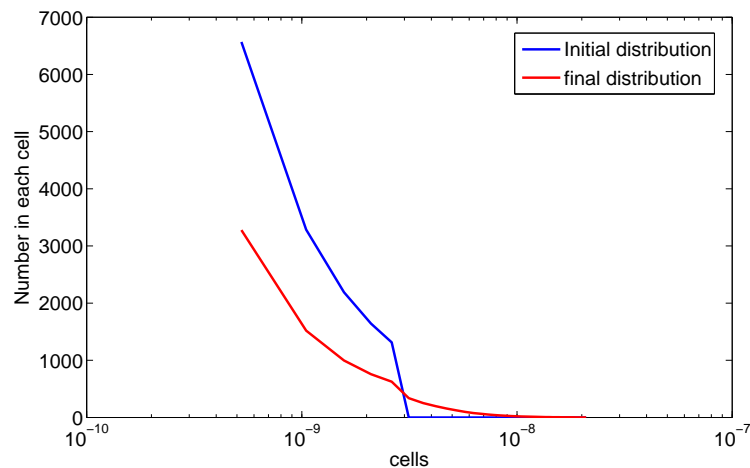


Figure 6.8: Aggregation starting with equal volume (first moment) criterion for pseudo 3D bed

6.4.2 Computation of the particle size distribution for 3D fluidized bed

We considered two specific cases for the computation of the particle size distribution using the aggregation equation. In the first case we considered the initial particle size distribution satisfying zeroth moment criteria, i.e. equal number of particles in each size class. For both the aggregation equation and discrete particle simulations we have taken the same initial condition and can be seen in the Figure 6.9 as blue line.

The final particle size distribution at the end of 30 seconds is plotted in the Figure 6.9 as the red line. For this specific simulation we calculated the aggregation kernel (6.5) using least square fit in the Section 6.2. We substituted the kernel (6.5) into the aggregation and then we solved it using cell average technique developed by Kumar (30). We calculated the number of particles in each class from the aggregation equation and the result can be seen in the Figure 6.9.

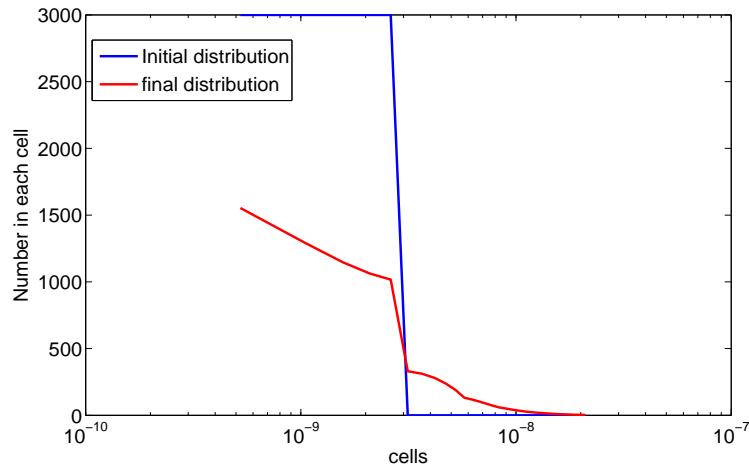


Figure 6.9: Aggregation starting with equal number (zero moment) criterion for 3D bed

In a similar manner we calculated the particle size distribution for the aggregation equation with the initial particle size distribution satisfying first moment criteria. We considered the same initial condition for the simulations in the discrete particle model. The aggregation kernel calculated from the discrete particle model simulations was given in (6.6).

6.4.3 Computation of the particle size distribution for 3D fluidized bed with log normal distribution

We considered a specific case for the computation of the particle size distribution from the aggregation equation. In this case we considered the initial condition having a log normal particle size distribution. For both the aggregation equation and discrete particle simulations we have

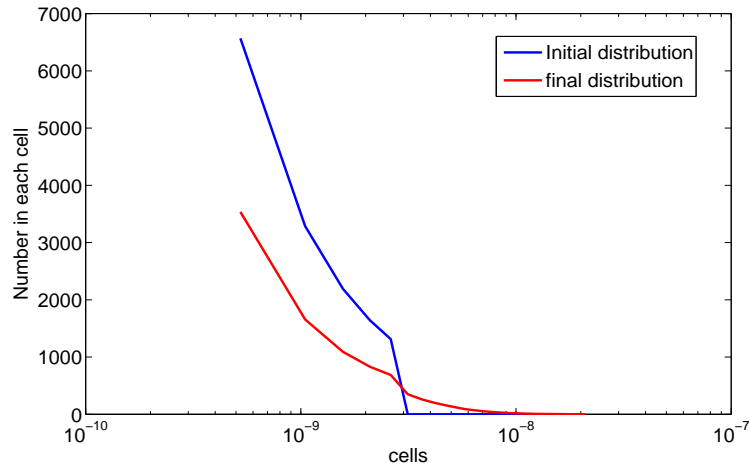


Figure 6.10: Aggregation starting with equal volume (first moment) criterion for 3D bed

taken the same initial condition and can be seen in the Figure 6.11 as blue line.

The final particle size distribution at the end of 30 seconds is plotted in the Figure 6.11 as the red line. For this specific simulation we calculated the aggregation kernel (6.7) using least square fit in the Section 6.2. We substituted the kernel (6.7) into the aggregation and then we solved it using cell average technique developed by Kumar (30). We calculated the number of particles in each class from the aggregation equation and the result can be seen in the Figure 6.11.

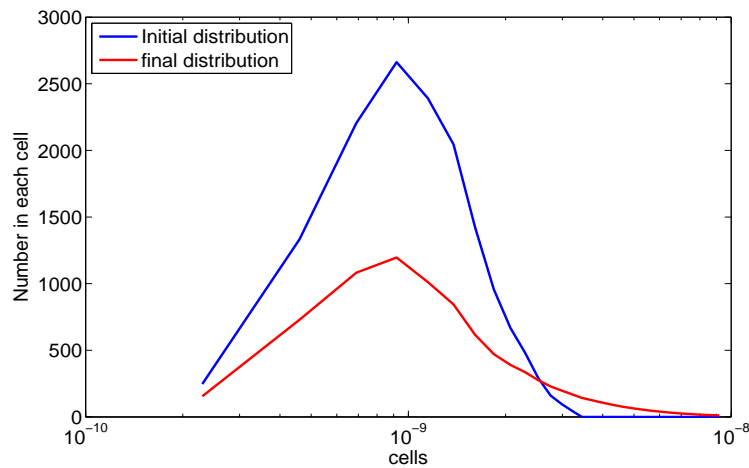


Figure 6.11: Aggregation starting with log normal particle size distribution

Chapter 7

General conclusions and outlook

The main aim of the present thesis is to have a complete idea of micro-macro transitions of granulation processes in the fluidized beds. We have different processes inside the fluidized beds like aggregation, growth, nucleation, breakage, etc. To understand these processes in a macroscopic level population balance equations are widely used in the literature. The present work involves the simulations for modelling the aggregation kernels of the Smoluchowski (49) equation. This equation describes the coagulation of particles, when they come in contact with one another, on a macroscopic scale. As a result of this aggregation process the particle size distribution will change in a given system due to various physical influences. The most important quantity in this modeling is the aggregation kernel. In general, this aggregation kernel is a function of time and particle diameter, volume, mass, etc and the physical and chemical processes influencing the aggregation. An elaborative discussion of the aggregation equation and various kernels were presented in Chapter 2.

To model the aggregation kernels we used a micro model known as Discrete Particle Model (DPM) and it was developed by Prof. J. A. M. Kuipers group, University of Twente, The Netherlands (29). The present Discrete Particle Model (DPM) involves both particle and gas phases. The particle phase is described by using Newton's equation of motion for each particle as a single entity. The continuous gas phase is described using volume averaged Navier-Stokes equations under isothermal conditions. The interaction between particles and gas phase is coupled through two terms, porosity and momentum exchange source term. The porosity in each cell is calculated by direct calculation of the volume of the particles present in a cell where as the momentum exchange source term is derived from lattice Boltzmann simulations. For solving the Newton's equations we used a first order integration scheme. The gas phase equations are solved using SIMPLE (Semi Implicit Method for Pressure Linked Equations) scheme. The particle interactions are resolved through binary hard sphere collision model. We used a smaller time step for the calculation of the particle interactions compared to the gas phase equations.

A novel technique for calculating the particle collisions from the dynamic discrete particle simulations of non-homogeneous granular flows of the particles was presented in Chapter 4. It was observed that the self collisions among the particles of the same size class were neglected in the

Smoluchowski equation. The effect of this term was analyzed for discrete particle model simulations, we found that the effect of this term may be neglected for a large number of particles. We calculated the particle Reynolds number and it was observed that the shear forces are more dominant in the present fluidized bed simulations. Therefore a shear kernel is expected.

To calculate the collisions among the particles, we introduced new subroutines in the existing Discrete Particle Model code. We introduced a new parameter known as the bed parameter in order to understand macroscopic characters on the particle collisions. We considered different initial particle size distributions satisfying equal number of particles (zeroth moment), equal length, equal surface area, equal volume (first moment) criteria for each size class and a discrete log-normal particle size distribution. The effect of various initial particle size distributions on the bed parameter were analyzed for pseudo three dimensional and three dimensional simulated fluidized beds.

The evolution of the particle size distribution that results from the aggregation are presented in the Chapter 6. We evaluated the particle aggregation efficiency for different initial particle size distributions. We incorporated a random aggregation mechanism for the aggregation of two particles. As a result of this aggregation a new particle of larger size is formed and the other particle disappeared, we call this particle a ghost particle. This ghost particle has no physical significance in the simulation and proper modifications were made in order to avoid its presence for the rest of the simulation time. The number of ghost particles formed is equal to the number of successful aggregations. We evaluated the aggregation efficiency rate for each simulation by collecting the number of successful aggregations and the resulting new particle size distribution. Therefore, we are able to model aggregation kernels from these micro simulations. We calculated the particle size distribution from the macro model known as aggregation equation with these new kernels. The aggregation equation with these newly simulated kernels was solved by using the cell average technique.

It was demonstrated in the thesis that the Discrete Particle Model (micro models) is an excellent tool to provide detailed information about the basic particle flow characteristics, which are (extremely) difficult if not impossible to obtain from experiments. The present modelling approach can be used to various types of fluidized beds like spouted fluidized beds, circulating fluidized beds, risers, etc. In the future, we intend to incorporate the physically relevant aggregation mechanism for the aggregation process by spraying the liquid binder on to particles. To model such applications one needs to extend the present model with the inclusion of a liquid droplet phase and nozzle. A multi particle aggregation can be simulated by considering the particle interactions with a soft sphere collision model, but the computational time will be expensive.

Comparing the present aggregation kernels with the experiments would be valuable for designing industrial level fluidized beds.

Appendix A

A.1 Analytical derivation of shear kernel for fluidized bed

Particles collisions in a uniform, laminar shear flow due to the relative motion of the particles. This relative motion is due to the differences in size and velocity of the particles. Particle collisions due to shear field in an ideal case can be seen in Figure A.1.

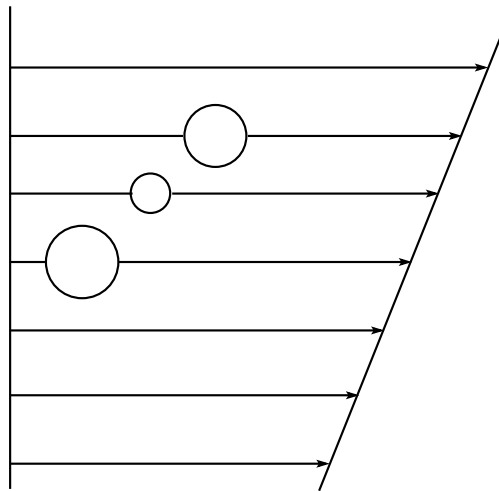


Figure A.1: Ideal collisions of particles in a uniform, laminar shear flow. The lower particles, are moving at a higher velocity, overtakes and collides with slower moving particle

In the ideal case, streamlines are assumed to be straight and the particle motion is rectilinear. This is an oversimplification for the motion of the particles in the fluidized bed. Since the shear flow is affected by the nonideal collisions of the particles, walls of the fluidized bed, properties of the gas and particles, etc. So we can not expect an ideal, uniform, laminar flow field inside the fluidized bed. Therefore, we try to introduce a parameter to account these effects. We call this parameter as bed parameter and it is denoted by η .

To derive an expression for the collision frequency, we refer to Figure A.1, which shows the

particle interactions due to shear flow. As shown in figure 1 the particle of radius a_i collides with the particle of radius a_j due to their relative difference in the velocity, as shown in Figure A.2.

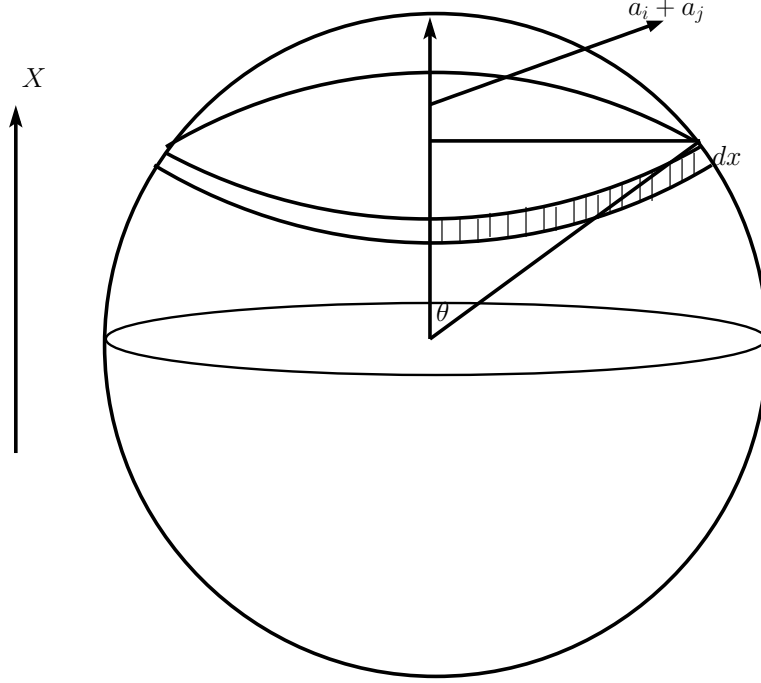


Figure A.2: Geometry for coagulation in a laminar shear field

The velocity of the particle normal to the surface of the page, relative to the particle shown is $x \frac{du}{dx}$. Hence flow of the particles into the shaded portion of the strip dx is given by

$$F = \eta n_j x \frac{du}{dx} (a_i + a_j) \sin \theta dx.$$

Here we introduced the parameter η to account for the distorted shear flow due to non-ideal particle collisions, effects of the boundary of the bed,...etc. Since $x = (a_i + a_j) \cos \theta$, the total number of particles entering into the central sphere is given by

$$F = 2(2)\eta n_j \int_0^{\frac{\pi}{2}} (a_i + a_j)^3 \frac{du}{dx} \sin^2 \theta \cos \theta d\theta$$

where the first factor 2 takes into the account of particles entering from the upper hemisphere from this side plus the particles entering from the bottom hemisphere from back side. The second factor 2 is necessary because the integration from 0 to $\frac{\pi}{2}$ must be done twice. Carrying out the

A.2. ANALYTICAL SOLUTION FOR SHEAR KERNEL FOR MONODISPERSE INITIAL CONDITIONS

integration the result is

$$\begin{aligned} F &= \frac{4}{3}\eta(a_i + a_j)^3 \frac{du}{dx} n_j \\ \Rightarrow N_{ij} &= \frac{4}{3}\eta(a_i + a_j)^3 \frac{du}{dx} n_i n_j \\ \Rightarrow N_{ij} &= \eta\beta(a_i, a_j) n_i n_j \end{aligned}$$

where $\beta(a_i, a_j) = \frac{4}{3}(a_i + a_j)^3 \frac{du}{dx}$ is the collision frequency function for the coagulation of the particles by laminar shear flow. When we consider the volume of the particles, the collision frequency function for the laminar shear flow is given by

$$\beta(v_i, v_j) = \frac{4}{3}(v_i^{\frac{1}{3}} + v_j^{\frac{1}{3}})^3 \frac{du}{dx}.$$

A.2 Analytical solution for shear kernel for monodisperse initial conditions

The discrete coagulation equation for the laminar shear kernel is:

$$\frac{dn_k}{dt} = \frac{1}{2} \sum_{i+j=k} \left[\frac{4}{3}(a_i + a_j)^3 \frac{du}{dx} n_i n_j \right] - \sum_{i=1}^{\infty} \frac{4}{3}(a_i + a_j)^3 \frac{du}{dx} n_i n_k$$

If the system is composed of particles that are all of nearly the same size, $a_i \approx a$, then the above equation becomes

$$\frac{dn_k}{dt} = \frac{1}{2} \sum_{i+j=k} \left[\frac{32}{3} a^3 \frac{du}{dx} n_i n_j \right] - \sum_{i=1}^{\infty} \frac{32}{3} a^3 \frac{du}{dx} n_i n_k.$$

Summing over all k , the result is

$$\frac{dN_{\infty}}{dt} = -\frac{16}{3} \frac{du}{dx} a^3 N_{\infty}^2.$$

But $\frac{4}{3}\pi a^3 N_{\infty} = V = \text{constant}$

$$\frac{dN_{\infty}}{dt} = -\frac{4V}{\pi} \frac{du}{dx} N_{\infty}.$$

Here the decay is proportional to N_{∞} , where as for the Brownian kernel it is proportional to N_{∞}^2 in the continuum range. Let $N = N_{\infty}(0)$ be the initial number of particles at $t = 0$. Then solving the above equation subject to this initial condition gives:

$$\begin{aligned} \frac{dN_{\infty}}{dt} &= -\frac{4V}{\pi} \frac{du}{dx} N_{\infty} \\ N &= N_{\infty}(0) \end{aligned}$$

$$\begin{aligned} N_{\infty}(t) &= C_1 e^{-\frac{4V}{\pi} \frac{du}{dx} t} \\ \because N_{\infty}(0) &= C_1 e^0 \\ &\Rightarrow C_1 = N_{\infty}(0) \\ \therefore \ln \frac{N_{\infty}(t)}{N_{\infty}(0)} &= \frac{4V}{\pi} \frac{du}{dx} t \end{aligned}$$

Appendix B

B.1 Physical and Numerical parameters of the simulations

Table B.1: The Parameters for the simulation

| <i>Parameter</i> | <i>Value</i> |
|---------------------------------------|---|
| Time step of calculation Δt | 1.00e-4 sec |
| Simulation time | 15 sec |
| <i>Bed properties</i> | |
| Height | 0.30 m |
| Width | 0.10 m |
| Depth | 0.01 m (pseudo 3D bed), 0.10 m 3D bed |
| <i>Particle properties</i> | |
| Material | glass particles |
| Number of primary particles | 5000, 10000, 15000 |
| Diameter d_α | 1.0e-3 m pseudo 3D bed 1.8e-3 m 3D bed |
| Density ρ | 2500 kg/m ³ |
| <i>Gas properties</i> | |
| Fluidisation velocity u | 2.4 m/sec |
| Viscosity μ | 1.82e-5 kg/ms |
| Density ρ_g | 1.21 kg/m ³ |
| Temperature T | 298 K |
| Gas constant R | 8.314 J/(mol K) |
| Average molecular weight of air M_g | 28.8e-3 kg/mol |
| <i>Particle contact constants</i> | |
| Spring coefficient k | 5.0e+5 |
| Restitution coefficient e | 0.98 |
| Friction coefficient | 0.09 |

B.2 Initial particle size distributions

B.2.1 Particle size distribution for 5000 particles

| Simulation | Criteria | Number of particles |
|------------|----------|------------------------------|
| 1 | 1 | 1000, 1000, 1000, 1000, 1000 |
| 2 | 2 | 1350, 1072, 937, 851, 790 |
| 3 | 3 | 1755, 1105, 843, 697, 600 |
| 4 | 4 | 2190, 1095, 730, 547, 438 |

Table B.2: Five classes

Table B.2 gives the number of particles in each class, having $I = 5$ classes, satisfying the criterias 1, 2, 3 and 4 with $N_0 = 5000$.

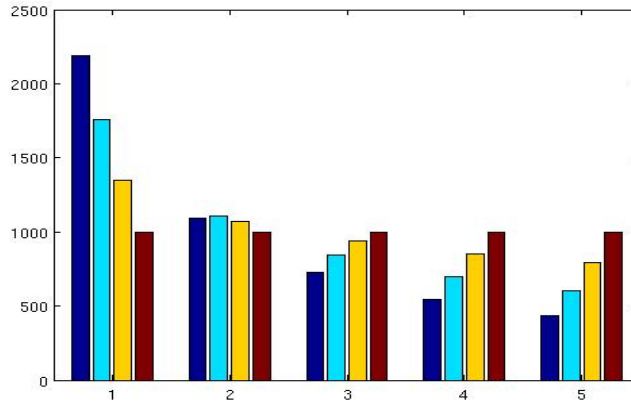


Figure B.1: Initial condition for the simulations: Particle class vs Number of particles

The bar diagram Figure B.1 represents the number of particles in each of the five classes satisfying the criteria 1-4 corresponding to the Table B.2.

| Simulation | Criteria | Number of particles |
|------------|----------|---|
| 5 | 1 | 500, 500, 500, 500, 500, 500, 500, 500, 500, 500 |
| 6 | 2 | 804, 638, 557, 506, 470, 442, 421, 402, 387, 373 |
| 7 | 3 | 1213, 764, 583, 481, 415, 368, 332, 303, 280, 261 |
| 8 | 4 | 1707, 853, 569, 426, 341, 285, 244, 214, 190, 171 |

Table B.3: Ten classes

Table B.3 gives the number of particles in each class, having $I = 10$ classes, satisfying the criterias 1, 2, 3 and 4 with $N_0 = 5000$.

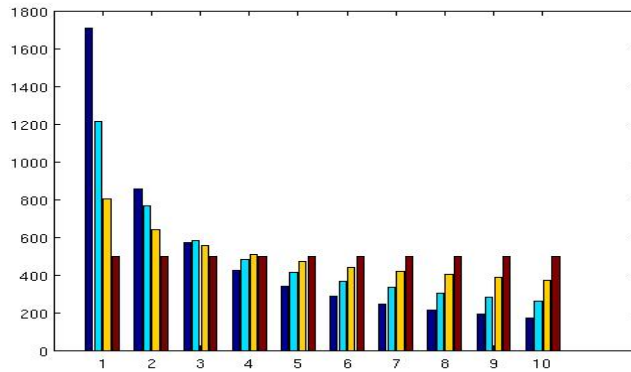


Figure B.2: Initial condition for the simulations: Particle class vs Number of particles

| Sim | Criteria | Number of particles |
|-----|----------|--|
| 9 | 1 | 333, 333, 333, 333, 333, 333, 333, 333, 333, 333, 333, 334, 334, 334, 334, 334 |
| 10 | 2 | 599, 475, 415, 377, 350, 329, 313, 299, 288, 278, 269, 262, 255, 248, 243 |
| 11 | 3 | 994, 626, 478, 395, 340, 301, 271, 248, 229, 214, 201, 189, 180, 171, 163 |
| 12 | 4 | 1507, 753, 502, 377, 301, 251, 215, 189, 168, 151, 137, 125, 116, 108, 100 |

Table B.4: Fifteen classes

The bar diagram Figure B.2 represents the number of particles in each of the five classes satisfying the criteria 1-4 corresponding to the Table B.3.

Table B.4 gives the number of particles in each class, having $I = 15$ classes, satisfying the criterias 1, 2, 3 and 4 with $N_0 = 5000$.

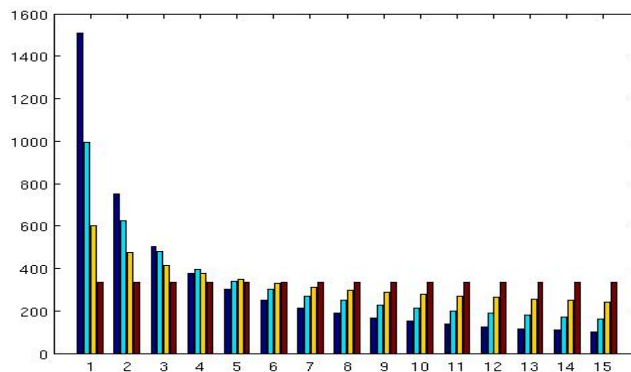


Figure B.3: Initial condition for the simulations: Particle class vs Number of particles

The bar diagram Figure B.3 represents the number of particles in each of the five classes satisfying the criteria 1-4 corresponding to the Table B.4.

B.2.2 Particle size distribution corresponding to 15000 particles

| Simulation | Criteria | Number of particles |
|------------|----------|------------------------------|
| 1 | 1 | 3000, 3000, 3000, 3000, 3000 |
| 2 | 2 | 4052, 3216, 2809, 2553, 2370 |
| 3 | 3 | 5264, 3316, 2531, 2089, 1800 |
| 4 | 4 | 6569, 3285, 2190, 1642, 1314 |

Table B.5: Five classes

Table B.5 gives the number of particles in each class, having $I = 5$ classes, satisfying the criterias 1, 2, 3 and 4 with $N_0 = 15000$.

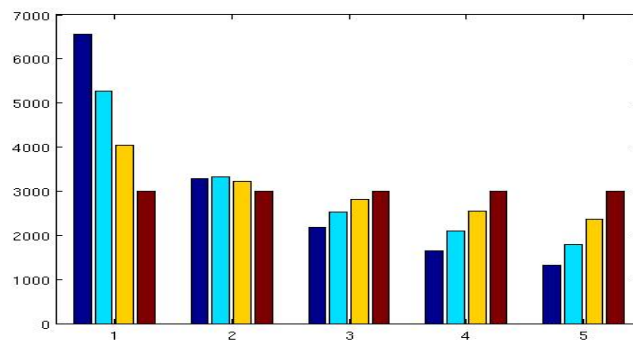


Figure B.4: Initial condition for the simulations: Particle class vs Number of particles

The bar diagram Figure B.4 represents the number of particles in each of the five classes satisfying the criteria 1-4 corresponding to the Table B.5. Table B.6 gives the number of particles in

| Simulation | Criteria | Number of particles |
|------------|----------|--|
| 5 | 1 | 1500, 1500, 1500, 1500, 1500, 1500, 1500, 1500, 1500, 1500 |
| 6 | 2 | 2412, 1914, 1672, 1519, 1410, 1327, 1261, 1206, 1160, 1119 |
| 7 | 3 | 3639, 2292, 1749, 1444, 1245, 1102, 994, 910, 841, 784 |
| 8 | 4 | 5121, 2561, 1707, 1280, 1024, 854, 732, 640, 569, 512 |

Table B.6: Ten classes

each class, having $I = 10$ classes, satisfying the criterias 1, 2, 3 and 4 with $N_0 = 15000$.

The bar diagram Figure B.5 represents the number of particles in each of the five classes satisfying the criteria 1-4 corresponding to the Table B.6.

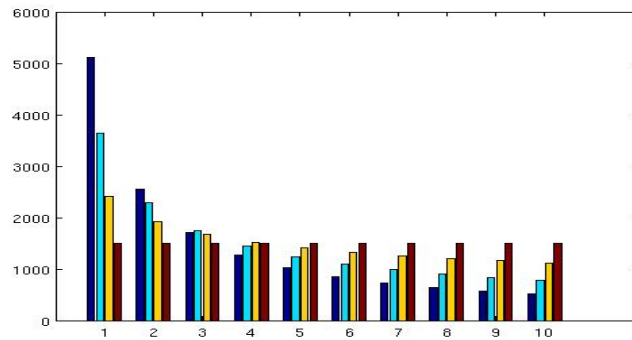


Figure B.5: Initial condition for the simulations: Particle class vs Number of particles

| Sim | Crit | Number of particles |
|-----|------|--|
| 9 | 1 | 1000, 1000, 1000, 1000, 1000, 1000, 1000, 1000, 1000, 1000, 1000, 1000, 1000, 1000 |
| 10 | 2 | 1796, 1426, 1245, 1131, 1050, 988, 939, 898, 863, 834, 808, 785, 764, 745, 728 |
| 11 | 3 | 2981, 1878, 1433, 1183, 1019, 903, 814, 745, 689, 642, 602, 569, 539, 513, 490 |
| 12 | 4 | 4520, 2260, 1507, 1130, 904, 754, 646, 565, 502, 452, 411, 377, 348, 323, 301 |

Table B.7: Fifteen classes

Table B.7 gives the number of particles in each class, having $I = 15$ classes, satisfying the criterias 1, 2, 3 and 4 with $N_0 = 15000$.

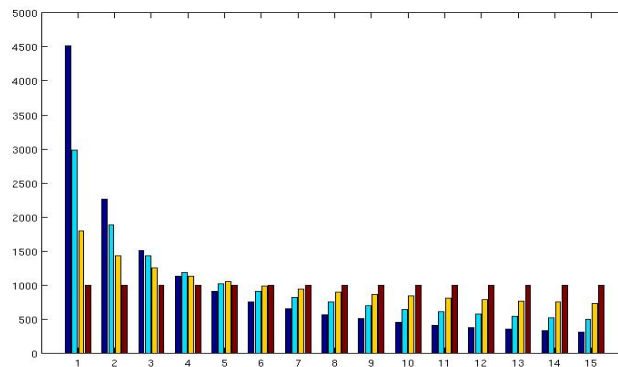


Figure B.6: Initial condition for the simulations: Particle class vs Number of particles

The bar diagram Figure B.6 represents the number of particles in each of the five classes satisfying the criteria 1-4 corresponding to the Table B.7.

Bibliography

- [1] Adetayo, A. A., B. J. Ennis., 1997, "Unifying approach to modelling granule coalescence mechanisms", *AIChE Journal*, 43(4), 927-934.
- [2] Anderson, T. B., R. Jackson., 1967, "A fluid mechanical description of fluidized beds", *I & EC Fundamentals*, 6(4), 527-539.
- [3] Beetstra, R., M. A. van der Hoef., J. A. M. Kuipers., 2007, "Numerical study of segregation using a new drag force correlation for polydisperse systems derived from lattice-Boltzmann simulations", *Chemical Engineering Science*, 62, 246-255.
- [4] Berry, E. X., 1967, "Cloud droplet growth by collection", *Journal of Atmospheric Science*, 24, 688-701.
- [5] Bertram. A., Jürgen Tomas, (Editors)., 2008, "Micro-Macro-Interactions,"in *Structured Media and Particle Systems*, Springer-Verlag, Heidelberg.
- [6] Bramley, A. S., M. J. Hounslow., R. L. Ryall., 1996, "Aggregation during precipitation from solution: A method for extracting rates from experimental data", *Journal of Colloid and Interface Science*, 183, 155-165.
- [7] Cameron, I. T., F. W. Wang., C. D. Immanuel., F. Stepanek., 2005, "Process systems modelling and applications in granulation: A review", *Chemical Engineering Science*, 60, 3723-3750.
- [8] Chamakuri, N., 2007, "Adaptive numerical simulation of reaction-diffusion systems", *PhD thesis*, Otto-von-Guericke University, Magdeburg.
- [9] Costa, C. B.B., M. R. W. Maciel., R. Maciel Filho., 2006, "Considerations on the crystallizing modelling: Populating balance solution", *Computers & Chemical Engineering*, doi:10.1016/j.compchemeng.2006.06.005.
- [10] Cryer, S. A., 1999, "Modeling agglomeration processes in fluid-bed granulation", *AIChE Journal*, 45(10), 2069-2078.
- [11] Deen, N. G., M. Van Sint Annaland., M. A. Van der Hoef., J. A. M. Kuipers., 2006, "Review of discrete particle modeling of fluidized beds", *Chemical Engineering Science*, doi:10.1016/j.ces.2006.08.014.

- [12] Drake, R. L., 1970, "A General Mathematical Survey of the Coagulation Equation," in *Topics in Current Aerosol Research*, (part 2), (G. M. Hidy and J. R. Brock, Eds.), p. 315, Pergamon Press, Newyork.
- [13] Ergun, S., 1952, "Fluid flow through packed columns", *Chemical Engineering Progress*, 48, 89-94.
- [14] Friedlander, S. K., 1977, "*Smoke, Dust, and Haze: Fundamentals of Aerosol Dynamics*", Oxford University Press, NewYork.
- [15] Gantt, J. A., I. T. Cameron., J. D. Litster., E. P. Gatzke., 2006, "Determination of coalescence kernels for high-shear granulation using DEM simulations", *Powder Technology*, 170, 53-63.
- [16] Godlieb, W., 2005, "Simulating a granulator using the discrete particle model" Masters thesis, University of Twente, The Netherlands.
- [17] Goldsmith, M. J. V., 2001, "Hydrodynamics modelling of fluidized bed spray granulation." PhD thesis, University of Twente, The Netherlands.
- [18] Handwerker, J., 2007, "Vorlesung radarmeteorologie 2006/2007", *Institut für meteorologie und klimaforschung.*, Karlsruhe, 1-72.
- [19] Hintz, W., Tzv. Nikolov., V. Jaordanova., J. Tomas., 2003, "Preparation of titanium dioxide nanoparticles and their characterisation", *Nanoscience & Nanotechnology*, 3, 73-76.
- [20] Hoomans, B. P. B., 2000, "Granular dynamics of Gas-Solid two-phase flow." PhD thesis, University of Twente, The Netherlands.
- [21] Hoomans, B. P. B., J. A. M. Kuipers., W. J. Briels., and W. P. M. van Swaij., 1996, "Discrete particle simulation of the bubble and slug formation in a two-dimensional gas-fluidised bed, A hard sphere approach" *Chemical Engineering Science*, 51(1), 99-108.
- [22] Hounslow, M. J., 1998, "Some problems in particle technology: A statistical mechanical formulation", *KONA.*, 19, 555.
- [23] Hounslow, M. J., 1990, "Nucleation, growth, and aggregation rates from steady-state experimental data", *AIChE Journal.*, 36(11), 1748-1752.
- [24] Hu, K. C., R. Mei., 1998, "A note on particle collision rate in fluid flows", *Phys. Fluids*, 10, 1028-1030.
- [25] Hulburt, H. M., S. Katz., 1964, "Some problems in particle technology: A statistical mechanical formulation", *Chem. Eng. Sci.*, 19, 555.
- [26] Kapur, P. C., D. W. Fuerstenau., 1966, " Size distributions and kinetic relationships in the nuclei region of wet pelletization", *I & EC Process design and development*, 5(1), 5-10.

- [27] Kapur, P. C., 1972, "Kinetics of granulation by non-random coalescence mechanism", *Chemical Engineering Science*, 27, 1863-1869.
- [28] Kapur, P. C., D. W. Fuerstenau., 1969, "A coalescence model for granulation", *I & EC Process Design and Development*, 8(1), 56-62.
- [29] Kuipers, J. A. M., Van Duin, K. J., Van Beckum, F. P. H., Van Swaaij, W. P. M., 1992, "A numerical model of gas-fluidized beds", *Chemical Engineering Science*, 47(8), 1913-1924.
- [30] Kumar, J., 2006, "Numerical approximations of population balance equations in particulate systems", *PhD thesis*, Otto-von-Guericke University, Magdeburg. ISBN 3-93939665-13-4.
- [31] Kumar, J., Peglow, M., Warnecke, G., Heinrich, S., Mörl, L., 2006, "Improved accuracy and convergence of discretized population balance for aggregation: The cell average technique", *Chemical Engineering Science*, 61, 3327-3342.
- [32] Kumar, S., Ramakrishna, D., 1996, "On the solution of population balance equations by discretization -I. A fixed pivot technique.", *Chemical Engineering Science*, 51, 1311-1332.
- [33] Link, J. M., L.A., Cuypers, N. G. Deen and J. A. M. Kuipers. 2005, "Flow regimes in a spout fluid bed: a combined experimental and simulation study." *Chemical Engineering Science*, 60, (13): 3425-3442.
- [34] Litster, J., B. Ennis., L. Liu., 2004, "The science and engineering of granulation process", *Kluwer Academic Publishers*, The Netherlands.
- [35] Liu, L. X., Litster, J. D., Iveson, S. M., Ennis, B. J., 2000, "Coalescence of deformable granules in wet granulation processes", *AIChE Journal*, 46(3), 529-539.
- [36] Müller, H., 1922, "A calculation procedure for heat, mass and momentum transfer in three-dimensional parabolic flow." *Int. J. Heat and Mass Transfer*, vol 15: 1787.
- [37] Norio, O., Tatsuo, T., 1975, "The probability of coalescence in granulation kinetics", *I & EC Process Design and Development*, 14(3), 286-289.
- [38] Patankar, S. V. and Spalding, D. B. 1972, "A calculation procedure for heat, mass and momentum transfer in three-dimensional parabolic flow." *Int. J. Heat and Mass Transfer*, vol 15: 1787.
- [39] Peglow, M., 2003, "Population Balance Modelling", *PhD thesis*, Otto-von-Guericke University, Magdeburg.
- [40] Pouw, A. G., Daan Verkoeijn., G. M. H. Meesters., B. Scarlett., 2002, "Population balances for particulate processes-a volume approach", *Chemical Engineering Science*, 57 , 2287-2303.
- [41] Pruppacher, H. R. and J. D. Klett., 1996, "Microphysics of clouds and precipitation", *Kluwer Academic Publishers*, Dordrecht, The Netherlands.

- [42] Quarteroni, A., 2009, "Mathematical models in science and engineering", *Notices of AMS*, 56(1), 10-19.
- [43] Ramakrishna, D., 2000, "Population balances: Theory and Applications to Particulate Systems in Engineering", *Academic Press*, San Diego, CA.
- [44] Rynhart, P. R., 2004, "Mathematical modelling of granulation process", *PhD thesis*, Massey University, New Zealand.
- [45] Sandu, A., 2002, "A Newton-Cotes quadrature approach for solving the aerosol coagulation equation", *Atmospheric Environment*, 36, 583-589.
- [46] Sastry, K. V. S., 1975, "Similarity size distribution of agglomerates during their growth by coalescence in granulation or green pelletization." *International Journal of Mineral Processing*, 2, 187-203.
- [47] Sastry, K. V. S., D. W. Fuerstenau., 1970, "Size distribution of agglomerates in coalescing dispersed phase systems." *I & EC Fundamentals*, 9(1), 145-149.
- [48] Smoluchowski, M. V., 1916, "Drei Vorträge über Diffusion, Brownische Molekularbewegung und Koagulation von Kolloidteilchen", *Phys. Z.*, 17, 557.
- [49] Smoluchowski, M. V., 1917, "Mathematical theory of the kinetics of the coagulation of colloidal solutions", *Z. Phys. Chem.*, 92, 129-168.
- [50] Stefan Heinrich., 2001, "Modellierung des wärmeund stoffübergangs sowie der partikelpopulationen bei der wirbelschicht-sprühgranulation", *PhD thesis*, Otto-von-Guericke University, Magdeburg. ISBN 3-18-367503-X.
- [51] Tan, H. S., M. J. V. Goldschmidt., R. Boerefijn., M. J. Hounslow., A. D. Salman., J. A. M. Kuipers., 2004, "Building population balance model for fluidized bed melt granulation: lessons from kinetic theory of granular flow", *Powder Technology*, 142, 103-109.
- [52] Tatang M. A., 1995, "Direct incorporation of uncertainty in chemical and environmental engineering systems", *PhD Thesis*, MIT, Cambridge, MA.
- [53] Wen, Y. C., Yu, Y. H., 1966, "Mechanics of Fluidization. Chemical engineering progress symposium series", 62, 100-111.
- [54] Yang, W. C., 2003, "Handbook of fluidization and fluid-particle systems", Dekker, New York.
- [55] Zeilstra, C., A. Bokkers., 2005, "3D-DPM manual", *Fundamental of Chemical and Reaction Group*, University of Twente, The Netherlands.

Curriculum Vitae

Personal Details

Name : **Narni Nageswara Rao**
Sex : Male
Marital status : Single
Date of birth : 01.07.1979
Place of birth : Kappaladoddi, Krishna, A. P.
Nationality : Indian

Education and Employment

1991-1994 High Schoolings, A. P. Residential School, Nimmakuru, India
1994-1996 Intermediate in Mathematics, Physics, Chemistry
The Hindu College, Machilipatnam, India
1996 - 1999 Bachelor of Science (B.Sc.) in Mathematics, Physics, Chemistry
A. P. Residential Degree Collge, Nagarjuna Sagar, India
1999 - 2001 Master of Science (M.Sc.) in Applied Mathematics
Regional Engineering College (REC) Warangal, India
2001 - 2002 Master of Philosophy (M.Phil.) in Applied Mathematics
University of Hyderabad, India
2002 - 2003 Temporary Assistant Lecturer in Mathamtics
National Institute of Technology Karnataka (NITK), India
2003 - 2005 Master of Technology (M.Tech.) in Industrial Mathematics and
Scientific Computing,
Indian Institute of Technology Madras, India
2005 - 2008 PhD graduation (DFG scholarship) within the
Graduiertenkolleg, "GK 828", Faculty of Mathematics,
Otto-von-Guericke-University, Magdeburg, Germany.

Academic Honors

- Qualified National Eligibility Test (NET)-2002.
- DAAD-IIT Academic Exchange Fellowship, Germany (2004-2005).
- German Research Foundation (DFG) Graduiertenkolleg Scholarship (2005-2008).